



Ship emission influence on clouds in satellite and model data

Karsten Peters



Hinweis

Die Berichte zur Erdsystemforschung werden vom Max-Planck-Institut für Meteorologie in Hamburg in unregelmäßiger Abfolge herausgegeben.

Sie enthalten wissenschaftliche und technische Beiträge, inklusive Dissertationen.

Die Beiträge geben nicht notwendigerweise die Auffassung des Instituts wieder.

Die "Berichte zur Erdsystemforschung" führen die vorherigen Reihen "Reports" und "Examensarbeiten" weiter.



Notice

The Reports on Earth System Science are published by the Max Planck Institute for Meteorology in Hamburg. They appear in irregular intervals.

They contain scientific and technical contributions, including Ph. D. theses.

The Reports do not necessarily reflect the opinion of the Institute.

The "Reports on Earth System Science" continue the former "Reports" and "Examensarbeiten" of the Max Planck Institute.

Anschrift / Address

Max-Planck-Institut für Meteorologie
Bundesstrasse 53
20146 Hamburg
Deutschland

Tel.: +49-(0)40-4 11 73-0
Fax: +49-(0)40-4 11 73-298
Web: www.mpimet.mpg.de

Layout:

Bettina Diallo, PR & Grafik

Titelfotos:

vorne:

Christian Klepp - Jochem Marotzke - Christian Klepp

hinten:

Clotilde Dubois - Christian Klepp - Katsumasa Tanaka

Ship emission influence on clouds in
satellite and model data

Karsten Peters

aus Braunschweig

Hamburg 2011

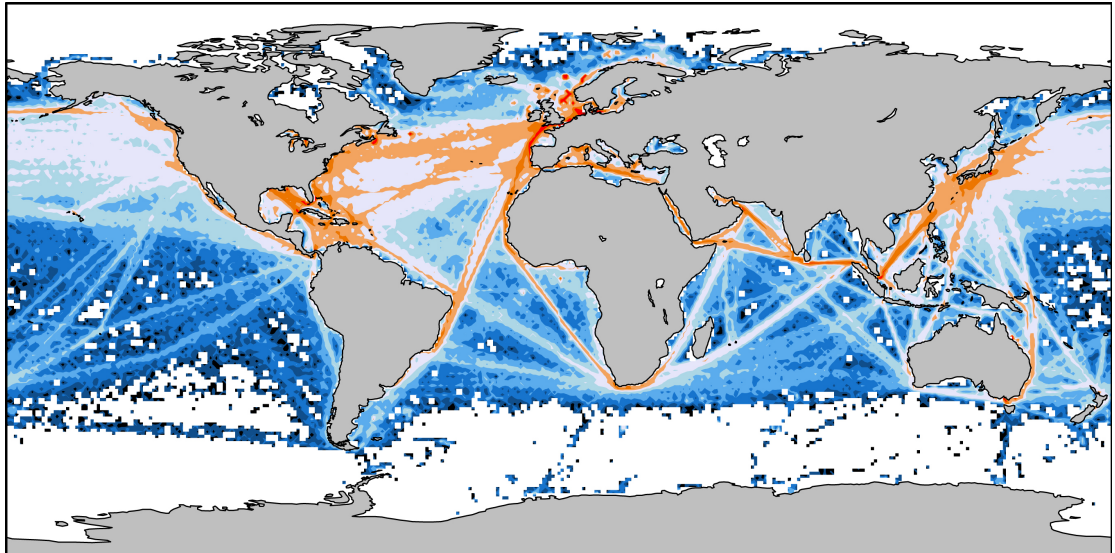
Karsten Peters
Max-Planck-Institut für Meteorologie
Bundesstrasse 53
20146 Hamburg
Germany

Als Dissertation angenommen
vom Department Geowissenschaften der Universität Hamburg

auf Grund der Gutachten von
Prof. Dr. Hartmut Grassl
und
Prof. Dr. Johannes Quaas

Hamburg, den 8. Dezember 2011
Prof. Dr. Jürgen Oßenbrügge
Leiter des Departments für Geowissenschaften

Ship emission influence on clouds in satellite and model data



Karsten Peters

Hamburg 2011

Title page:

Global distribution of SO₂-emissions from ships for the year 2000 as provided in the shipping emissions inventory presented in Behrens (2006). The colour scale denotes the annual emissions in metric tons per 1°×1° grid box:



CONTENTS

Abstract	iii
Zusammenfassung	v
1 Introduction	1
1.1 Motivation	1
1.2 Physical basis and investigative methods	2
1.2.1 Clouds and aerosols in the climate system	2
1.2.2 Tools for investigating aerosol effects	5
1.3 Key objectives and outline of this thesis	7
2 Analysis with satellite data	9
2.1 Data	10
2.1.1 Clouds, aerosols and radiation	10
2.1.2 Meteorological environment	11
2.1.3 Ship emission inventory	11
2.2 General methodology	12
2.3 Lagrangian approach	15
2.3.1 Method	15
2.3.2 Results	18
2.4 Eulerian approach	21
2.4.1 Method	21
2.4.2 Results	23
2.5 Summary and Conclusions	33
3 Global modelling of ship-induced AIEs	37
3.1 The ECHAM5-HAM aerosol climate model	37
3.1.1 Dynamics	37
3.1.2 Aerosols	39
3.1.3 Clouds	40
3.1.4 Aerosol emissions	42

3.1.5	Experiments	44
3.2	Ship-emission induced processes in ECHAM5-HAM	48
3.2.1	Changes in emissions and mass burdens	49
3.2.2	Changes in aerosol number burdens	51
3.2.3	Changes in predicted CCN concentrations	56
3.2.4	Changes in cloud micro- and macrophysical properties	57
3.2.5	Impact on atmospheric radiation	58
3.3	Sensitivity to emission parameters	60
3.3.1	Changes in the emission parametrisation	61
3.3.2	Changes in the amount of emissions	67
3.3.3	Reduction of carbonaceous emissions	69
3.4	Summary	70
4	Combining modelling and satellite approaches	73
4.1	On the benefits and issues of comparing satellite- to model data	73
4.2	Sampling approach	75
4.3	Results	77
4.4	Summary and Conclusions	89
5	Summary, Implications and Outlook	91
5.1	Summary	91
5.2	Implications	94
5.3	Outlook	94
A	Implementing the nudging	97
B	Conditional vs. unconditional sampling of the AIE	101
	Bibliography	105
	Acknowledgements	117

ABSTRACT

The impact of large-scale cloud modification through anthropogenic emissions of aerosols and aerosol precursor gases (“aerosol indirect effects”, AIEs) on Earth’s climate is weakly constrained when it comes to assessing human-induced climate change. In this thesis, the impact of shipping emissions on cloud fields at large scales is used as a test case to contribute towards the reduction of the uncertainty associated with AIEs. For this, both observational data obtained from space-borne remote sensing and results from global climate modelling are employed.

The observational approach presented here utilises aerosol and liquid-cloud properties as obtained from the two MODIS satellite instruments and combines them with meteorological data from the ERA-Interim project. Three shipping corridors over tropical oceans are investigated by using the information on the large-scale meteorological environment to separate “clean” from “polluted” sectors upwind and downwind of a shipping lane, respectively, of each corridor. Aerosol and cloud properties are then analysed statistically. The analysis reveals no statistically significant impacts of shipping emissions on clouds at a large scale in any of the selected regions. It is concluded that the net AIEs from shipping emissions are not large enough to be distinguishable from the natural dynamics controlling cloud presence and formation in the investigated regions.

A global assessment of AIEs from shipping emissions is performed by employing the aerosol climate model ECHAM5-HAM. An up-to-date shipping emissions inventory is incorporated into the model. The model’s sensitivity towards uncertainties associated with the shipping emissions themselves is investigated. Three sets of sensitivity experiments are performed to assess (1) the uncertainty associated with the size of emitted particles, (2) the uncertainty associated with the total amount of emissions and (3) the impact of reducing carbonaceous emissions from ships. From these experiments, the globally averaged AIEs are found to range from $-0.07 \pm 0.01 \text{ Wm}^{-2}$ to $-0.32 \pm 0.01 \text{ Wm}^{-2}$, the magnitude of which depends much more on the assumed emission size distribution than on the magnitude of the emissions themselves. Although the upper estimate from this thesis is relatively large, with the current best estimate of the first AIE, or “Twomey-effect”,

being -0.7 Wm^{-2} , it is about half of the previous upper estimate of AIEs from shipping emissions. The reduction of carbonaceous emissions from ships is not found to have important implications for the simulated AIEs in ECHAM5-HAM.

The gap between satellite observations and model simulations is bridged by sampling the model output in a similar way as the satellite data. The results confirm those obtained from the satellite data analysis, *i.e.* clouds are not subject to substantial changes at the location of the shipping lane in the three tropical regions considered. However, this analysis reveals marked changes in atmospheric composition at the exact position of the shipping lane.

In conclusion, the results presented in this thesis show a smaller effect of shipping emissions on large-scale clouds fields than previously estimated. Thus shipping emissions have important implications for determining the sensitivity of Earth's climate system to external forcings.

ZUSAMMENFASSUNG

Die Quantifizierung der Auswirkung großskaliger Wolkenmodifikation durch anthropogene Emissionen von Aerosolen und Aerosolvorläufergasen (“indirekte Aerosoleffekte”, AIEs) auf den Strahlungshaushalt der Erde ist mit großen Unsicherheiten behaftet. In dieser Dissertation wird der Einfluss von Schiffsemissionen auf Wolken auf großer Skala als Testumgebung genutzt, um zur Reduktion der Unsicherheiten, mit denen AIEs behaftet sind, beizutragen. Dazu werden durch Satellitenfernerkundung erhaltene Messdaten sowie Ergebnisse aus globalen Klimasimulationen verwendet.

Bei der die Messdaten verwendenden Methode werden Aerosol- und Flüssigwasserwolkeigenschaften, abgeleitet aus Messungen der beiden MODIS Instrumente, mit meteorologischen Reanalysedaten des ERA-Interim Projektes kombiniert. Drei Schifffahrtskorridore in tropischen Ozeanen werden im Detail untersucht. Die meteorologischen Daten werden dabei zur Trennung von “sauberen” und “verschmutzten” Gebieten, im Luv bzw. Lee eines jeweiligen Korridors, benutzt. Es folgt die statistische Analyse der Aerosol- und Wolkeneigenschaften. Die Analyse offenbart keinen statistisch signifikanten Einfluss von Schiffsemissionen auf die Wolkenfelder auf großer Skala in den ausgewählten Regionen. Schlussfolgernd sind die AIEs von Schiffsemissionen nicht ausgeprägt genug um von den die Wolkeneigenschaften bestimmenden dynamischen Faktoren genug isoliert zu werden.

Eine globale Abschätzung der von Schiffsemissionen verursachten AIEs erfolgt durch Anwendung des Aerosol-Klimamodells ECHAM5-HAM. Ein aktuelles Schiffsemissionsinventar wird in das Modell implementiert und die Sensitivität des Modells in Bezug auf Unsicherheiten in den Emissionen untersucht. Es werden insgesamt drei Sensitivitätsexperimente zur Quantifizierung (1) der Unsicherheit in Bezug auf die Größe der emittierten Partikel, (2) der Unsicherheit in Bezug auf die Gesamtmenge der Emissionen und (3) der Auswirkung von reduzierter Emission kohlenstoffhaltiger Partikel durchgeführt. Der aus diesen Experimenten erhaltene global gemittelte, durch AIEs verursachte Strahlungsantrieb beträgt $-0.07 \pm 0.01 \text{ Wm}^{-2}$ bis $-0.32 \pm 0.01 \text{ Wm}^{-2}$, wobei dieser Wert viel mehr von

der angenommenen Grössenverteilung der emittierten Partikel als von der Menge der Emissionen selbst abhängt. Obwohl diese obere Abschätzung relativ groß ist (die aktuell beste Abschätzung des global gemittelten sog. ersten AIE, oder “Twomey-Effekt”, beträgt -0.7 Wm^{-2}), ist sie dennoch nur halb so groß wie die vorherige obere Abschätzung von durch Schiffsemissionen verursachten AIEs. Die Reduktion kohlenstoffhaltiger Emissionen hat keinen wesentlichen Einfluss auf die von ECHAM5-HAM simulierten AIEs.

Um eine erhöhte Vergleichbarkeit beider o.g. Ergebnisse zu gewährleisten werden die Modellergebnisse in derselben Weise wie die Satellitendaten untersucht. Die Ergebnisse bestätigen die der Satellitendatenanalyse, d.h. es ist keine wesentliche Modifikation von Wolkeneigenschaften an einer Schifffahrtslinie in den drei untersuchten Regionen erkennbar. Jedoch zeigt diese Analyse deutliche Veränderungen der atmosphärischen Zusammensetzung am Punkt der jeweiligen Schifffahrtslinie auf.

Schlussfolgernd deuten die Ergebnisse dieser Dissertation auf weniger ausgeprägte AIEs von Schiffsemissionen auf Wolken auf großer Skala hin als vorher angenommen. Daher haben Schiffsemissionen wichtige Bedeutung für die Bestimmung der Empfindlichkeit des Klimasystems der Erde in Bezug auf externe Antriebe.

INTRODUCTION

1.1 Motivation

Anthropogenically-induced alteration of the Earth's climatic system is a topic which has gained increasing amounts of attention in recent decades. Although the importance of correctly quantifying this alteration has been known to the scientific community since at least the end of the 1980s, it was the publications of the Intergovernmental Panel on Climate Change (IPCC, 1990, 1995, 2001, 2007) which brought it to the attention of a growing public. A number of policy measures intended to either mitigate or adapt to the consequences of global warming have been introduced globally (UNFCCC (1992); Kyoto Protocol (1997) and the 2° goal of Cancún (2010)).

Human-induced climate change is primarily caused by the emission of long-lived greenhouse gases, not only carbon dioxide (CO_2), but also methane (CH_4), from various activities such as fossil fuel burning or agriculture. This leads to an enhanced trapping of thermal radiation in the Earth System and results in an increase in surface temperature, which has been quantified from measurements of near-surface air temperature (Trenberth et al., 2007). Human activities also lead to the emission of aerosols (*i.e.* small liquid- or solid particles suspended in the air) and their precursor gases. Aerosols influence the Earth's radiation budget by interacting directly with the incident solar radiation, and indirectly through the modification of cloud properties and the associated changes in their reflectivity. Overall, these aerosol effects are believed to exert a net cooling on the Earth System, thereby masking part of the warming induced by changes in greenhouse gas concentrations (*e.g.* Andreae et al., 2005). For this reason, ideas aimed at utilising large amounts of aerosols to increase the reflectivity of the Earth System, so-called “geo-engineering” or “climate-engineering”, have been proposed in the past few years.

Despite growing research activities over the past decades, the level of scientific understanding of the influence of anthropogenic aerosols on clouds (“aerosol indirect effects”, AIEs) remains low. With the implications of these effects continuing to attract the attention of the broader public, it is important to reduce the uncertainties associated with them. This increased understanding could then be utilised to better constrain climate sensitivity, *i.e.* the equilibrium surface-temperature response of the Earth System to a doubling of atmospheric CO₂ as compared to pre-industrial conditions.

Insight into the associated mechanisms and magnitude of AIEs can be derived from numerical modelling (*i.e.* cloud-droplet to global scales) combined with observations (*e.g.* in-situ, ground-based remote sensing, space-borne remote sensing). Recent advances in understanding AIEs have been made by concentrated research efforts on the emissions of sea-going ships, which sometimes leave “ship-tracks” in their wake. Because ships emit aerosols into an often pristine environment, strong cause-and-effect relationships can be established, making areas of intense shipping an ideal focus area for AIE-studies.

1.2 Physical basis and investigative methods

1.2.1 Clouds and aerosols in the climate system

When looking at Earth from space, it is obvious that clouds are an ubiquitous feature of the Earth System. In fact, clouds cover roughly 60% of the Earth’s surface (Rossow and Schiffer, 1999). Clouds are accumulations of tiny water droplets or ice crystals which are present at high concentrations such that their collective interaction with the incoming solar radiation makes them visible to the human eye. Clouds have a number of important radiative effects on the climate system. Probably their most important contribution is that of limiting the amount of energy being absorbed by the Earth System by reflecting a large portion of the incident short-wave (SW) radiation back to space. Clouds also have implications in the long-wave (LW) radiation spectrum. Because cloud tops generally have a colder temperature than the underlying surface, less LW radiation is emitted back to space than if there was no cloud – energy is thereby trapped in the system, leading to a warming. On average, the magnitude of the SW cooling outweighs that of the LW warming. Especially the widespread areas of shallow stratocumulus fields, *e.g.* off the western coasts of Africa and the Americas, contribute to this cooling because they emit LW radiation at about the same temperature as the underlying surface would if there were no cloud present. Last but not least, clouds represent crucial parts of the Earth’s hydrological and energetic cycles by providing for precipitation and the distribution of latent heating, respectively. The remainder of

this thesis focuses on the description of liquid-water clouds, while mixed-phase- and ice clouds are not discussed further.

Liquid cloud droplets form when aerosol particles swell hygroscopically to become cloud condensation nuclei (CCN), a process known as activation. Water vapour condenses on their surface if the ambient water vapour pressure is larger than the saturation water vapour pressure over the CCN. The capability of aerosol particles to act as a CCN depends on their size and chemical composition, although the particle size is believed to be of more relevance (*e.g.* Dusek et al., 2006). The CCN concentration is also highly correlated with the ambient aerosol load (*e.g.* Andreae, 2009). Thus, increases in the ambient aerosol load due to anthropogenic activities almost inevitably lead to increases in the number of CCN. As a result, clouds developing in polluted regions exhibit higher cloud droplet number concentrations (CDNC) for the remainder of this thesis, the focus is put on the description of liquid-water clouds, and it is this increase in CDNC which forms the basis for AIE hypotheses. Concerning the impact on atmospheric radiation, the quantity of interest is the cloud albedo, *i.e.* the fraction of incident solar radiation scattered back to space by the cloud. Following Petty (2006), the albedo α at the top of a plane-parallel homogeneous cloud with vertically constant droplet size distribution is approximately:

$$\alpha = \frac{(1-g)\tau}{1+(1-g)\tau} \quad \text{with} \quad \tau = Q_e \left(\frac{9\pi L^2 H}{16\rho_l^2} N \right)^{\frac{1}{3}} \approx \frac{3L}{2\rho_l r_{\text{eff}}}, \quad (1.1)$$

where g is the asymmetry parameter (typically $g = 0.85$ for stratocumulus clouds), τ is the cloud optical depth, Q_e is the extinction efficiency of a particle (typically $Q_e \approx 2$ for cloud droplets), L is the cloud liquid water path, H is the cloud geometrical thickness, N is the CDNC, r_{eff} is the cloud droplet effective radius and ρ_l is the density of water. Thus, cloud albedo increases with increasing CDNC, increasing liquid water content, and decreasing cloud droplet sizes.

In the past decades, a whole suite of AIE hypotheses has been proposed. Of these, the ‘‘Twomey effect’’, or first AIE, is the most prominent. This assumes that for constant cloud liquid water path (L), the increase in available CCN eventually leads to more and smaller cloud droplets which then enhances cloud albedo. This effect was originally proposed in the 1940s (*e.g.* Hewson, 1943) and was applied to the more general context of anthropogenic pollution by Twomey (1974). The current best estimate of the globally averaged Twomey effect amounts to a radiative forcing (RF) of -0.7 Wm^{-2} but the level of scientific understanding of the processes involved is still considered low. Other AIE hypotheses include effects on cloud lifetime (Albrecht, 1989; Small et al., 2009) and cloud top height (Koren et al., 2005; Devasthale et al., 2005). These are associated with alterations of the hydrological cycle through changes in precipitation and are far from being verified

(*e.g.* Stevens and Feingold, 2009, and references therein). In total, AIEs are subject to the largest uncertainties of all radiative forcing components of the Earth System when it comes to assessing human-induced climate change (Forster et al., 2007).

Apart from having an indirect impact on the Earth’s radiation budget by modifying cloud properties, aerosols and aerosol precursor gases also have aerosol direct radiative effects (DREs), *i.e.* the aerosol particles absorb and scatter the incident solar radiation directly (Ångström, 1962; McCormick and Ludwig, 1967). While at the regional scale, a warming effect by aerosol absorption can be substantial (*e.g.* Peters et al., 2011), at the global scale, aerosol-DREs are believed to exert a net radiative cooling of about -0.5 Wm^{-2} at the top-of-atmosphere (TOA) (Haywood and Boucher, 2000; Forster et al., 2007).

Ship-emission induced aerosol effects

Investigation of AIEs stemming from shipping emissions gives valuable insights into the processes involved and responses of individual cloud systems. Sea-going ships are one of the least regulated sources of anthropogenic emissions, often burning low-quality residual fuels containing high amounts of sulfur and even heavy metals. Besides gaseous compounds such as carbon dioxide (CO_2), carbon monoxide (CO), nitrous oxides (NO_x), methane (CH_4), and non-methane hydrocarbons (NMHCs), the combustion of such fuels produces large amounts of aerosols and aerosol precursors. These come in the form of particulate matter (PM) consisting of elemental (black) and organic carbon, sulfate, ash, and particles forming from sulfuric acid (*e.g.* Eyring et al., 2005b; Petzold et al., 2008). A substantial amount of the emitted particles can serve as CCN, which can result in linear cloud structures referred to as “ship tracks” – a clear manifestation of AIEs from shipping emissions. Ship-tracks were first observed in satellite imagery by Conover (1966). Since then a considerable number of observational studies have contributed to the quantification of the micro- and macrophysical cloud properties of ship-tracks (*e.g.* Coakley et al., 1987; Christensen and Stephens, 2011). Putting ship tracks into the climate context, Schreier et al. (2007) estimated the top-of-atmosphere (TOA) RF of observed ship tracks to be -0.4 to -0.6 mWm^{-2} . More recently, Sayer and Grainger (submitted, 2011) found a value of -8.9 mWm^{-2} . The difference to the results of Schreier et al. (2007) can be explained by different approaches for characterising the atmospheric background.

Ship-tracks have also been evaluated using cloud resolving numerical models. The results indicate that shipping emissions can lead to distinct modifications of the circulation patterns in large-scale cloud fields (*e.g.* Wang and Feingold, 2009). Apart from being manifested in ship-tracks, shipping emissions have the potential to change the micro- and macrophysical properties of cloud fields at large

and climatically relevant scales. The investigation of these large scale effects of shipping emissions needs special attention and should utilise approaches which use data obtained from numerical simulation and/or dedicated observational efforts.

One study to date approaches this issue from the satellite perspective: Devasthale et al. (2006) looked at the statistical properties of low clouds over European coastal waters and found evidence of cloud-property modification through shipping emissions in the heavily frequented area of the English Channel. From the perspective of numerical modelling, a number of studies have utilised general circulation models (GCMs) to quantify the effect of shipping emissions on clouds at a global scale (Capaldo et al., 1999; Lauer et al., 2007, 2009). Some of these studies estimate globally averaged AIEs from shipping emissions to be as much as -0.6 Wm^{-2} at TOA. However, with the International Maritime Organisations' (IMO) regulation on the reduction of the sulfur content of marine bunker fuel coming into force within the next decade (IMO, 1998), the magnitude of the negative TOA RF from ship-induced AIEs may decrease in spite a global increase in ship-traffic (Lauer et al., 2009).

The globally averaged DRE of shipping emissions is small and estimated to range from -47.5 to -9.1 mWm^{-2} (Eyring et al., 2010, and references therein). The emission of trace and long-lived greenhouse gases from ships leads to substantial modifications of atmospheric chemistry (Eyring et al., 2007) and in the long run, the warming effect of the emitted gaseous species will overcompensate for the initial cooling by the emitted aerosols and aerosol precursor gases (Fuglestvedt et al., 2009).

1.2.2 Tools for investigating aerosol effects

In this thesis, the tools of choice for investigating AIEs from shipping emissions are datasets obtained from (1) space-borne passive remote sensing and (2) global climate modelling.

Space-borne remote sensing

Data from space-borne remote sensing are obtained from measurements by instruments which are mounted on satellites orbiting Earth on fixed trajectories in space. Passive sensors measure the upwelling radiation at a number of wavelength intervals. Their wavelength range depends on the sensor and the intended application, *e.g.* UV to VIS for OMI (Ozone Monitoring Instrument), VIS to IR for MODIS (MODerate resolution Imaging Spectroradiometer) or microwave for AMSR-E (Advanced Microwave Scanning Radiometer - EOS). From the measured radiances, properties of the observed scene are obtained by applying inverse modelling approaches. These inverse models rely on a large number of assumptions and

simplifications, thereby making the derivation of geophysical quantities from space-borne remote sensing a challenging task. For the derivation of cloud micro- and macrophysical properties, regions with clouds which are close to “plane-parallel”, *i.e.* spatially homogeneous over large scales like wide-spread stratocumulus fields, generally yield more reliable results than those containing broken cloud fields. In case of multi-level cloud systems, such as fronts or cirrus clouds overlying boundary layer clouds, passive remote sensing only yields reliable information about the top cloud layer. Aerosol properties retrieved from passive remote sensing represent column-integrated values, are normally obtained from cloud-free scenes only, and are more reliable over ocean than over land surfaces. Well-maintained satellite products, such as those distributed by the MODIS science team, also provide uncertainty estimates along with the geophysical data so that the end-user can apply data filtering to suit their research purpose.

Using data from space-borne remote sensing to investigate AIEs has been done in a vast number of studies and most of these rely on regressing aerosol and cloud properties of adjacent scenes to each other. While often yielding exciting results, the scientific community has recently developed scepticism towards these methods because spurious correlations may arise when the limitations of the sensors and the ambient meteorological conditions are not correctly accounted for (Quaas et al., 2010; Grandey and Stier, 2010; McComiskey and Feingold, 2011, and references therein).

Global climate modelling

General circulation models (GCMs) are numerical models that are used to simulate the general characteristics of the atmospheric circulation on long, climatically relevant timescales. GCMs are most often set up to simulate the atmospheric circulation at horizontal resolutions of $\approx 100\text{--}300$ km. For this reason, processes occurring at smaller spatial scales, *i.e.* at “sub-grid” scales, are parametrised in such a way that their effects on large scale resolved variables are correctly reproduced. Cloud processes in particular are therefore heavily parametrised in GCMs. In recent years, a number of modelling groups have implemented sophisticated aerosol-microphysics schemes into their models, that allow for a detailed representation of the global aerosol system. In this way, a more realistic representation of AIEs is also achieved.

The crucial part in obtaining a representative influence of changing aerosol concentrations on cloud properties is the coupling of cloud micro-physics parametrizations to aerosol sub-models. This is most accurately performed by employing so-called double-moment cloud schemes, *i.e.* schemes which calculate cloud water and -ice mixing ratios as well as cloud droplet- and ice crystal concentrations.

Interpreting the results for globally averaged AIEs is often straightforward.

However, it must be stated that the limitation of applying heavily parametrised models to such complicated processes as the ones involving the interaction of aerosols and clouds is that the model's response is more or less given by the way a certain process is incorporated in the parametrisation. A typical example is the way the autoconversion process (*i.e.* the conversion of cloud to precipitable water) is commonly parametrised: an increase in CDNC inevitably decreases the precipitation efficiency and thus increases the cloud liquid water content and no other micro-physical response is allowed.

As detailed above, both the observational and the modelling approaches have their obvious limitations and advantages. Thus, synthesising them promises to yield the most reliable results on AIEs. It is important to note that whatever approach is used, one must clearly be aware of its limitations.

1.3 Key objectives and outline of this thesis

This PhD thesis aims reduce the uncertainty associated with the quantification of AIEs. For this, the effect of emissions from sea-going ships on clouds at climate relevant scales (*i.e.* more than a particular ship-track) is assessed using both space-borne and climate model data. The central starting point of this work is an up-to-date global inventory of shipping emissions (described in Behrens, 2006) that was produced in the framework of the European Integrated Project QUANTIFY, which has provided for the funding of the first year of this PhD project.

The approach using satellite data is presented in Chapter 2. Using the spatial distribution of global shipping emissions provided by the shipping emission inventory, a separation of clean and polluted maritime regions of similar large-scale meteorology is performed for three shipping corridors in tropical regions. To isolate an effect of shipping emissions on cloud properties, a statistical analysis of satellite data with respect to clean and polluted environments is performed. This chapter is accepted for publication in *Journal of Geophysical Research - Atmospheres*¹ and is reproduced with editorial adjustments.

In Chapter 3 the effect of shipping emissions on clouds is investigated on a global scale by employing the ECHAM5-HAM aerosol climate model. This model features a dynamic representation of aerosol processes and the cloud microphysics are parametrised to fully respond to changes in the ambient aerosol population. The simulations performed with ECHAM5-HAM are designed to assess the uncertainties associated with the annual total global fuel consumption and the emission size distribution as well as to investigate the potential implications of mitigating

¹Peters, K., J. Quaas, and H. Graßl (2011), A search for large-scale effects of ship emissions on clouds and radiation in satellite data, *J. Geophys. Res.*, doi:10.1029/2011JD016531, in press.

carbonaceous-particle emissions from ships. The results from one of these simulations are used to illustrate the pathway from the emissions to the resulting influence on cloud properties. For the other experiments, the focus of analysis is instead put towards the resulting impact on atmospheric radiation.

Chapter 4 provides results from applying the sampling method used for the satellite data (Ch. 2) to the model simulation data providing essential insights regarding the results obtained from the satellite data analysis. Both Chapter 3 and 4 are soon to be submitted to a high-quality journal²

In Chapter 5, a summary and implications of the results presented in this thesis are given. Recommendations for further research are also given in that chapter.

²Submission is planned in form of two accompanying papers, *e.g* **1**) Peters, K., P. Stier, J. Quaas, H. Graß: Aerosol indirect effects from shipping emissions. Part I: Sensitivity studies with the global aerosol-climate model ECHAM5-HAM; **2**) Peters, K., P. Stier, J. Quaas, H. Graß: Aerosol indirect effects from shipping emissions. Part II: Comparison to satellite data. The two papers are to be submitted to *Atmospheric Chemistry and Physics*.

ANALYSIS WITH SATELLITE DATA

This chapter is accepted for publication in Journal of Geophysical Research – Atmospheres as Peters, K., J. Quaas, and H. Graßl (2011), A search for large-scale effects of ship emissions on clouds and radiation in satellite data, J. Geophys. Res., doi:10.1029/2011JD016531, in press.

It is reproduced here with editorial adjustments.

Ship tracks are regarded as the most obvious manifestations of the effect of anthropogenic aerosol particles on clouds (indirect effect). However, it is not yet fully quantified whether there are climatically relevant effects on large scales beyond the narrow ship tracks visible in selected satellite images. A combination of satellite- and re-analysis data is used here to analyse regions in which major shipping lanes cut through otherwise pristine marine environments in subtropical- and tropical oceans. The region downwind of a shipping lane is expected to be affected by the aerosol produced by shipping emissions, but not the one upwind. Thus, differences in micro- and macrophysical cloud properties are analysed statistically.

Micro- and macrophysical cloud properties as well as the aerosol optical depth and its fine mode fraction are investigated for the years 2005 - 2007 as provided for by retrievals of the two MODIS instruments. Water-cloud properties include cloud optical depth, cloud droplet effective radius, cloud top temperature and cloud top pressure. Large scale meteorological parameters are taken from ERA-Interim reanalysis data and microwave remote sensing (sea surface temperature). The regions of interest are analysed in an Eulerian- and Lagrangian sense, *i.e.* sampling along shipping lanes and sampling along wind trajectories, respectively.

No statistically significant impacts of shipping emissions on large-scale cloud fields could be found in any of the selected regions close to major shipping lanes. In conclusion, the net indirect effects of aerosols from ship emissions are not large enough to be distinguishable from the natural dynamics controlling cloud presence and -formation.

2.1 Data

Data products containing cloud- and aerosol properties as well as sea surface temperature retrieved from space-borne remote sensing, namely by instruments mounted on the EOS-Aqua and EOS-Terra polar-orbiting satellites, are used. EOS-Aqua flies in an ascending orbit with an equator crossing time of 1:30 PM, whereas EOS-Terra flies in a descending orbit with an equator crossing time of 10:30 AM.

2.1.1 Clouds, aerosols and radiation

Highly resolved cloud- and aerosol properties retrieved from both the MODIS (MODerate resolution Imaging Spectrometer) instruments are used in this study. Concerning cloud properties, cloud optical depth (τ), cloud droplet effective radius (r_{eff}), cloud top temperature (CTT), cloud top pressure (CTP), LWP and cloud fraction (Platnick et al., 2003) are used. Because this study is focused on low-level liquid water clouds and as many retrieval errors as possible should be avoided, the MODIS Level2 data are filtered to consider only (1) confidently cloudy pixels, (2) liquid water phase and (3) single-layer clouds as obtained from the MODIS quality assurance flags. Furthermore, to avoid ambiguities in the retrieved cloud microphysical quantities, only pixels in which $\tau > 4$ and $r_{\text{eff}} < 20 \mu\text{m}$ (Nakajima and King, 1990; Platnick et al., 2003) are used. By applying this filtering, about 30 – 70% of available data is discarded and a mean low-level cloud fraction >0.96 at pixel-level is obtained (similar to Kotarba, 2010). The cloud droplet number concentration (CDNC) for liquid clouds is computed from r_{eff} and τ assuming adiabaticity (Quaas et al., 2006). Concerning the calculation of CDNC, it is acknowledged that the adiabatic assumption breaks down for broken cloud fields (*e.g.* Hayes et al., 2010), but as the cloudy pixels that pass the quality filtering are very close to overcast, that assumption is seen as appropriate.

To characterise the aerosol population, the aerosol optical depth (AOD) and the fine mode fraction (FMF) of the AOD as retrieved from MODIS data are used. The FMF quantifies the part of the AOD which corresponds to particles in the sub-micron size range and is mostly associated with anthropogenic combustion aerosol (Remer et al., 2005; Bellouin et al., 2008). All the above parameters are taken from the MODIS Collection5 Joint Level2 products (MODATML2, MYDATML2). The large-scale liquid-cloud fraction is taken from the MODIS Collection5 Level3 products (MYD08_D3, MOD08_D3).

To characterise the radiative properties at the top of the atmosphere (TOA) for the regions of interest, data acquired from the CERES (Clouds and the Earth's Radiant Energy System; Wielicki et al., 1996; Loeb and Manalo-Smith, 2005) instrument and collected in the Level2 single-scanner footprint (SSF) product is

used. Only the spectrally-integrated (0.3 - 5 μm), upwelling shortwave radiative flux at TOA is used. From this, the local planetary albedo is calculated by relating the outgoing shortwave flux to the incoming solar radiation which is computed by use of the solar zenith angle of the measurement scene at the surface, the eccentricity of Earth's orbit and a solar constant of 1365 Wm^{-2} as used in the CERES retrievals. The CERES Single Scanner Footprint (SSF) product offers a spatial resolution of about $0.25^\circ \times 0.25^\circ$.

2.1.2 Meteorological environment

The local meteorological environment is characterised using both satellite- and reanalysis data. Sea surface temperature (SST) as retrieved from measurements by the AMSR-E (Advanced Microwave Scanning Radiometer - Earth Observing System) instrument, which is mounted on EOS-Aqua, is used to sample for the conditions in the lowermost troposphere. The root mean square retrieval error of the SST is estimated at $\pm 0.58^\circ\text{C}$ (Wentz and Meissner, 2000), but it is assumed that this error averages out due to the large sample size (on the order of several thousand). Additional meteorological parameters are taken from the ERA-Interim Reanalysis dataset (Simmons et al., 2007). From this dataset, the local noon model output time is used for both Aqua and Terra, assuming that this model output time is sufficient to characterise the local meteorology for both satellite overpass times. The used parameters are wind speed and -direction at 10 m height as well as the boundary layer height (BLH). ERA-Interim data are also used to calculate the lower tropospheric stability (LTS) according to Klein and Hartmann (1993). The ERA-Interim data are provided at $1.5^\circ \times 1.5^\circ$ spatial resolution. From the retrieved MODIS CTT and AMSR-E SST, an approximate cloud top height (CTH) is computed assuming a constant lapse rate of -6.5 K km^{-1} , take this as a proxy for BLH and compare it to the BLH as retrieved from ERA-Interim.

2.1.3 Ship emission inventory

The shipping emission inventory presented in Behrens (2006), representative for the year 2000, see Fig. 2.1, is used for the definition of shipping lanes which cut through otherwise pristine marine environments. In this inventory, the geographical distribution of shipping emissions is obtained by the using a combination COADS (Comprehensive Atmosphere-Ocean Data Set) and AMVER (Automatic Mutual-Assistance Vessel Rescue System) ship-traffic densities for the years 2000 and 2001/2002, respectively. COADS is maintained by the NOAA (National Ocean and Atmosphere Administration) and is a publicly available dataset of global marine surface observations. These include ship positions and ship identifiers reported

by oceangoing vessels on a voluntary basis, which can then be used for allocation of shipping emissions. AMVER is a ship reporting system on a voluntary basis to aid the rescue of people in distress at sea. This system is generally constrained to ships of size larger than 1000 gross tonnage (GT), but Endresen et al. (2003) illustrate that the AMVER ship position dataset very well represents the global cargo fleet. To distribute the annual emissions in the inventory presented in Behrens (2006), 997168 (COADS) and 993074 (AMVER) marine reports were used as input for deriving global ship reporting frequencies as illustrated in Endresen et al. (2003). The global distributions of ship reporting frequencies are shown in Dalsøren et al. (2009).

2.2 General methodology

This study is aimed at quantifying the effect of shipping emissions on clouds via a statistical analysis of satellite data. The time frame of the study is 2005 - 2007, and environments over the open oceans are analysed at a large scale. It attempts to detect an effect of shipping emissions on large-scale cloud fields, including situations in which ship tracks cannot readily be observed. The approach here therefore differs to previous satellite-data based studies on the influence of ship emissions on clouds, because these focused on clearly visible ship-tracks.

Although the change in cloud properties may not be obvious from just looking at the single cloud fields, the cloud properties in polluted regions are expected to show on average different micro- and macrophysical properties from the clouds observed in cleaner regions, if aerosol indirect effects from ship emissions are significant at a large scale. The main hurdle in this approach is the clear definition of clean- and polluted regions which still show a comparable large scale meteorology in such a way that part of the “cloud-problem”, *i.e.* the uncertain relationship between the statistics of a cloud field and ambient meteorological conditions, can be eliminated (Stevens and Feingold, 2009).

It is proposed that a definition of clear- and polluted regions is feasible with the combination of ship emission inventories and reanalysis data: if a shipping lane leads through an otherwise largely unpolluted region and if there is a mean low-level wind blowing across this shipping lane, then the air mass downwind of the shipping lane is expected to be affected by the pollution from the ship emissions, but not the air mass upwind of the shipping lane. Going in hand with the diversity of AIE hypotheses, the micro- and macrophysical cloud properties in the polluted region should then be different from those in the clean region. Then, if statistically significant, this would reveal a climatically relevant effect of shipping emissions on large scale cloud fields and subsequently radiation. It is important to note that it is not possible to sample for individual ship movements, *i.e.* one cannot discriminate

between those scenes which are polluted and those which are unpolluted.

In terms of notation in this paper, the terms “shipping corridor” or “corridor” refer to the respective region of interest including the defined shipping lane as well as the clean- and polluted regions up- and downwind of the shipping lane, respectively.

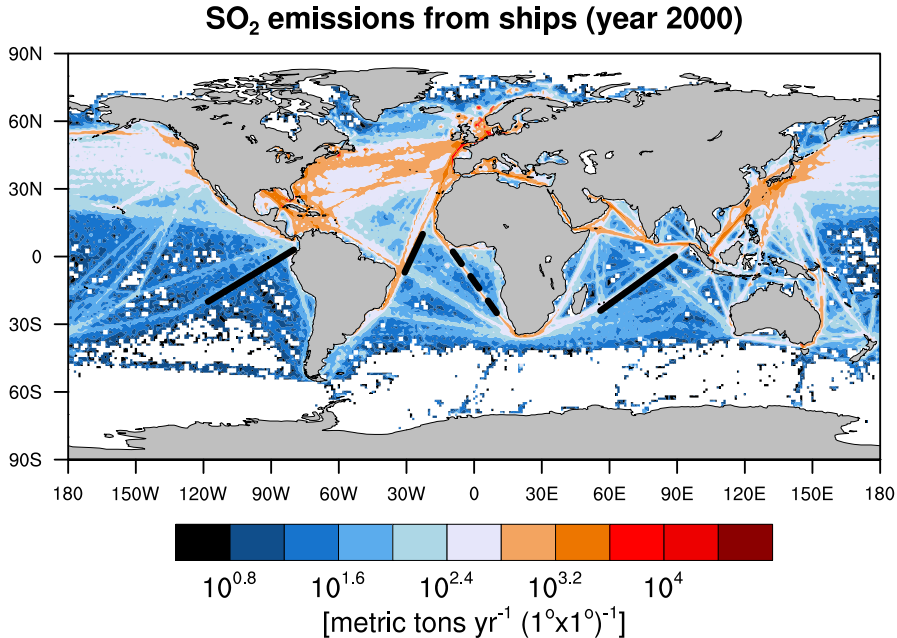


Figure 2.1: Geographical distribution of total annual SO₂ emissions from ships in the emission dataset of Behrens (2006). Colour coding is for the log₁₀ of total emissions in metric tons per year. The black lines indicate the three shipping lanes in otherwise unpolluted marine environments selected for analysis. The dashed line shows a shipping lane excluded from analysis (see Ch. 2.3)

Regions which are subject to large spatial contrast in shipping emissions are selected by visual analysis of a ship emission inventory (see Ch. 2.1.3). Also, the regions should not be situated too close to continental landmasses to avoid aerosol contamination from continental pollution, and the regions should not be subject to significant seasonal variation in wind direction, such as monsoonal circulation patterns. The choice of selected regions along with the emission profiles across these regions is shown in Fig. 2.2. As the focus of this study is on the influence of shipping emissions on clouds, three-year (2005 - 2007) mean values of water-cloud fraction as retrieved by MODIS(Aqua) are shown in Fig. 2.3 for the shipping corridors in the SE Pacific, mid Atlantic and mid Indian Oceans as illustrated in Fig. 2.1.

The region which is upwind of the respective track is defined as “clean” and the region which is downwind of the track as “polluted”. The 10m wind direction as provided by the ERA-Interim reanalysis is used to identify the areas up- and downwind of the ship track. To account for efficient vertical mixing in the

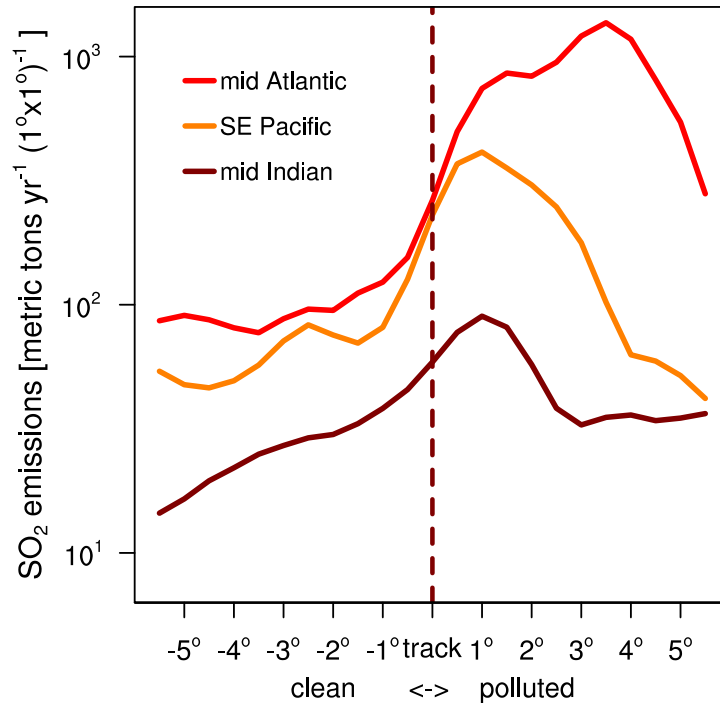


Figure 2.2: Total annual SO_2 -emissions across selected corridors in Fig. 2.1 (\log_{10} scale), as function of distance from the shipping lane (units of $^\circ$), sampled according to 10m wind direction.

boundary layer, wind directions at 925 hPa ($\approx 700\text{m}$) were compared to those at 10m and no distinct differences are found. In the selected regions, the local meteorology, especially the lower tropospheric winds, does not vary very much with time. Therefore, the regions which are defined as clean and polluted, respectively, remain the same most of the time. For example, the region south of the shipping lane in the SE Pacific is usually clean (Fig. 2.3, middle), whereas the region north of this shipping lane is usually polluted because winds are mostly south-easterly in this region. The same methodology applies for the shipping corridor in the mid Indian Ocean (Fig. 2.3). In the mid Atlantic region (Fig. 2.3, left), the boundary layer winds are mostly easterly. Therefore most of the time the area eastward of the shipping lane is clean and the area westward of the shipping lane is polluted with respect to shipping emissions. The across-corridor emission profiles shown in Fig. 2.2 illustrate the change in emissions at the point of the defined shipping lane.

Two analysis strategies which should allow to determine changes in cloud properties due to shipping emissions are developed. One approach follows a Lagrangian strategy whereas the other approach follows an Eulerian strategy. The method and results of the Lagrangian approach are shown in Ch. 2.3 whereas the method and results of the Eulerian approach are shown in Ch. 2.4.

Again a note on the notation in this paper: words similar to “changes near the intersect” refer to the area within ≈ 200 km of the intersect ($\pm 2^\circ$ for the Eulerian-

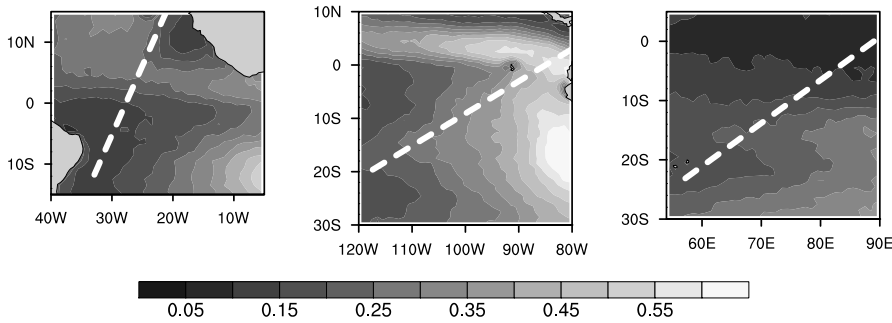


Figure 2.3: Three-year (2005 - 2007) mean water-cloud fraction as derived from operational MODIS(Aqua) Collection5 Level3 data for the regions in the mid Atlantic (left), SE Pacific (middle) and mid Indian (right) Oceans. The dashed white lines indicate the position of the windward edge of the shipping lanes analysed in each region.

and 5 hours for the Lagrangian approach).

2.3 Lagrangian approach

2.3.1 Method

The general approach to perform a Lagrangian analysis to quantify the effect of shipping emissions on clouds is illustrated in Fig. 2.4. Using wind trajectory analysis (following Sandu et al., 2010), wind trajectories which intersect a predefined shipping lane are identified. Then, clean and polluted parts of each wind trajectory can be distinguished: the part of the trajectory prior to (“upwind”) the intersection with the shipping lane is considered clean, whereas the part after (“downwind”) is considered polluted. It is hypothesised that cloud microphysical properties are different between the clean and polluted parts, due to the effect of shipping emissions. Analysing satellite data along a given wind trajectory should then reveal different cloud properties for the clean and polluted parts of the respective trajectory.

Three shipping lanes are selected for the Lagrangian analysis: (1) the shipping lane from the Panama Canal to Australia, (2) the shipping lane from the southern African tip northwestwards and (3) the mid Atlantic part of the shipping lane from Europe to South America. The selected regions are depicted in Fig. 2.5.

Second, low-level wind trajectories in these regions are analysed to find scenes, in which the boundary-layer air masses cross the respective shipping lane. The used wind trajectories are calculated using the Hybrid Single-Particle Lagrangian Integrated Trajectory Model (HYSPLIT) (<http://ready.arl.noaa.gov/HYSPLIT.php>). The trajectories for shipping lanes (1) and (2) are a subset of those used in Sandu et al. (2010). For the analysis of lane (3), low-level wind trajectories are computed analogous to the method described in Sandu et al. (2010): the wind trajectories are initialised at 200m height from nine equally spaced points inside a grid box

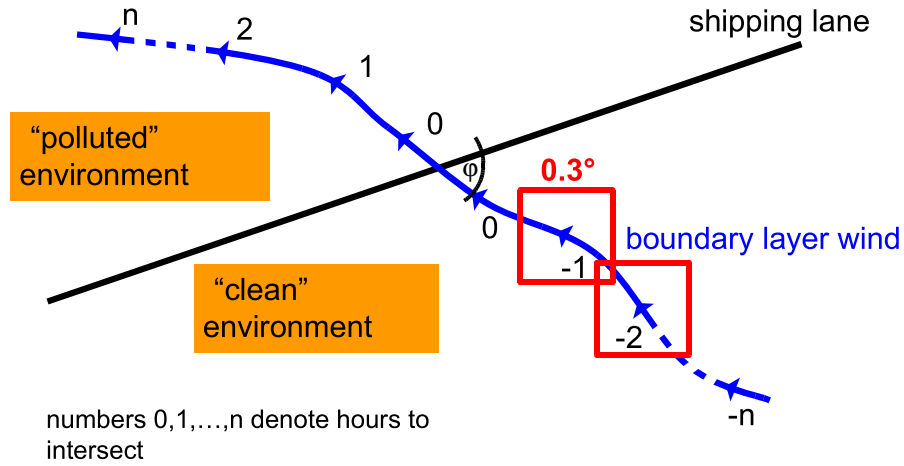


Figure 2.4: Conceptual illustration of the Lagrangian analysis concept (not to scale).

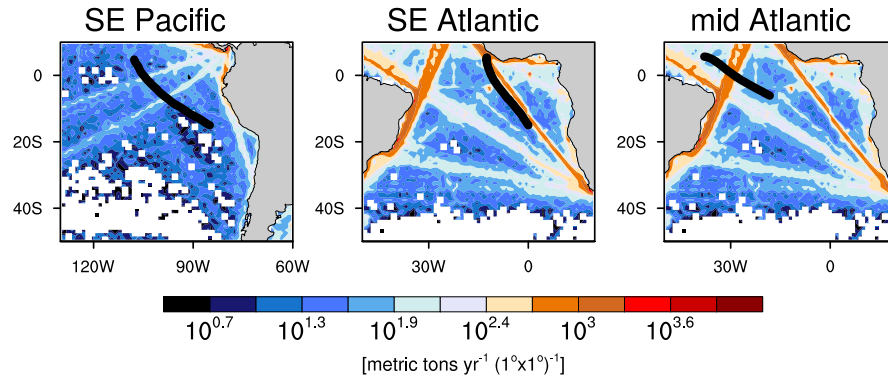


Figure 2.5: Application of the Lagrangian analysis concept. Contours show SO₂ emissions from ships as described in Behrens (2006) (Fig. 2.1). The black lines indicate the mean low-level wind trajectories for the region of interest (years 2002 - 2007).

having latitude- and longitude coordinates of the possible permutations from (2S, 5S, 8S) and (15W, 18W, 21W), respectively. These starting points are chosen to ensure the crossing of the shipping lane and the results are shown in Fig. 2.5. Here, the interest lies on whether or not a given wind trajectory intersects one of the prescribed shipping lanes. Therefore, the intersection point of each given wind trajectory is calculated by means of linear algebra. This intersection point and the respective trajectory is classified as useful for further analysis if (1) the height of the trajectory does not exceed 500m above sea level 15 hours before and 15 hours after the intersection and (2) the intersection angle is $90^\circ \pm 80^\circ$. The number of useful scenes with respect to intersection angle for each region is given in the histograms shown in Fig. 2.6. The amount of useful scenes for the southeastern Atlantic Ocean (middle panel of Fig. 2.5) is relatively small because in that region, most of the calculated wind trajectories are almost parallel to the shipping lane. Because the low number of useful scenes does not allow for sound statistics, that region is excluded from the further analysis.

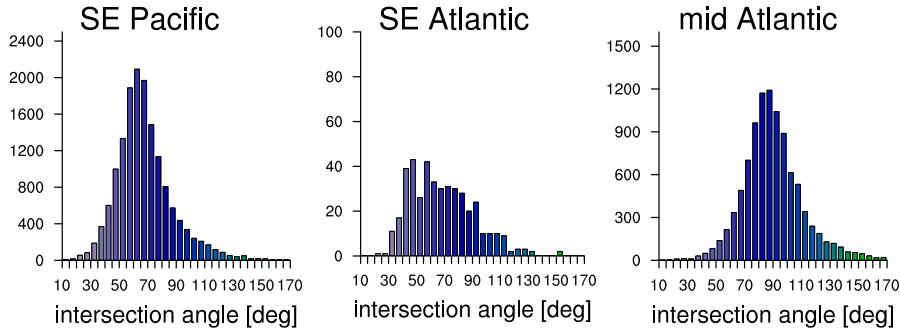


Figure 2.6: Number of useful scenes (as defined in Ch. 2.3.1) for each of the regions of interest. The number of measurements is given as function intersection angle between shipping lane and the trajectory. The total number of useful scenes is 15408, 427 and 9816 for the regions SE Pacific, SE Atlantic and mid Atlantic, respectively.

Third, aerosol- and cloud properties are analysed along the useful trajectories. Not all trajectories categorised as “useful” by the above analysis are used, but only those whose intersection times fall within a time window which matches the satellite overpass times. These time windows are defined as 10 – 17 UTC for the mid Atlantic and 14 – 22 UTC for the SE Pacific region. After applying this time-window filter, the number of useful trajectories is 3284 for the SE Pacific and 2486 for the mid Atlantic region. Because the trajectory model delivers hourly output of trajectory location, satellite data can be sampled at every hour of the trajectory. The analysis is restricted to the trajectory locations 15 hours before and 15 hours after the intersect with the shipping lane. The 15 hours before and the 15 hours after the intersect will from now on be termed as “clean” and “polluted” areas, respectively. Satellite data is analysed for a $0.3^\circ \times 0.3^\circ$ grid box which is centered around a given trajectory point (as illustrated in Fig. 2.4). All valid satellite pixels within a $0.3^\circ \times 0.3^\circ$ box for a particular observation time are averaged to represent a daily average. This leads to 15 daily averages (one for each hourly trajectory position) for each of the two parts of the wind trajectory (“clean” or “polluted”). The results are then averaged for all trajectories crossing the respective shipping lane, which gives a long-term mean value for each hourly trajectory position. Because the obtained parameter distributions are not normally distributed, the error is estimated separately for observations having larger/smaller values than the respective mean value: the mean upper/lower difference to the mean value is divided by \sqrt{N} , with N being the respective number of observations having a larger/smaller value than the mean.

2.3.2 Results

2.3.2.1 SE Pacific region

Results of the wind trajectory analysis for the SE Pacific region are shown in Fig. 2.7 as function of time to the calculated intersect with the shipping lane. SST increases by about 0.5 K, LTS is reduced by about 1.2 K and a reduction of the BLH by about 140 m along the mean wind trajectory is observed. Thus, although the MBL gets slightly more unstable along the trajectories, BLH as diagnosed from the re-analysis as well as the BLH-proxy from MODIS CTT is reduced; the BLH-proxy suggests a substantially higher MBL, though, which is also consistent with the results of Wood and Bretherton (2004).

Along the mean trajectory, the number of MODIS pixels valid for analysis per $0.3^\circ \times 0.3^\circ$ averaging domain is slightly reduced for the cloudy scenes, but stays about constant for pixels having valid aerosol retrievals. The retrieved cloud- and aerosol properties mostly show the same patterns for both instruments. If applicable, differences are explicitly mentioned in the following. The retrieved AOD shows a slight and rather constant increase along the trajectories with the ones retrieved from MODIS(Terra) having an offset from the ones retrieved from MODIS(Aqua) (this is a known issue of MODIS Collection 5, (Remer et al., 2008)). The retrieved FMF shows increasing values for both instruments, with the values retrieved from MODIS(Terra) being substantially higher than the ones from MODIS(Aqua) (which is on the order of the oceanic background level (Remer et al., 2008)). This is interesting because the slight increase in the FMF could indicate an influence of shipping emissions on MBL aerosol composition. The calculated CDNC also increases and for the LWP, the retrievals by the two instruments lead to different along-trajectory gradients: the LWP slightly decreases for MODIS(Terra) and slightly increases for MODIS(Aqua). Although these changes appear systematic, the relative change is only on the order of 3 %. In combination with the retrieved gradients in AOD, FMF and CDNC, the data retrieved from both instruments could indicate a first aerosol effect. However, a reduction of CTH, manifested in both the BLH-proxy from retrieved CTTs as well as decreasing cloud top pressure (CTP, not shown; derived from a combination of MODIS measured brightness temperatures and NCEP reanalysis data; Platnick et al. (2003)) is also obtained. Assuming an adiabatic cloud droplet effective radius (r_{eff}) profile, the retrieved along-trajectory decrease of r_{eff} -values is consistent with the reduced CTHs.

Thus, the apparent change in calculated CDNC may very well have its cause in cloud dynamics, which outweighs any arguments advocating the first aerosol indirect effect as it is just of second order importance for cloud formation and -properties. Furthermore, evidence of shipping emissions in the retrieved aerosol

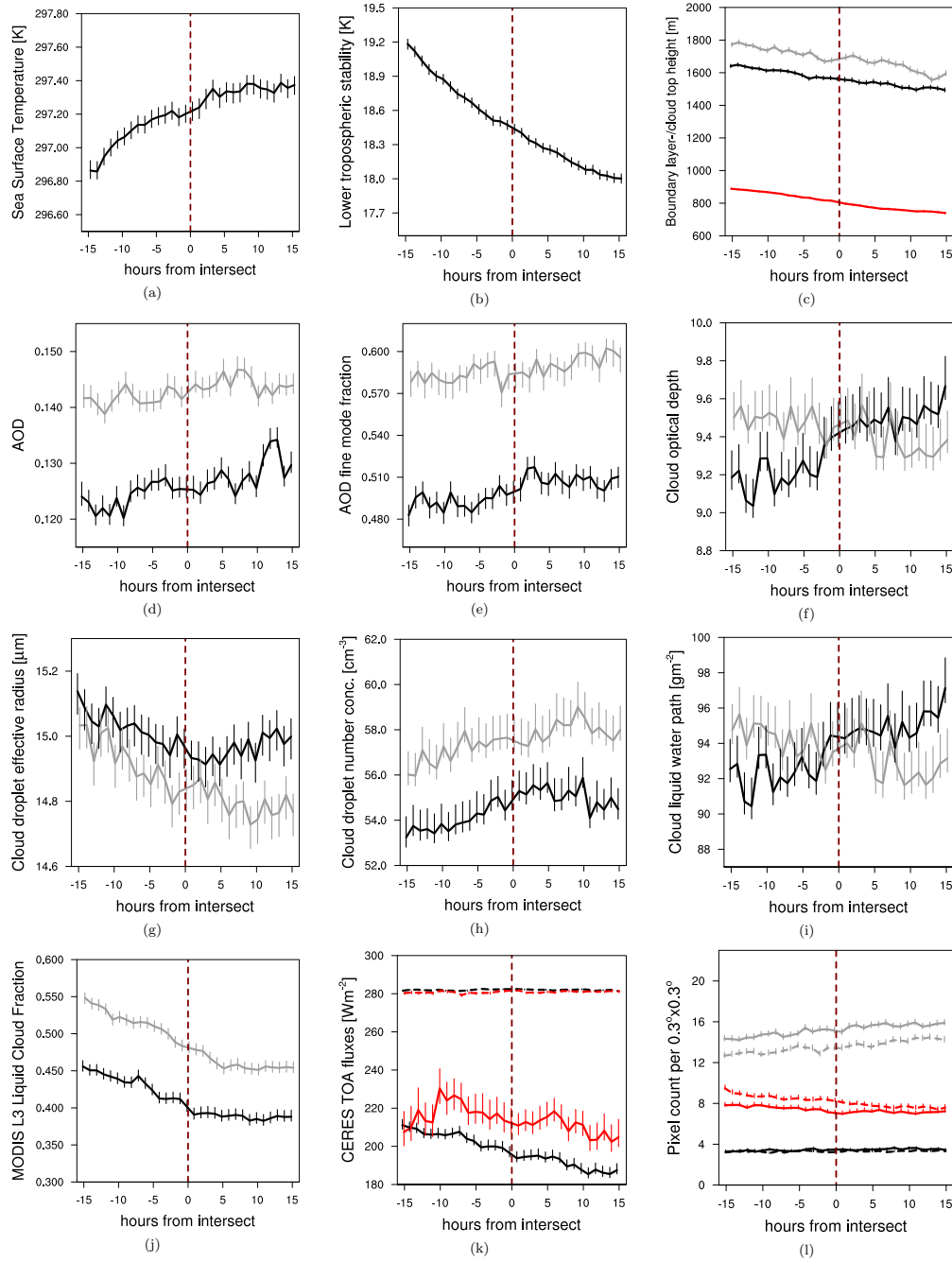


Figure 2.7: Three-year mean values of the Lagrangian trajectory analysis for the SE Pacific region, aerosol- and cloud parameters: (a) SST; (b) LTS; (c) boundary layer- and cloud top height derived from ERA-Interim (red) and MODIS cloud top temperatures (black, grey), respectively; (d) AOD; (e) AOD fine mode fraction (FMF); (f) τ ; (g) r_{eff} ; (h) CDNC; (i) LWP; (j) cloud fraction, (k) outgoing SW- and LW fluxes and (l) pixel count statistics for each $0.3^\circ \times 0.3^\circ$ box. For Figs. (c) - (j), the black and grey curves represent data from MODIS on Aqua and Terra, respectively. In Fig. (k), the solid- and dashed curves represent the reflected shortwave and outgoing longwave fluxes from CERES; black and red denote all- and cloudy sky values, respectively. In Fig. (l), the red- and black lines show valid cloud- and aerosol retrievals, respectively; grey denotes invalid pixels with respect to cloud filtering; solid- and dashed lines denote retrievals from Aqua and Terra, respectively. The error bars denote the confidence in the calculated mean value towards higher/lower values (see Ch. 2.2). The curves are shifted with respect to each other along the x-axis to avoid overlapping. 19

properties is essential for concluding an observed first indirect effect. But no systematic change in retrieved AOD and its FMF is found near the intersect with the shipping lane. The obtained increases of both properties are most probably associated with the oceanic background aerosol concentrations and a direct aerosol effect (DRE) due to shipping emissions is thus not found.

Although the measurement setup allows for reducing the influence of meteorological variability, such as distinct seasonal- and inter-annual changes in the large-scale circulation, the sampling along a gradient of increasing SSTs cannot be avoided. Because the focus of this study are low liquid-water clouds residing in or slightly above the MBL, the mean cloud-top characteristics of these clouds are bound to be affected by the slight change in SST along the trajectories. This is reflected in the retrieved gradients of low-level cloud fraction. The TOA radiative fluxes as retrieved from CERES(Aqua) correlate well with the retrieved cloud-fraction gradients: the shortwave part decreases in along-trajectory direction and there is no indication of a distinct change near the intersect. It is therefore not possible to isolate a microphysical effect of shipping emissions on clouds, and therefore on the TOA radiation budget, from the statistical analysis for the region investigated.

2.3.2.2 Mid-Atlantic region

The results from the wind trajectory analysis for the shipping lane in the mid-Atlantic region as a function of time from the intersect are displayed in Fig. 2.8. The sea surface temperature as retrieved from the AMSR-E instrument increases by about 0.2 K, the LTS decreases slightly by about 0.1 K and the boundary layer height as retrieved from the re-analysis decreases by about 60 m along the trajectories. However, the BLH-proxy using MODIS retrieved CTTs shows substantially higher values and also increases along the mean trajectory. As shown for the SE Pacific region, the results for the BLH-proxy most probably represent the MBL height more closely. Therefore, the increase in SST results in a slight destabilization of the lower troposphere which in turn leads to an increase in BLH and CTH. This is also confirmed by reduced CTP (not shown).

For the MODIS retrieved cloud- and aerosol properties, the two sensors show similar along-trajectory gradients with MODIS(Terra) values mostly slightly higher than the ones from MODIS(Aqua). The number of valid pixels available for analysis is approximately the same for both cloud and aerosol properties. This implies that the filtering for useful pixels discards a substantial amount of potentially cloudy pixels because these are available at 5×5 km² resolution, whereas aerosol properties are available at 10×10 km². The AOD steadily increases along the wind trajectories by about 10%, but the FMF is about constant throughout the mean trajectory. As for the SE Pacific region, thus, ship emission aerosol

are not distinguishable in the column aerosol concentrations as represented by the retrieved AOD, which also implies that there is no aerosol DRE of shipping emissions in this region. The calculated mean CDNC and LWP are also approximately constant in along-trajectory direction which reflects no distinct change in r_{eff} and τ in along-trajectory direction. Thus, no first indirect effect is visible either. However, systematic gradients in more macrophysical cloud field properties are still obtained: the cloud fraction increases by about 4% and CTP decreases by about 20 hPa (not shown). So for the trajectories analysed in this region, the mean large scale cloud fraction slightly increases and the increase in CTH matches the reduced LTS values in along-trajectory direction. The retrieved TOA radiative fluxes also show no distinct change near the intersection point but match the gradient in cloud fraction: SW-fluxes increase and LW-fluxes decrease in along trajectory direction.

Therefore, although the AOD shows an increase on the order of 10 % in the along-trajectory direction, there is no evidence of an influence of shipping emission on either the properties of the MBL-aerosol composition or on the properties of low-level liquid water clouds in this region. Nevertheless, large-scale cloud field properties like the mean CTH and cloud fraction show distinct gradients; these can be explained by the gradient in the meteorological conditions, *i.e.* the increase in SSTs and subsequent destabilisation of the lower troposphere.

2.4 Eulerian approach

2.4.1 Method

For the Eulerian perspective, averages are calculated along straight lines which are define parallel to the respective shipping lane. These have the same length as the shipping lane and are shifted in equal steps orthogonal to the shipping lane. The shift between each straight line is 0.5° and there are seven of these straight lines up- and downwind of the shipping lane, *i.e.* the sampling covers the area 5.5° up- and downwind of the shipping lane. The concept is illustrated in Fig. 2.10. It is hypothesised that the mean MBL-composition in the area downwind of the shipping lane is more polluted from shipping emissions than the area upwind. Therefore, the retrieved cloud- and aerosol properties should be different in such a way that their change in across-corridor direction can be associated with the shipping emissions at the position of the shipping lane. The sampling is done only for days where the 10 m wind obtained from the ERA-Interim re-analyses blows in the predominant direction, to assure that the definition of up- and downwind remains consistent.

The geophysical data of interest are collected along these straight lines in such a way that the data fall into squares of 0.3° edge length, *i.e.* each straight line is

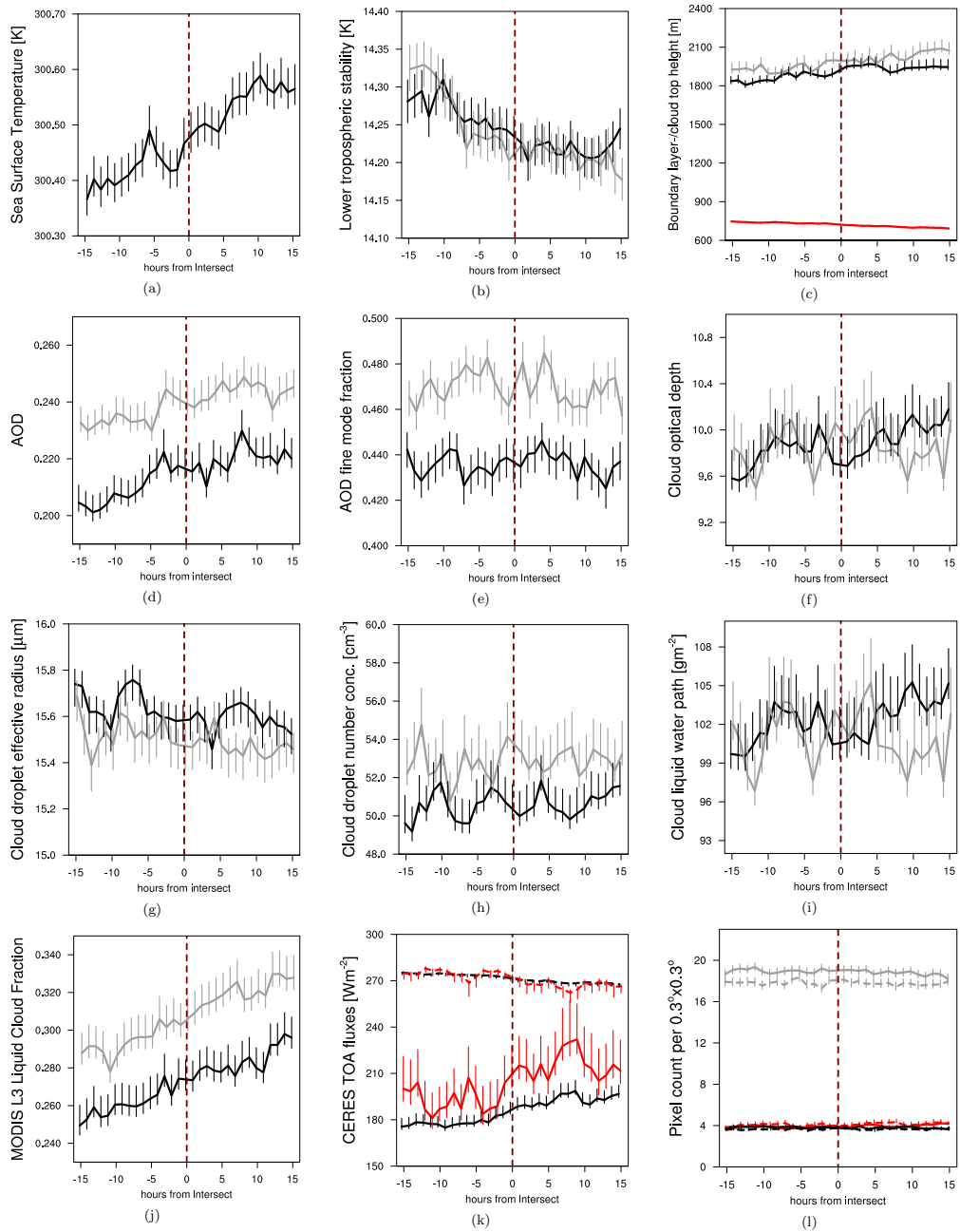


Figure 2.8: As Fig. 2.7, but for the Mid-Atlantic region.

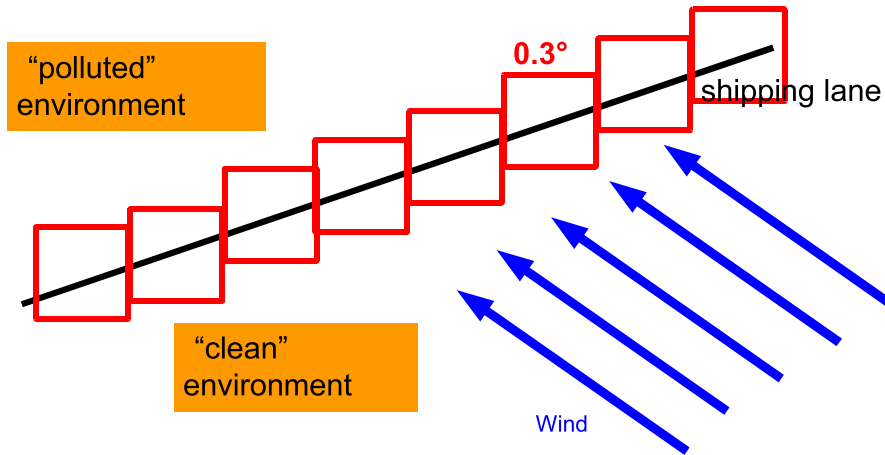


Figure 2.9: Conceptual illustration of the Eulerian analysis concept (not to scale).

overlain by a certain number of squares which have a 0.15° overlap to either side of the line (see Fig. 2.9). The edge-length of 0.3° is chosen to ensure that there is no data overlap between two neighbouring lines. The average is then calculated over all measurements falling into each square. Because sampling is performed on a daily basis, the local meteorology can be assumed as being roughly similar in the region of interest.

The main advantage of this Eulerian perspective over the previous Lagrangian one is that a much larger amount of data can be investigated. The aim here is to average over even more situations to potentially average out “noise” due to the natural variability in the large-scale meteorology, which was found to mainly drive the variability in the boundary-layer clouds. Thus, it is not necessarily expected to obtain identical results for both approaches. For the Lagrangian approach, the sampling is only performed along a uniquely defined wind trajectory and exclude all other data from a particular day. By this, the data is strictly filtered prior to the final analysis. For the Eulerian approach, on the other hand, all data from the shipping corridor are analysed on a daily basis. By this, the data are less filtered compared to the Lagrangian approach, a much larger area is covered and the spectrum of possible observed situations is broader. This may give differences in the observed aerosol- and cloud properties. The method for deriving the mean values and respective error estimates is the same as that described for the Lagrangian approach (see Ch. 2.3.1).

2.4.2 Results

2.4.2.1 SE-Pacific Ocean

For the SE-Pacific region, the analysis covers that part of the shipping lane which extends from 118°W - 100°W . Any data eastward of 100°W is excluded because there the environmental conditions do not guarantee similar conditions with respect to

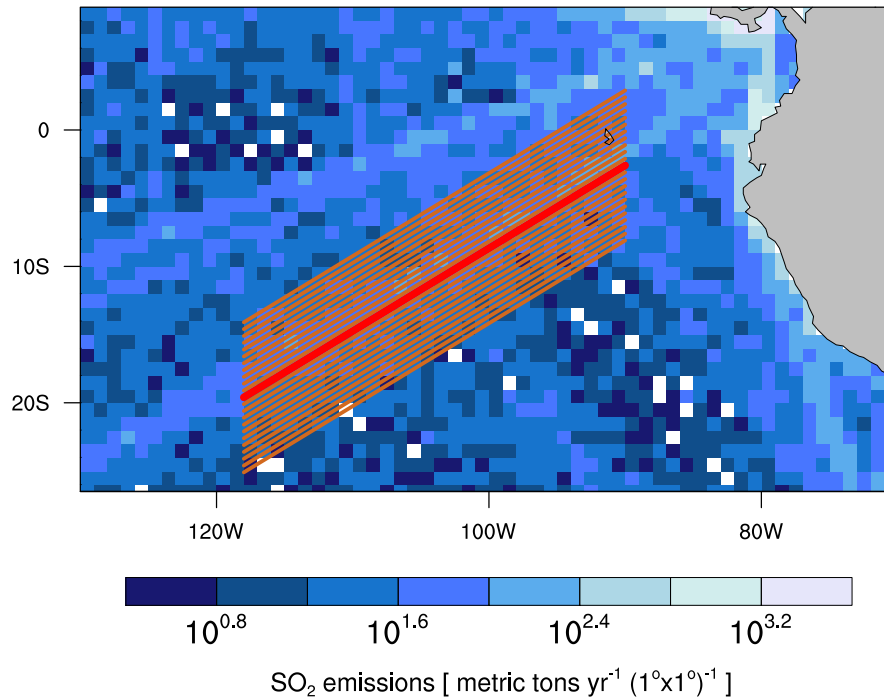


Figure 2.10: Illustration of the Eulerian analysis concept demonstrated for the shipping lane in the SE-Pacific Ocean region. The thick red line is the shipping lane. Cloud- and aerosol properties for the “clean” and “polluted” regions are sampled along the thin lines to the south and the north of the shipping lane, respectively. The colour map denotes annual mean sulphur dioxide (SO_2) emission as provided by the shipping emissions inventory (Behrens, 2006).

the more westward part of the shipping lane. The SST-gradient, in particular, shows varying patterns: SST first increases in the clean part, and then decreases in the polluted part. For the region spanning 118W - 100W, SST continuously increases in across-corridor direction. Additionally, the retrieved cloud properties eastward of about 95W are influenced by the Galapagos Islands (different MODIS algorithm for land surfaces), and most satellite pixels do not pass the filtering for ice- and multi-level clouds eastward of about 85W, which is probably associated with deep convection in close proximity to the ITCZ. Furthermore, data taken eastward of 90W would be too close to continental South America.

It is mostly because of this spatial restriction that different characteristics of the observed aerosol- and cloud distributions are obtained with the Eulerian- compared to the Lagrangian approach shown in Ch. 2.3.2.1. In the Lagrangian approach, most of the trajectories cluster in the longitudinal band of 90W - 105W. Furthermore, as the averaging direction of the Lagrangian approach was rather zonal (wind directions $\approx 110^\circ$ - 120°), the results from the Eulerian analysis reflect the zonally-averaged meridional gradient across the shipping corridor. Therefore, there is little overlap among the two analysis approaches in both the sampled region and averaging procedure. This then leads to different statistical results

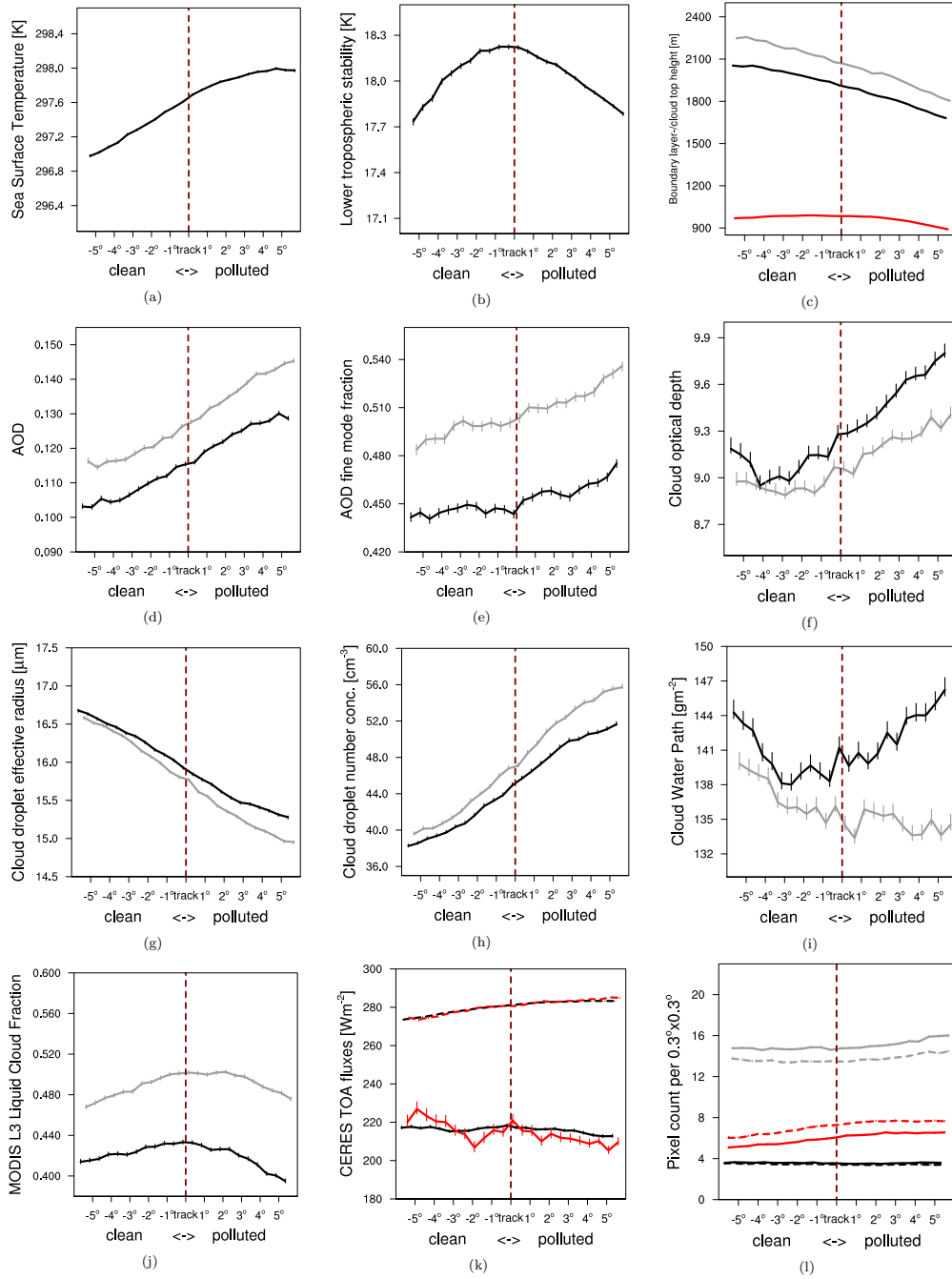


Figure 2.11: As Fig. 2.7, but applying the Eulerian sampling method.

among the two methods. Nevertheless, the main conclusions remain untouched by this.

Three-year across-corridor average values of selected meteorological parameters and cloud properties as function of distance to the shipping lane are shown in Fig. 2.11.

For the corridor extending from 118W to 100W, an annually persistent increase in SST from the clean- to the polluted area is found. The LTS exhibits a maximum close to the shipping lane with the values on the clean- and polluted sides being

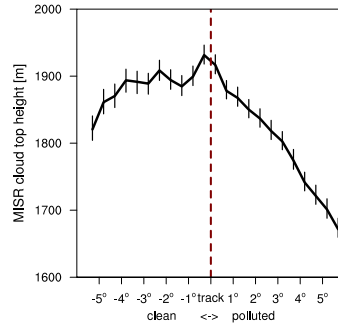


Figure 2.12: Cloud top heights of low (liquid water) clouds as retrieved from the MISR aboard Terra for the SE-Pacific region. Data is from the months September - November of 2005-2007. The error bars denote the confidence in the calculated mean value towards higher/lower values (see Ch. 2.2).

lower by ≈ 0.5 K. The BLH as obtained from the re-analysis is approximately constant throughout the clean side of the corridor and then decreases by about 10% on the polluted side. The BLH-proxy values suggest (1) a constant decrease in BLH in across-corridor direction and (2) a much deeper boundary layer than the BLH values obtained from the re-analysis. So as for the Lagrangian approach, the LTS does not follow the general increase in SSTs which would suggest a destabilisation of the lower troposphere.

Unlike for the Lagrangian approach, the number of valid cloudy pixels available for analysis per $0.3^\circ \times 0.3^\circ$ box increases in across-corridor direction; but the ratio of valid- vs. invalid pixels is nevertheless small. Similar to the Lagrangian approach, the AOD is found to systematically increase by about 20% from the clean- to polluted side of the sampled region, and AODs retrieved from MODIS(Terra) are also higher than those from MODIS(Aqua). The FMF associated with the AOD is on the order of the oceanic background value (Remer et al., 2008), and slightly increases towards the polluted side of the shipping corridor. Whether or not this relative increase in small-particle extinction in across-corridor direction can be associated with shipping emissions is not clear; it is also present in the results from the Lagrangian analysis, though. Similar to the results found for the Lagrangian approach, the systematic increase in total AOD cannot be linked to shipping emissions. Therefore, there is also DRE detected from the Eulerian approach.

The calculated CDNC substantially increases in across-corridor direction with the values obtained from MODIS(Terra) ($\approx 40\%$) being slightly higher than those from Aqua ($\approx 36\%$). The LWP shows different patterns in across corridor directions for the two instruments: while the LWP continuously decreases for data from Terra, it first de- and then increases for Aqua; these changes in LWP are within a range of 5% though and may be attributed to the diurnal cycle of shallow convection. The same holds for the liquid cloud fraction as obtained from the MODIS Level3

product. Compared to the results from the Lagrangian analysis, the gradients in retrieved cloud properties between the clean- and polluted sides of the shipping corridors are much larger here.

From these data alone, one could state having isolated an aerosol indirect effect from shipping emissions in this shipping corridor. To further corroborate the analysis, changes in CTH of the sampled cloud fields are also analysed. The MODIS retrieved CTP values (not shown) show a pattern consistent with the BLH: they are relatively constant in the clean- and then increase on the polluted side of the corridor. Therefore, the change in CTH as deduced from MODIS data is most probably due to dynamical drivers.

Recently, it has been investigated that MODIS-retrieved CTP values suffer from severe underestimation (*i.e.* CTH overestimation) under specific meteorological conditions (Ludewig, 2011). Therefore, a check for CTH as retrieved from MISR and CALIPSO measurements is performed and similar across-corridor patterns for the three instruments (MISR CTH in Fig. 2.12, CALIPSO CTH not shown) are found; MISR and CALIPSO CTHs show very good agreement. As CALIPSO retrieved CTH is often used as a reference, it is concluded that the CTH-gradient retrieved from MODIS is a robust result.

Overall, the analysed data suggest a first indirect aerosol effect: an increase in AOD and associated FMF is accompanied by increased CDNC and almost constant LWP. Furthermore, to maintain the approximately constant or even increasing LWP values in across-corridor direction with decreasing CTH, the cloud base height should decrease as well because the vertical extent of the clouds should remain about the same. Then, the decrease in MODIS retrieved r_{eff} can only be explained by an overall shift of the r_{eff} -profile towards smaller sizes. There is, on the other hand, no evidence at all for a cloud lifetime effect (cloud fraction decreases rather than increases), and also CTHs decrease rather than increase. Most importantly, no discernible effect is visible in the radiation - the dominant influence on it is the change in cloud fraction, opposite to the expected aerosol indirect forcing.

2.4.2.2 Mid-Atlantic Ocean

Just as for the analysis of the SE Pacific region, the analysis is not done along the whole latitudinal extent of the shipping lane. Data southward of 5S is excluded because of possible “landmass contamination” and northward of 2N because of an increasing number of observations being filtered out due to ice-cloud presence. For the Lagrangian approach (see Ch. 2.3.2.2), most trajectories cluster in the latitudinal range of 3S - 3N. Therefore, the sampled region discussed here is shifted slightly southward compared to the Lagrangian approach and the results of the analysis are shown in Fig. 2.13.

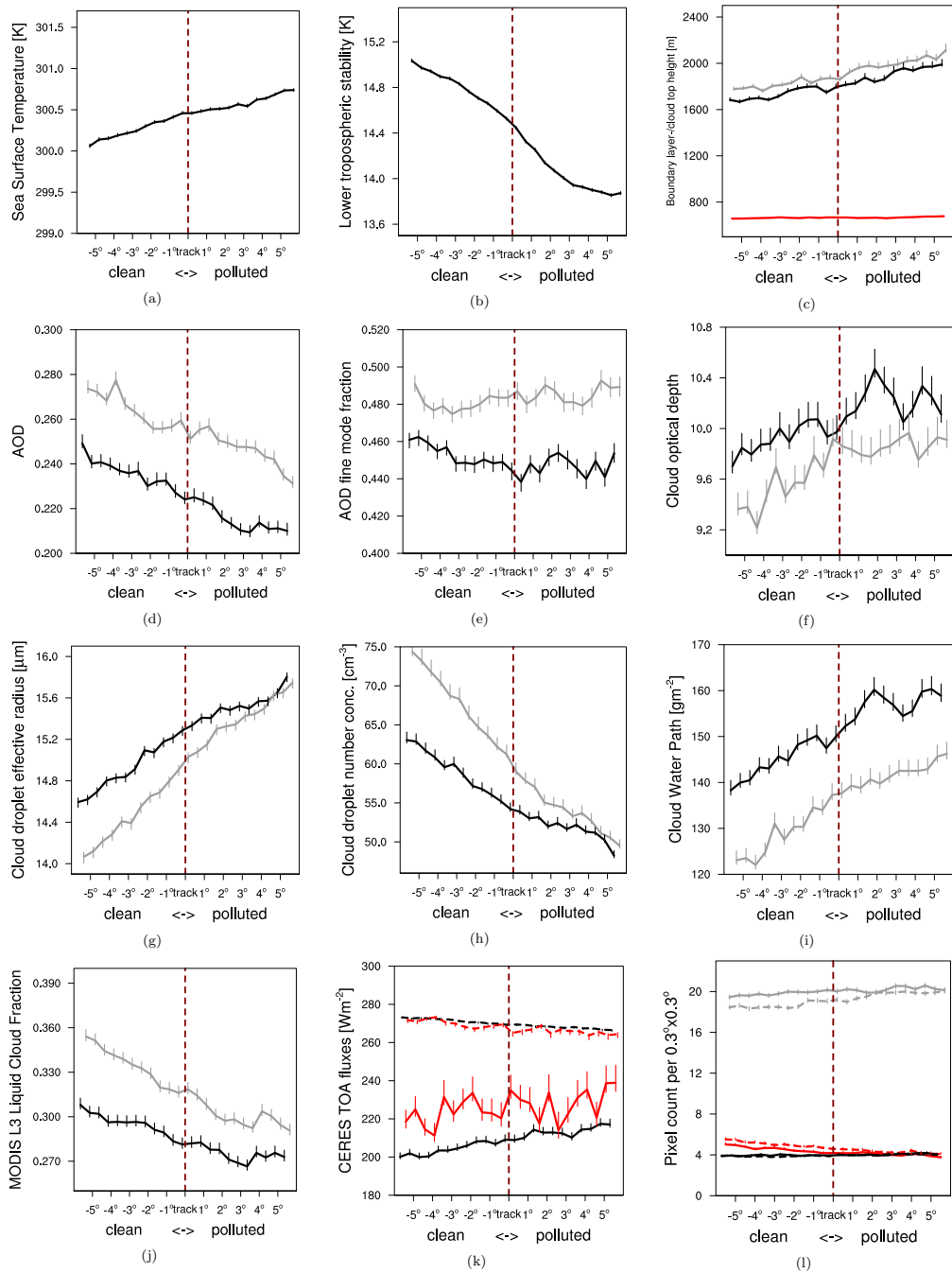


Figure 2.13: As Fig. 2.8, but applying the Eulerian sampling method.

Similar to the results obtained from the Lagrangian analysis, the SST increases by about 0.5 K from the clean to the polluted side of the corridor. This across-corridor SST-gradient is subject to inter-seasonal variability within the uncertainty range given. The LTS as obtained from the reanalysis-data decreases from ≈ 15 K to ≈ 14 K and the BLH as obtained from the re-analysis correspondingly slightly increases in across-corridor direction. The calculated BLH-proxy values again indicate a distinctly deeper boundary layer and the across-corridor increase in BLH is also more pronounced than in the re-analysis data. Interestingly, this is partly in contradiction to the results from the Lagrangian approach: there, the LTS also decreases, much lesser though (≈ 0.1 K), but the BLH slightly increases (≈ 20 m).

The observed gradients in across-corridor direction are similar for both MODIS sensors and as for the Lagrangian approach, the number of valid pixels is about the same for both cloud- and aerosol retrievals. The AOD decreases over the whole shipping corridor by about 10% (Lagrangian approach: increasing AOD), with the AOD retrieved from MODIS(Terra) showing the previously mentioned offset to MODIS(Aqua). Therefore, there is no aerosol DRE from shipping emissions detectable in this region also. The AOD FMF is almost constant in across-corridor direction at approximately the oceanic background value as shown in Remer et al. (2008). This is particularly interesting because the ship emissions inventory used in this study shows the highest shipping emissions of the three corridors under investigation for the region of the mid-Atlantic Ocean (Fig. 2.2).

The liquid cloud fraction as retrieved from the aggregated MODIS Level3 product shows a constant decrease across the shipping corridor with values around 0.3 indicating rather broken trade cumulus cloud fields. This is the same order of magnitude as found with the Lagrangian approach; there, the cloud fraction increases though. The r_{eff} increases by about 10% which also holds for τ . The calculated CDNC-values show a significant decrease ($\approx 23\%$ - 33%) in across-corridor direction and the LWP increases across the whole corridor (Lagrangian approach: CDNC and LWP about constant). This is accompanied by an increase in CTH.

The results obtained from this analysis approach indicate that nothing more than a change in mean cloud properties associated with an increase in SST is sampled (*e.g.* Betts and Ridgway, 1989). The important measure in this regard is the change in CTH across the shipping corridor. All other results follow from this: assuming no change in cloud base height, the increase in CTH leads to increased cloud geometrical thickness, LWP and τ . Keeping the adiabatic r_{eff} profile in mind, it is deduced that the increase in the retrieved r_{eff} is associated with the increased cloud geometrical thickness. The results for CERES TOA radiative fluxes also support this finding: the shortwave flux increases and the longwave flux decreases along the mean trajectory. Clouds get more reflective

along the trajectories sampled, which explains the increased shortwave fluxes. The clouds also have higher cloud tops with lower cloud temperatures, which explains the along-trajectory reduction of the outgoing TOA longwave fluxes. Therefore, the observed across-corridor change in cloud properties are not associated with shipping emissions. The observed gradient can be solely explained by the observed meteorological conditions of this region. This is also in line with the finding that the AOD decreases and that the FMF stays about constant in across-corridor direction. Because one would expect a somewhat pronounced signal in the AOD and its FMF due to the across-track gradient in shipping-emissions (see Fig. 2.2), these results shed light on the difficulties of determining aerosol indirect effects in dynamically active cloud regimes.

Interestingly, the results obtained for this region differ greatly between the two statistical analysis approaches. For the Eulerian approach discussed in this section, not such stringent dynamical constraints as for the Lagrangian approach are applied, *e.g.* such as that a “useful” trajectory must not exceed a height of 500 m above sea level which by common sense excludes highly convective environments. Therefore, it is possible that distinctly different lower tropospheric conditions are sampled between the two approaches.

2.4.2.3 Mid-Indian Ocean

For the shipping corridor in the mid-Indian Ocean, only data in the range from 56E to 75E is sampled because (1), data westward of 60E would be influenced by Madagascar and Mauritius and (2), the across-corridor mean cloud properties eastward of 75E are significantly different from those in the rest of the corridor. Furthermore, data from the northern hemispheric winter season (DJF) is excluded because the mean wind direction in across-corridor direction in this season differs distinctly from that obtained for the other seasons. This is due to the circulation patterns associated with the Indian winter monsoon. As for the other two regions, three-year mean values of selected meteorological quantities as well as cloud- and aerosol properties as a function of distance from the shipping lane in the mid-Indian Ocean are shown in Fig. 2.14.

Similar to the other two shipping corridors under investigation, an annual persistent increase in SST across the corridor of almost 2 K, which is the largest change in across-corridor SST amongst the three analysed shipping corridors. The LTS decreases by about 0.7 K and the BLH also decreases by more than 200 m. Like for the other two regions, the BLH-proxy values suggest a substantially deeper MBL than that obtained from the re-analysis. Furthermore, the proxy values suggest a rather constant BLH whereas the re-analysis data suggest a constant decrease in across-corridor direction.

For this corridor, the results are mostly consistent among the two MODIS sen-

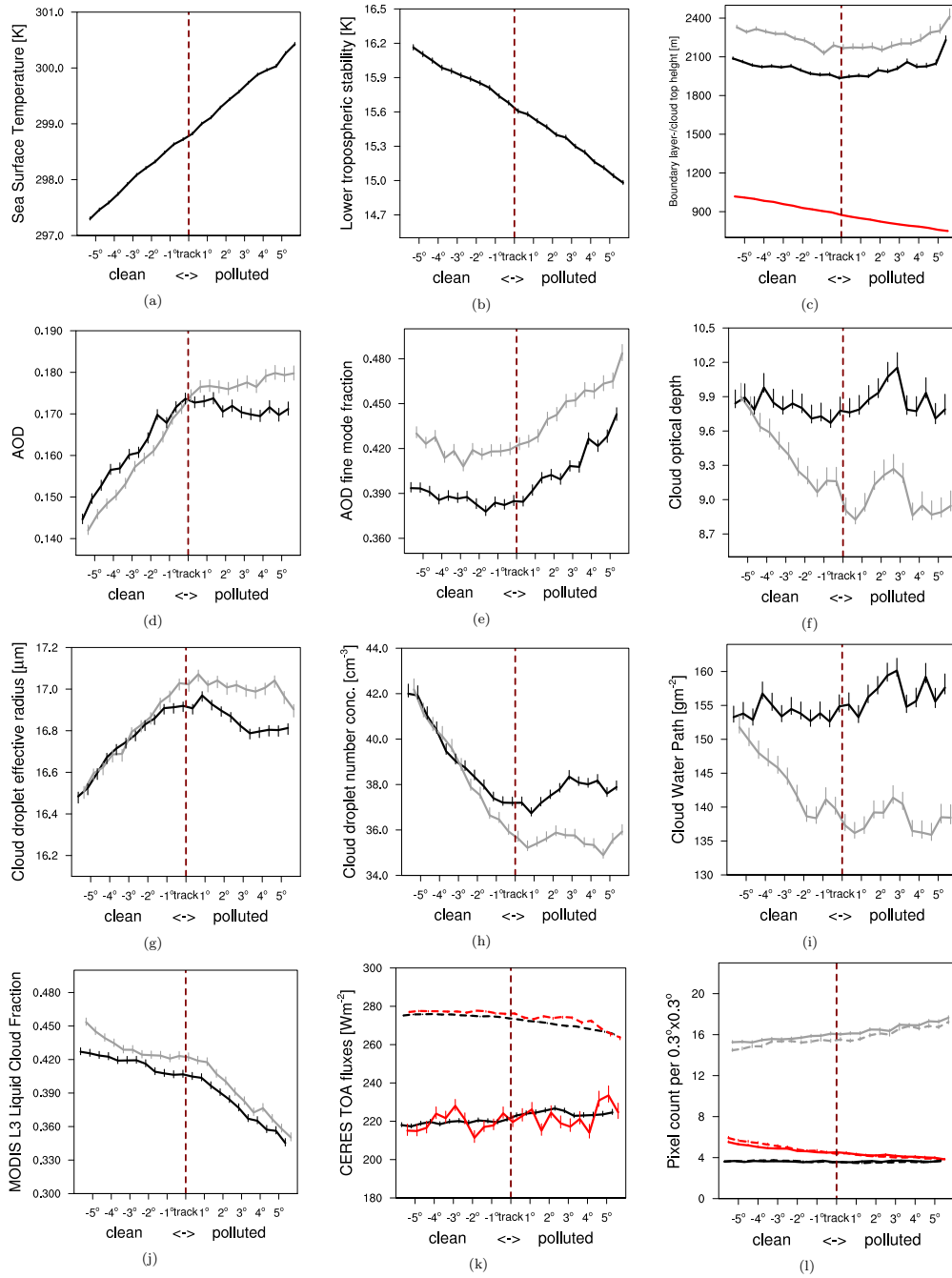


Figure 2.14: As Figs. 2.11 and 2.13 but for the mid-Indian Ocean region.

sors if not mentioned otherwise. The number of pixels per $0.3^\circ \times 0.3^\circ$ box available for analysis of cloud properties slightly decreases in across-corridor direction and converges to the number of available aerosol retrievals. Near the location of the shipping lane, both the AOD and its FMF show a change in across-corridor gradient: the AOD peaks or levels off and the FMF increases from thereon. These gradients are similar for both datasets which gives confidence in this result and implies no aerosol DRE from shipping emission in this region also.

The gradient in CDNC values shows decreasing values ($\approx -(12\% - 17\%)$) in the clean part followed by a leveling-off or even a slight increase in the polluted part of the shipping corridor. The analysis of the retrieved τ and derived LWP reveals the largest differences between the two instruments: τ and LWP as retrieved from MODIS(Aqua) stay about constant or increase in across-corridor direction whereas the same parameters retrieved from MODIS(Terra) measurements rather decrease on the clean- and then stay approximately constant on the polluted side. The liquid cloud fraction decreases by about 10% in across-corridor direction with the largest part of this reduction occurring on the polluted side of the corridor.

The most interesting analysed quantity for this region is the FMF of the observed AOD. With a distinct but not large increase from the position of the shipping lane into the polluted side of the shipping corridor. So in here, it may be the case indeed scenes in which the size distribution of the aerosol population has changed due to shipping emissions were sampled. Nevertheless, it remains an open question, why the retrieved AOD increases throughout the clean side of the shipping corridor and then levels off on the polluted side. The across-corridor gradients of the calculated CDNC also show a distinct change near the point of the shipping lane: the profiles levels-off. Therefore, CDNC correlates negatively with the retrieved AOD whereas a positive correlation would generally be expected when considering the “Twomey-effect”. Nevertheless, this negative correlation could very well be the background conditions of this region and shipping emissions at the shipping lane disturb these conditions. From this perspective, the relative increase in small particle numbers then leads to altered cloud properties. Interestingly, the all-sky TOA shortwave radiative fluxes show an increase larger than the mean gradient near the point of the shipping lane.

So overall, the analysis of the mid-Indian Ocean shipping corridor reveals apparent correlations between observed aerosol and cloud properties. These could be indicative of a first indirect effect from shipping emissions but dynamical drivers cannot be ruled out: the across-corridor increase in SST is the largest among the three analysed regions. From this point of view, it is interesting that not a more significant change in cloud macrophysical properties is derived because a distinct increase in CTH should be observed from the observed 2 K increase in SST (*e.g.* Betts and Ridgway (1989)).

2.5 Summary and Conclusions

To investigate the influence of shipping emissions on climatically relevant scales, satellite- and reanalysis data were used to sample parameters characterising the cloud, aerosol and radiative properties as well as the large-scale meteorological conditions of several remote oceanic regions. These remote oceanic regions were selected according to the following criteria: 1) a well-defined shipping lane leading through an otherwise pristine environment is present, 2) the mean low-level wind directions are not too close to being parallel with this shipping lane and 3) the so-defined shipping corridor is not subject to significant pollution advected from a nearby landmass. This definition fits three shipping corridors which were then selected for analysis: 1) the SE-Pacific Ocean with the shipping lane from the Panama Canal southwestward, 2) the mid-Atlantic Ocean with the shipping lane from Europe to South America, and 3) the mid-Indian Ocean with the shipping lane from Madagascar to Indonesia.

In short, the statistical analysis, following an either Lagrangian- or Eulerian approach, did not reveal sound evidence of ship-emission influence on the micro- and macrophysical properties of the large-scale cloud fields that were analysed in this study. More specifically, gradients in aerosol optical depth, its fine-mode fraction, and in cloud droplet number concentration are consistent with an, albeit relatively small, Twomey effect due to ship emissions in two out of the three regions (except in the mid-Atlantic, where no discernible effect on aerosol concentrations is found). However, cloud properties that are more relevant to the radiation budget (cloud fraction, cloud liquid water path and cloud top temperature) change across the ship tracks in various ways, which may be better explained by gradients in the large-scale meteorology than by any single concept of secondary aerosol indirect effects. In particular in the Indian Ocean region, which is close to the ITCZ, convective dynamics may have such a large influence on the cloud fields that the signal-to-noise ratio stemming from any microphysical perturbations due to ship emissions is very small. Thus, no effect of the ship emissions on the radiation budget is discernible, and in conclusion, no discernible aerosol indirect effect of ship emissions can be identified. However it must again be stressed that the results found in this study only apply to the regions investigated here. Cloud systems in other regions, *e.g.* regions characterised by persistent stratocumulus fields, are known for their susceptibility with respect to shipping emissions. Furthermore, those regions with the most intense ship traffic, such as the northern Atlantic- or northern Pacific Oceans, were not investigated due to limitations of the available data.

Gradients suggesting ship-emission influence in the retrieved AOD and its' fine mode fraction (FMF) were found for the SE-Pacific and mid-Indian Ocean regions. In these two corridors, the FMF increases from the clean- to the polluted sides of

the shipping corridor which suggests a larger fraction of small particles downwind of the shipping lane. It is also in these two regions where the retrieved cloud properties indicate a possible first AIE: for the shipping corridor in the SE-Pacific Ocean the expected positive correlation of the AOD with CDNC is found. In the mid-Indian Ocean region, a change in the across-corridor gradients of the retrieved cloud properties is obtained near the point of the shipping lane, *e.g.* the systematic decrease in CDNC in the clean side does not continue into the polluted side of the corridor. So from the retrieved cloud droplet number concentration and aerosol parameters, features consistent with a Twomey aerosol indirect effect are found in these two out of three regions. However, the across-corridor gradients of total AOD do not support a possible aerosol direct radiative effect (DRE) in any of the three regions. As model estimates of the aerosol DRE from shipping are small and range from -47.5 to -9.1 mWm^{-2} (Eyring et al., 2010, and references therein), its detection in satellite data for the regions investigated in this study seems highly unlikely.

In the mid-Atlantic Ocean on the other hand, the obtained across-corridor gradients of aerosol properties do not yield such a clear picture. For the Lagrangian approach, the AOD increases from the clean- to the polluted side of the trajectories whereas the opposite is true for the Eulerian analysis. These differences are probably due to differences in the filtering for analysed scenes (see Ch. 2.4.2.2).

To characterise the local meteorology, the SST as retrieved from microwave remote sensing was used and it was found to increase from the clean- to the polluted sides of the corridors for all three corridors. This is of particular interest, because a large number of modelling studies have found a positive correlation between SST and CTH (see *e.g.* Betts and Ridgway (1989)). The retrieved CTHs did not show this relationship with SST in all corridors: in the SE Pacific region, the increase in SST is accompanied by a decrease in CTH, whereas the CTH mostly increased with increasing SST for the other two regions of interest.

In a recent modelling effort, Lauer et al. (2007) estimated that emissions from shipping may lead to a significant negative TOA radiative forcing due to aerosol indirect effects of up to -0.6 Wm^{-2} when implemented into a general circulation model (GCM) with interactive aerosol representation. They show the zonal mean increase in CDNC due to shipping emissions over southern hemisphere tropical oceans to be on the order of $2 - 12$ cm^{-3} which suggests this increase being substantially larger in regions of intense shipping. In the Lagrangian analysis, along-trajectory gradients in CDNC of ≈ 2 cm^{-3} were obtained for both regions. From the Eulerian analysis, constant across-corridor gradients leading to differences in the range $10 - 25$ cm^{-3} are found for the mid-Atlantic and SE-Pacific Ocean regions. Thus, in the mid-Atlantic and SE-Pacific Ocean regions, the analysis does not reveal a change in CDNC as a result from shipping emissions as

suggested by the estimates of Lauer et al. (2007). But in the mid-Indian Ocean, the obtained results are somewhat consistent with the modelling estimates. There, CDNC shows an apparent decrease across the clean part of the shipping corridor. Near the shipping lane, the gradient levels off and CDNC stays constant or even increases throughout the polluted part. If this change in across-corridor gradient is due to shipping emissions and CDNC were to further decrease under undisturbed conditions, the shipping emissions lead to an increase in CDNC by 4 - 6 cm^{-3} in the polluted part. This value would meet the lower end of the estimates in Lauer et al. (2007).

With shipping traffic bound to increase in the next decades, it remains a challenging task to quantify its emissions' effects on the TOA radiation budget from measurements. However, the uncertainties associated with satellite-sensor retrieval algorithms and their inability to deliver sound results for multi-layered cloud systems hampers their usability in regions with the highest shipping emissions, *i.e.* in the northern mid-latitudes. With the technical possibilities available today, the approach taken in this study therefore may represent the best possible one to tackle possible aerosol indirect effects from shipping emissions on large scale environments other than regions governed by stratocumulus clouds.

GLOBAL MODELLING OF SHIP-INDUCED AIES

In this chapter, globally averaged aerosol indirect effects (AIEs), resulting from shipping emissions of aerosols and aerosol precursor gases, are assessed by employing the aerosol climate model ECHAM5-HAM. Emissions of sulphur dioxide (SO₂), black carbon (BC) and particulate organic matter (POM) for the year 2000 are implemented into the model. The model's sensitivity towards uncertainties associated with the shipping emissions themselves is investigated. Sensitivity experiments are designed to investigate (1) the uncertainty in the size distribution of emitted particles, (2) the uncertainty associated with the total amount of emissions, and (3) the impact of reducing carbonaceous emissions from ships.

The results from one experiment are employed for a detailed discussion of shipping-induced changes in the global aerosol system as well as the resulting impact on cloud properties. From all sensitivity experiments, AIEs from shipping emissions are found to be in the range of $-0.07 \pm 0.01 \text{ Wm}^{-2}$ to $-0.32 \pm 0.01 \text{ Wm}^{-2}$. The magnitude depends much more on the assumed emission size distribution than on the magnitude of the emissions themselves – this result should be expected as the amount of emitted particles scales with the inverse of their cubed radius. It is important to note that although the upper estimate of AIEs from shipping emissions is relatively large, it is only about half of the previous upper estimate (Lauer et al., 2007). The reduction of carbonaceous emissions from ships is not found to have an important impact on the globally averaged AIEs as simulated by ECHAM5-HAM.

3.1 The ECHAM5-HAM aerosol climate model

3.1.1 Dynamics

In this study, the ECHAM5-HAM GCM is employed to thoroughly investigate the effect of shipping emissions on clouds. ECHAM5 is the fifth generation climate

model developed at the Max Planck Institute for Meteorology which continuously evolved from the model of the ECMWF (European Centre for Medium-Range Weather Forecasts) (Roeckner et al., 2003). In ECHAM5, prognostic equations for divergence, vorticity, surface pressure, and temperature are solved in terms of spherical harmonics and with triangular truncation. Calculations of parametrised subgrid-scale processes are performed on a corresponding Gaussian grid. In the simulations discussed here, cloud cover is computed following a relative humidity-based approach (Sundqvist et al., 1989) and the treatment of convective clouds and -transport is based on the mass-flux scheme of Tiedtke (1989). Cloud microphysics are computed according to Lohmann et al. (2007) with a detailed description given below. Transport of physical quantities in gridpoint-space, such as water vapour, cloud water and -ice, and trace components is performed via a semi-lagrangian transport scheme (Lin and Rood, 1996). The radiation scheme has four bands in the solar spectral range (one UV/VIS, three in NIR Fouquart and Bonnel, 1980) and 16 bands in the longwave spectral range (Mlawer et al., 1997).

In this study, ECHAM5 is configured to perform nudged simulations, that is, to perform simulations in which the prognostic variables (vorticity, divergence, temperature and surface pressure) are relaxed towards an atmospheric reference state. This relaxation is performed using an implicit Eulerian framework and ERA-Interim reanalysis data (Simmons et al., 2007) is used to define the atmospheric reference state. Although the ERA-Interim re-analysis data are available at just six-hourly resolution, the ECHAM5-HAM simulations are nudged at every model time step (twelve minutes in our case). Therefore, the ERA-Interim input data are spline-interpolated to match the model time step which then results in ECHAM5-HAM's atmospheric state being most closely tied to the re-analysis data every six hours of model time. The nudging routine is applied at all vertical levels of the model and all spectral components, except for the 0th one. Because the nudging is performed for just the four parameters mentioned above, the hydrological cycle remains almost untouched so clouds can develop freely within the imposed dynamics. However, a possible feedback of changes in cloud properties on the general circulation cannot be obtained from this kind of simulation and the energy budget may not be closed on local scales (S. Rast, pers. comm. 2011). However, nudged simulations are the tool of choice in this study because this allows for the derivation of statistically significant results from relatively short simulations (*i.e.* five years in this case). Otherwise, longer simulations would be necessary to eliminate internal variability of the model. For a detailed mathematical description of the nudging procedure, please refer to Appendix A.

3.1.2 Aerosols

For the purposes of this study, ECHAM5 is combined with HAM (Hamburg Aerosol Module), a microphysical aerosol module which predicts the evolution of an aerosol population represented by seven interacting internally and externally mixed log-normal aerosol modes (Stier et al., 2005). Currently, HAM is designed to treat an aerosol population consisting of sulfate (SU), black carbon (BC), particulate organic matter (POM), sea salt (SS) and dust (DU) with the possible mixing state configurations as shown in Tab. 3.1. The modes consist of compounds with either low or no solubility (insoluble modes) or an internal mixture of insoluble and soluble compounds (soluble modes). The microphysical interaction among the modes, such as coagulation, condensation of sulfuric acid on the aerosol surface, and water uptake are calculated by the microphysical core M7 (Vignati et al., 2004). New particle formation is calculated as in the experiments of Kazil et al. (2010) (using ECHAM5-HAM): particle formation via (1) cluster activation and (2) neutral- and charged activation are treated following Kulmala et al. (2006) and Kazil and Lovejoy (2007), respectively. Compared to observations, Kazil et al. (2010) found a generally good agreement of ultrafine-particle numbers in the marine boundary layer, however accompanied by significant overestimation of CDNC over oceans. Furthermore, particle numbers in the mid- to high troposphere were found to be much too high. To overcome this overestimation of ultrafine particle numbers, Kazil et al. (2010) suggest to limit the maximum mean diameter of Nucleation mode particles to 5 nm; a suggestion which is not applied in the scope of this study in order to stay as close as possible to the original formulation of HAM (P. Stier, pers. comm.). Further components of HAM are an emission module (see below for details), a sulfur chemistry scheme (Feichter et al., 1996), a deposition module, and a module to calculate the aerosol radiative properties.

Table 3.1: Modal structure and possible mixing state configurations of HAM; N_i denotes the aerosol number of the mode i and M_i^j denotes the mass of compound $j \in \{\text{SU}, \text{BC}, \text{POM}, \text{SS}, \text{DU}\}$ in mode i . The ranges of \bar{r} give the respective mode boundaries. For the acronyms, “S” and “I” denote soluble and insoluble modes, respectively. (adapted from Stier et al., 2005, 2006a)

Mode	\bar{r} [μm]	Acronym	Soluble/mixed	Insoluble
Nucleation	$\bar{r} \leq 0.005$	NS	N_1, M_1^{SU}	-
Aitken	$0.005 \leq \bar{r} \leq 0.05$	KS, KI	$N_2, M_2^{\text{SU}}, M_2^{\text{BC}}, M_2^{\text{POM}}$	$N_5, M_5^{\text{BC}}, M_5^{\text{POM}}$
Accumulation	$0.05 \leq \bar{r} \leq 0.5$	AS, AI	$N_3, M_3^{\text{SU}}, M_3^{\text{BC}}, M_3^{\text{POM}}, M_3^{\text{SS}}, M_3^{\text{DU}}$	N_6, M_6^{DU}
Coarse	$\bar{r} \geq 0.5$	CS, CI	$N_4, M_4^{\text{SU}}, M_4^{\text{BC}}, M_4^{\text{POM}}, M_4^{\text{SS}}, M_4^{\text{DU}}$	N_7, M_7^{DU}

3.1.3 Clouds

In the simulations discussed here, cloud microphysical properties are derived using a double-moment scheme which solves prognostic equations for cloud water (q_l) and -ice (q_i) mass mixing ratios as well as for the number of cloud droplets (N_l) and -ice crystals (N_i) (Lohmann et al., 2007, and references therein). The parametrised microphysical processes relevant for liquid-water cloud properties are nucleation of cloud droplets, condensational growth of cloud droplets, autoconversion of cloud droplets to form rain water, accretion of cloud droplets by snow and by rain, and melting of cloud ice and snow. The amount of q_l inside a grid box is provided by the condensation scheme (Sundqvist et al., 1989) with an additional source from convective detrainment, and is a prerequisite for performing the calculations of cloud microphysics. Because it is of crucial importance to calculate the evolution of the cloud droplet population correctly, N_l is computed prognostically from (Lohmann et al., 1999):

$$\frac{\partial N_l}{\partial t} = R(N_l) + Q_{\text{nucl}} - Q_{\text{aut}} - Q_{\text{self}} - \frac{N_l}{q_l} (Q_{\text{racl}} + Q_{\text{sacl}} + Q_{\text{frz}} + Q_{\text{evc}}) + Q_{\text{mlt}}. \quad (3.1)$$

In Eq. 3.1, $R(N_l)$ represents the advective, turbulent, and convective transports of N_l , Q_{nucl} is the nucleation of cloud droplets, Q_{aut} is the autoconversion of cloud droplets, Q_{self} is the self-collection of cloud droplets, Q_{racl} and Q_{sacl} are the accretion of cloud droplets by rain and snow, respectively, Q_{frz} is the freezing of cloud droplets, Q_{evc} is the evaporation of cloud droplets and Q_{mlt} is the melting of ice crystals.

Here, the mechanisms representing cloud droplet nucleation and the autoconversion process are explained in detail as these are the most relevant to determining aerosol indirect effects for liquid water clouds. For a detailed description of the other microphysical processes, please refer to Lohmann et al. (1999). The cloud microphysical scheme is coupled to HAM in such a way that changes in both the aerosol- and cloud population can feed-back onto each other (*e.g.* aerosols serve as cloud condensation nuclei (CCN)/precipitation provides a depositional sink for aerosol particles). As described in Lohmann et al. (2007), cloud droplet nucleation Q_{nucl} [$\text{m}^{-3}\text{s}^{-1}$] is parametrised as an empirical function of aerosol number concentrations in the soluble modes except for the smallest (nucleation) mode (KS, AS, CS) according to Lin and Leaitch (1997):

$$Q_{\text{nucl}} = \max \left[\frac{1}{\Delta t} \left(0.1 \left(\frac{N_a w}{w + \alpha N_a} \right)^{1.27} - N_{l,\text{old}} \right), 0 \right] \quad (3.2)$$

with N_a being the number concentration of aerosol particles having a wet radius $> 0.035\mu\text{m}$ [m^{-3}], w is the vertical velocity [ms^{-1}], Δt is the model timestep and

$N_{i,old}$ is the cloud droplet concentration from the previous timestep. The value of $\alpha = 0.023 \text{ cm}^4\text{s}^{-1}$ is obtained from observations (Lin and Leitch, 1997) and accounts for the size-dependent hygroscopicity of aerosol particles. In Eq. 3.2, Q_{nucl} therefore depends on the aerosol size and the dependence on aerosol composition is taken into account by assuming that all aerosols in the soluble modes can serve as cloud condensation nuclei. Dusek et al. (2006) have shown that it is more the aerosol size than the -composition which determines aerosol activation. Furthermore, the cut-off radius of $0.035 \mu\text{m}$ falls in-between the activation-radii observed for maritime- and continental clouds, namely $\approx 0.037 \mu\text{m}$ and $0.033 - 0.042 \mu\text{m}$ at supersaturation $S = 0.4\%$, respectively (Dusek et al., 2006). Here it is important to note that there still exists a considerable uncertainty concerning the actual S in (stratiform) clouds. Most studies find values of $S < 0.3\%$ (e.g. Hegg et al., 2009, and references therein), but evidence suggests that S may also be considerably higher (e.g. Hudson et al., 2010). Regardless of the value of S attained for a grid box in ECHAM5, the aerosols found suitable for cloud droplet nucleation are those attributable to the transition zone from the soluble Aitken- to the Accumulation mode in HAM (KS and AS, see Tab. 3.1). Therefore, any change in the aerosol population, such as from shipping emissions, which has the potential to alter that particular aerosol population can also potentially alter cloud properties in ECHAM5-HAM.

The vertical velocity w as used in Eq. 3.2 is obtained by combining the mean vertical velocity of a model grid box \bar{w} with contributions estimated from the turbulent kinetic energy (TKE, after Brinkop and Roeckner, 1995) and the convective available potential energy (CAPE, Rogers and Yau, 1989):

$$w = \begin{cases} \bar{w} + 1.33\sqrt{\text{TKE}}, & \text{stratiform clouds} \\ \bar{w} + \sqrt{\text{CAPE}} + 1.33\sqrt{\text{TKE}}, & \text{convective clouds.} \end{cases} \quad (3.3)$$

Here it is important to note that convective clouds have no effect on the radiation calculation because they are assigned a cloud cover of zero. In ECHAM5, the convection parametrisation provides for vertical transport and horizontal detrainment of cloud water and CCN, *i.e.* the number of which is calculated by Eq. 3.3. The detrained CCN then serve as potential nuclei for stratiform clouds which form at the detrainment level.

Autoconversion, *i.e.* conversion from cloud droplets to form precipitation, is treated according to the relation found by Khairoutdinov and Kogan (2000) in which the autoconversion rate $Q_{\text{aut}} [\text{s}^{-1}]$ is given by

$$Q_{\text{aut}} = 1350 \times q_l^{2.47} N_l^{-1.79}, \quad (3.4)$$

which represents a least squares fit to results obtained from a droplet spectra

resolving cloud model. In Eq. 3.4, q_l is the cloud liquid water mass mixing ratio and N_l the number of cloud droplets [cm^{-3}]. Thereby, the autoconversion rate negatively correlates with the number of cloud droplets; a response expected from studies advocating for the second aerosol indirect effect (*e.g.* Albrecht, 1989). To then provide the link to atmospheric radiation (see Eq. 1.1), the cloud droplet effective radius r_{eff} is calculated according to

$$r_{\text{eff}} = \epsilon \sqrt[3]{\frac{3\rho q_l}{4\pi b \rho_l N_l}}, \quad (3.5)$$

with (q_l/b) being the cloud liquid water mixing ratio in the cloudy part of the grid box (b is the cloud fraction), N_l is the number of cloud droplets, ρ is the density of air, and ρ_l is the density of water. The ratio ϵ between volume-mean and effective radius (defined as the ratio of the volume-mean to the surface-mean radius) takes into account the dispersion of the droplet size spectrum.

3.1.4 Aerosol emissions

HAM uses prescribed emissions of aerosol species and aerosol precursor gases (carbonaceous- and sulfuric compounds) as well as interactively calculated particle emissions to calculate the global aerosol population. The emissions of dust (Tegen et al., 2002), sea salt (Guelle et al., 2001) and dimethyl sulfide (DMS, Kettle and Andreae, 2000) are computed on-line. The emissions of carbonaceous and sulfuric compounds, except those from shipping, are prescribed according to the AEROCOM recommendations (Dentener et al., 2006).

As this study is focused on quantifying the effect of shipping emissions on clouds, particular focus is put on the emissions which represent the contribution from ships. The AEROCOM-recommended shipping emissions of sulfuric compounds are taken from the EDGAR inventory (Olivier et al., 2005) and carbonaceous emissions represent those as described in Bond et al. (2004). In the EDGAR inventory, sulfuric emissions from ship traffic are represented as emission fluxes along single shipping lanes (*e.g.* in one lane across the northern Atlantic Ocean (see Fig. 3.1)). On the contrary, the carbonaceous compounds are more widely emitted over entire shipping corridors (in accordance with Corbett et al., 1999). Due to this inconsistency, the original It is therefore obvious that this previously used inventory may not be a good approximation for actual shipping emissions. For the purpose of this study, it is therefore substituted by a shipping inventory produced within the European Integrated Project QUANTIFY (EU-IP QUANTIFY) which comprises globally gridded data of shipping emissions for the year 2000 (Behrens, 2006). That inventory offers a consistent geographical distribution for all emitted components and a comparison of the total emissions is given in Tab. 3.2. The spatial distribution of SO_2 -emissions in both the QUANTIFY- and

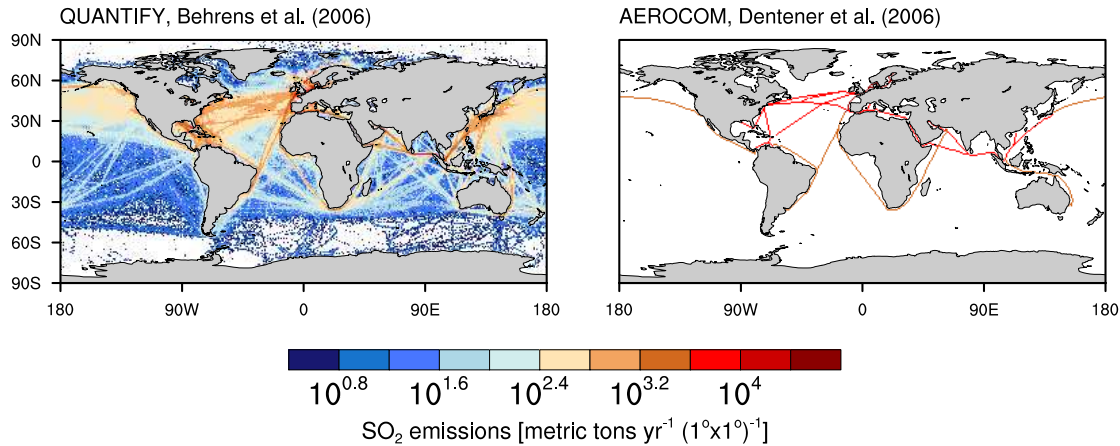


Figure 3.1: Emission fluxes of SO₂ from ships as in the QUANTIFY- and AEROCOM emission inventories for the year 2000 (Behrens, 2006; Dentener et al., 2006).

AEROCOM inventories is shown in Fig. 3.1; the distributions of carbonaceous emissions is similar among both datasets.

Table 3.2: Annual emissions of particulate matter and aerosol precursors in Tg yr⁻¹ for the year 2000. The QUANTIFY inventory is the one employed in this study, while the one by Dentener et al. (2006) is shown for reference purposes.

Compound	QUANTIFY (Behrens, 2006)	AEROCOM (Dentener et al., 2006)
SO ₂	7.95	7.75
BC	0.03	0.13
POM	0.15	0.06

In the QUANTIFY inventory, the geographical distribution of shipping emissions is performed by using a combination of COADS (Comprehensive Atmosphere-Ocean Data Set) and AMVER (Automatic Mutual-Assistance Vessel Rescue System) ship-traffic densities for the years 2000 and 2001/2002, respectively. COADS is maintained by the NOAA (National Ocean and Atmosphere Administration) and is a publicly available dataset of global marine surface observations. These include ship positions and ship identifiers reported by oceangoing vessels on a voluntary basis which can then be used for the estimation and spatial distribution of shipping emissions. AMVER is a ship reporting system on a voluntary basis to ease the rescue of people in distress at sea. This system is generally constrained to ships having a size larger than 1000 gross tonnage (GT), but Endresen et al. (2003) illustrate that the AMVER ship position dataset does a good job representing the global cargo fleet. To distribute the annual emissions in the QUANTIFY inventory, 997168 (COADS) and 993074 (AMVER) marine reports were used as input for deriving global ship reporting frequencies as illustrated in Endresen et al.

(2003). The global distributions are shown in Dalsøren et al. (2009). In a different study, Wang et al. (2007) have combined the AMVER and COADS data to come up with a more representative geographical distribution of shipping emissions. They also report that near-coast shipping is vastly underestimated in both AMVER and COADS and they accordingly derive significantly higher ship traffic in coastal waters than previous studies. Because this study is rather focused towards the effect of shipping emissions on open oceans, the information provided in Wang et al. (2007) is not applied employed here.

In addition to the uncertainties related to the geographical distribution of the shipping emissions, there also exist inherent uncertainties in the total fuel consumption of seagoing ships. For the QUANTIFY inventory, a statistical approach to relate ship size, ship type, and days spent at sea is used to derive the total global annual fuel consumption (Endresen et al., 2003, 2007; Dalsøren et al., 2009) as 172.5 Mt of total fuel consumption for the year 2000. A different approach to estimate the global fuel consumption is taken by Corbett and Koehler (2003) and Eyring et al. (2005b) in which the authors combine total installed engine power and -operation hours with emission factors. By doing this, they come up with a total annual fuel consumption of 289 Mt and 280 Mt, respectively. The large differences between QUANTIFY and the other inventories concerning the fuel consumption estimates have been a matter of intense debate. It has also been shown that the assumed level of activity (or “days at sea”) is the main reason for the large differences (*e.g.*, Endresen et al., 2004; Corbett and Koehler, 2004).

Because the QUANTIFY emission inventory shows a somewhat low estimate of total annual fuel consumption among the current best estimates, the use of this inventory will yield a lower estimate of the effect of shipping emissions on clouds and climate. To quantify the uncertainty associated with total annual fuel consumption, sensitivity experiments in which the emissions are scaled according to higher fuel consumption estimates are also performed.

The emissions are applied as a constant flux (in $[\text{kg m}^{-2} \text{s}^{-1}]$) into the respective model layer. Monthly resolved ship traffic density datasets do exist (*e.g.* Wang et al., 2007) and their main advantage is a better representation of seasonal variations in shipping corridors. This is especially the case in the northern hemisphere because ship traffic tends to avoid the intense regions of the storm-tracks. Nevertheless, the uncertainty introduced by using annually mean emission fields is probably negligible compared to the uncertainty associated with the emissions themselves (A. Lauer, pers. comm., 2011).

3.1.5 Experiments

Quantifying the effect of shipping emissions on clouds is achieved by performing and analysing a total of seven GCM experiments. The experiments are designed

to highlight the uncertainties associated with the total global annual fuel consumption and the emission size distribution as well as to investigate the potential and implications of mitigating carbonaceous-particle emissions from ships. All simulations are performed with a horizontal resolution of T63 ($1.8^\circ \times 1.8^\circ$) and a vertical resolution of 31 levels up to 10 hPa. Monthly mean sea surface temperatures (SSTs) and sea ice cover are prescribed according to the AMIP II dataset (Atmospheric Model Intercomparison Project Taylor et al., 2000). The performed simulations span the time period from October 1999 - December 2004. The first three months are considered as model spin-up and the analysis is then performed on the remaining years. The main characteristics of the experiments are listed in Table 3.3.

Table 3.3: Experimental setup configurations for the GCM runs used in the analysis. The “old” emission parameterisation refers to the operational AEROCOM method whereas the “new” one was developed in this study. The scaling factor is applied to investigate the range of uncertainty associated with unknown total fuel consumption. The acronyms for the emission modes are: KI (Aitken insoluble), KS (Aitken soluble), AS (Accumulation soluble), CS (Coarse soluble).

Experiment	emission parameterisation	scale factor	Particulate emissions, emission mode		
			f_{SO_4} ^a	BC	OC ^b
NS	old	-	-	-	-
A	old	1	2.5% (50% AS, 50% CS)	KI	KI
B	new	1	4.5%, KS	KS	KS
Asc	old	1.63	2.5% (50% AS, 50% CS)	KI	KI
Bsc	new	1.63	4.5%, KS	KS	KS
BnoBC	new	1	4.5%, KS	-	KS
BnoC	new	1	4.5%, KS	-	-

^a mass fraction of emitted sulfur to be emitted as primary SO_4

^b HAM treats OC emissions as emissions of POM. OC emissions are therefore scaled by 1.4 to obtain values of emitted POM

In experiment **A**, the model is run with the QUANTIFY inventory using the originally implemented shipping emissions parameterisation. In doing this, the original emission parameterisation is slightly modified because it was found to be inconsistent – the carbonaceous compounds from shipping emissions were origi-

nally assigned to the model's surface layer whereas the sulfuric compounds were assigned to one layer above the model's surface layer. This is because shipping emissions in AEROCOM are considered as part of industrial emissions, the sulfuric emissions from ships are combined in the same input-dataset as the industrial emissions. For these emissions, an emission height well above the surface is assumed because industrial plants emit most of their exhausts from smoke stacks. This method is not applied to industrial carbonaceous emissions because their fraction in the stack-emissions is assumed to be negligible (S. Kinne, pers. comm. 2010). The emission routine in HAM is therefore modified so that all emissions from ships are consistently assigned to the model layer above the surface layer.

In experiment **A**, the emissions of BC and OC are assigned to the insoluble Aitken mode with a number mean radius of $\bar{r} = 0.03 \mu\text{m}$ and a standard deviation of the log-normal distribution of $\sigma = 1.59$. The bulk of sulfuric emissions is emitted in form of gaseous SO_2 . Fast processing of gaseous SO_2 emissions is accounted for by allowing a certain fraction f_{SO_4} of the emitted sulfuric mass to transform to particulate sulfate at the point of emission instantaneously (*i.e.* within one timestep). In the AEROCOM setup, $f_{\text{SO}_4} = 2.5\%$. Of this particulate sulfate, 50% is assigned to the soluble Accumulation mode (AS, $\bar{r} = 0.075 \mu\text{m}$, $\sigma = 1.59$) and 50% is assigned to the soluble Coarse mode (CS, $\bar{r} = 0.75 \mu\text{m}$, $\sigma = 2$).

Experiment **B** is developed to investigate the uncertainty associated with the insufficient knowledge of the emission size distribution. A close look at the original emission parametrisation as used in **A** yields significant discrepancies to what is currently known about the microphysical- and chemical properties of shipping emissions.

First, recent studies indicate that the f_{SO_4} is often larger than 2.5%. Agrawal et al. (2008) find a value of $f_{\text{SO}_4} = 3.7 - 5\%$ for a fuel sulphur content of 2.05%. Lack et al. (2009) deduce $f_{\text{SO}_4} = 1.4\% \pm 1.1\%$ and $f_{\text{SO}_4} = 3.9\% \pm 2.0\%$ for low ($<0.5\%$) and high ($>0.5\%$) fuel sulphur content, respectively. Therefore, f_{SO_4} is increased from 2.5% to 4.5% in experiment **B**, considering the fact that the globally weighted marine fuel sulphur content is estimated at 2.68% for 2002, with this value most probably being slightly higher for the year 2000 (Endresen et al., 2004). Our chosen value is also supported by the work of Lauer et al. (2007) where the authors use the shipping emission inventory of Eyring et al. (2005b) with $f_{\text{SO}_4} = 4.38\%$.

Second, the assumed emission size distribution of primary sulfate particles may be too large and the sensitivity of the results to this parameter is also assessed. A number of studies have shown that ships emit a suite of particles which are all in the size range $\bar{r} < 0.05 \mu\text{m}$. Specifically, Petzold et al. (2008) investigated the particle size distribution in an aged plume (20 minutes old, which is roughly on the order of the model timestep) of shipping emissions over the English Channel and found that the modal radius of the ship-emitted particles was $\approx 0.02\text{-}0.04 \mu\text{m}$. Because

this size range corresponds to that of the Aitken mode in HAM, all ship-emitted primary sulfate particles are assigned to the soluble Aitken mode in experiment **B**.

Third, the original parametrisation of shipping emissions assumes all carbonaceous particles being emitted are insoluble. This assumption however is inconsistent with recent laboratory measurements. Kireeva et al. (2010) showed that freshly emitted soot from a ship engine burning fuel with a sulfur content of just 0.5% yields significantly higher solubility than soot emitted from an aircraft- or truck engine. As the globally averaged sulfur content of marine fuel is $>2.5\%$ (*e.g.* Endresen et al., 2004), the differences presented in the work of Kireeva et al. (2010) may even represent a lower estimate. Motivated by these results, all ship-emitted carbonaceous particles are assigned to the soluble Aitken mode in experiment **B**. In their modelling study, Lauer et al. (2007) also assigned all ship-emitted particles to the soluble Aitken mode. Therefore, the model setup for experiment **B** also yields a better comparison framework to earlier studies.

In the experiments **Asc** and **Bsc**, the emissions of the QUANTIFY inventory are scaled in order to investigate the uncertainty associated with the unknown total annual fuel consumption from ships. As previously noted, the QUANTIFY inventory represents a lower estimate among the currently used shipping emission inventories. Therefore, the mass of annually emitted particulate- and gaseous species is scaled to values which meet the ones published by Corbett and Koehler (2003), the inventory which represents the current upper estimate in total annual fuel consumption. In Corbett and Koehler (2003), the annual total emission of SO_2 is given as 12.98 Tg (based on ship activity for the year 2001). Relating this to the given value in the QUANTIFY inventory (7.95 Tg; year 2000), the emissions of SO_2 , BC and OC are scaled by a factor of 1.63 for use in the experiments **Asc** and **Bsc**. This approach implies the assumption of constant emission factors for BC and OC with an increase in SO_2 emissions. Possible changes in the mean emission factors with increasing total emissions (*e.g.* increases in emissions from just a few specific ship-types), are thus not accounted for. Scaling is performed with the emitted mass of SO_2 instead of total annual fuel consumption, because the emitted mass is of more importance for this study than consumed fuel. Still, if the emissions were scaled by total annual fuel consumption instead of emitted SO_2 , the scaling factor would be approximately the same (≈ 1.67).

In the experiments **BnoBC** and **BnoC**, the potential effects of mitigating the emission of carbonaceous compounds from ships are explored. In the recent climate-change discussion, the mitigation of carbonaceous emissions has attracted substantial attention in the scientific community. BC aerosols are associated with a net positive radiative forcing at the top-of-atmosphere (TOA) due to their strong absorption of incident solar radiation and this effect is estimated to contribute

+0.2±0.15 Wm⁻² to anthropogenic radiative forcing of climate (Forster et al., 2007, excluding the semi-direct effect and the impact of BC on snow- and ice surface albedo). Thus, BC is perhaps the third largest individual warming agent, following CO₂ and methane, and reducing its emission could contribute to reducing global warming due to anthropogenic climate change (Jacobson, 2002; Bond and Sun, 2005; Bond, 2007). However, this neglects the ability of BC particles to act as cloud condensation nuclei (CCNs) when they get internally mixed with hygroscopic species through microphysical and chemical ageing. This possibly leads to an overestimation of the cooling potential of BC mitigation options (*e.g.* Pierce et al., 2007; Chen et al., 2010). The direct radiative forcing of OC at TOA is currently estimated as 0.05±0.05 Wm⁻² (Forster et al., 2007).

For both experiments **BnoBC** and **BnoC**, the model with the newly introduced emission parametrisation is employed (see experiment **B**) because it probably represents the actual shipping emissions more closely, and because the expected simulated effects are larger. All BC and all carbonaceous emissions from ships are omitted in experiments **BnoBC** and **BnoC**. These simulations thus represent idealised sensitivity studies because no potential side-effects that BC mitigation may have on the magnitude of sulfuric emissions is included.

3.2 Ship-emission induced processes in ECHAM5-HAM

To illustrate the pathway from shipping emissions to changes in the TOA radiation budget as modelled by ECHAM5-HAM, a stepwise analysis using the results obtained from experiment **B** is performed. The steps in this analysis consider the changes in

- emissions
- aerosol mass- and number burdens
- CCN concentrations
- cloud macro- and microphysical properties
- radiation budget.

In the following, the displayed figures represent simulated five-year mean values. Statistical significance is computed by applying a Student's t-test to the respective five annually averaged fields and the standard deviation of the five annual means in each grid-box.

3.2.1 Changes in emissions and mass burdens

The global distributions of total sulphur (comprised of sulphur dioxide (SO₂), sulfate and dimethyl sulphide (DMS)), black carbon (BC) and particulate organic matter (POM) emissions along with their associated anthropogenic fractions are shown in Fig. 3.2. Shipping emissions represent just a small fraction of the global mean anthropogenic emissions: 7.2% for S, 0.5% of BC and 0.25% of POM. However, emissions from shipping often occur in otherwise pristine marine environments and can therefore result in substantial modifications of the aerosol populations in the marine boundary layer (MBL).

These emissions lead to distinct changes in atmospheric column burdens of the emitted constituents. As shown in Fig. 3.3, the relative changes in SO₂ column burden are very similar to the spatial pattern of shipping emissions on global oceans. The largest changes are obtained over the Northern Hemisphere (NH) Atlantic Ocean, the northern Indian Ocean and the northern Pacific Ocean, with most changes being statistically significant at the 10% level. Less significant changes are obtained for the sulfate column burden off the western coasts of Europe and North America as well as in the region of the Malakka strait. It is interesting to note that the obtained relative changes in sulfate column burden show smaller values in Southeast Asia compared to the ones off the western European coast although the changes in SO₂ column burden are of similar magnitudes. Because SO₂ is oxidised to H₂SO₄ by OH, the differences in the obtained changes of sulfate burden can be explained by differences in the OH abundance.

In ECHAM5-HAM, the OH distribution is prescribed using three-dimensional monthly averaged fields obtained from the simulations of Horowitz et al. (2003). The primary source of OH is the photolysis of ozone and subsequent reaction with water vapour. High ozone abundance is found in regions of high photochemical production rates of ozone, which require high concentrations of NO_x and other precursors, as well as ultraviolet radiation. Therefore, the highest ozone concentrations at the surface are obtained for northern mid-latitudes in summer. Generally, ozone concentrations in the middle-troposphere are higher in the NH compared to the Southern Hemisphere (SH) (Horowitz et al., 2003). Accordingly, the OH fields used in ECHAM5-HAM show higher concentrations in the lower to middle troposphere off the western European coasts compared to Southeast Asian waters.

As may be deduced from the relatively small contribution of carbonaceous emissions from shipping to the total emissions, the relative changes in atmospheric BC- and OC burdens only show distinct patterns over the northwestern Atlantic. Also, none of these features is statistically significant. From this, it seems plausible that it is the emissions of sulfuric constituents from ships which ultimately determines the total effect on both cloudy- and clear sky radiative properties.

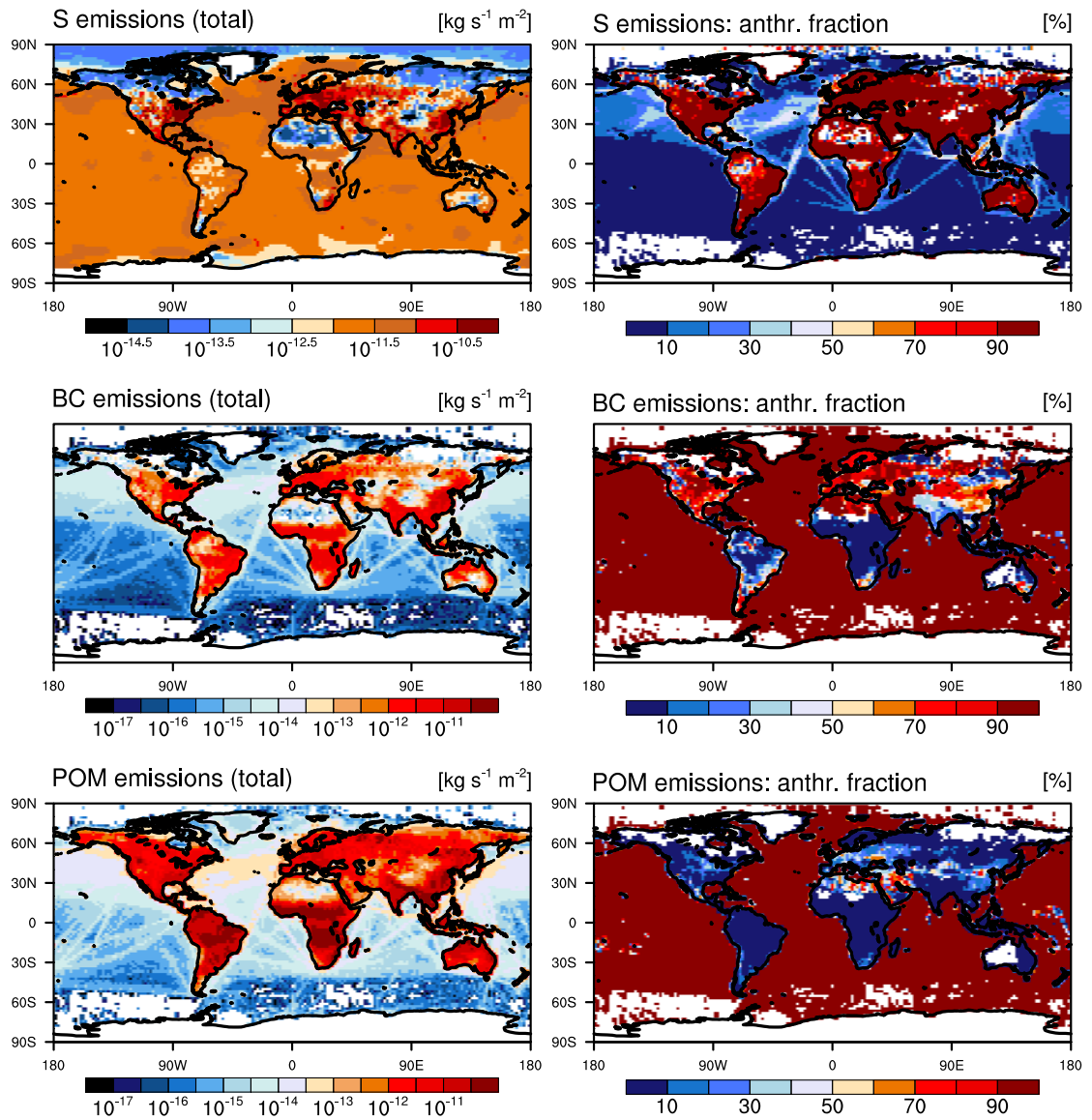


Figure 3.2: Total emissions (left column) and corresponding anthropogenic fractions (right column) of aerosols and aerosol precursors as used in experiment setup **B**. **1st row:** sulphur (comprised of sulphur dioxide (SO_2), sulfate and DMS), **2nd row:** black carbon (BC), **3rd row:** particulate organic matter (POM). The colour scales for the left column denote the \log_{10} of emission fluxes in $[\text{kg s}^{-1} \text{m}^{-2}]$. Anthropogenic fractions are given in [%]. Emissions over land correspond to those prescribed in AEROCOM (Dentener et al., 2006), anthropogenic emissions over water surfaces to those provided in the QUANTIFY shipping emission inventory (Behrens, 2006).

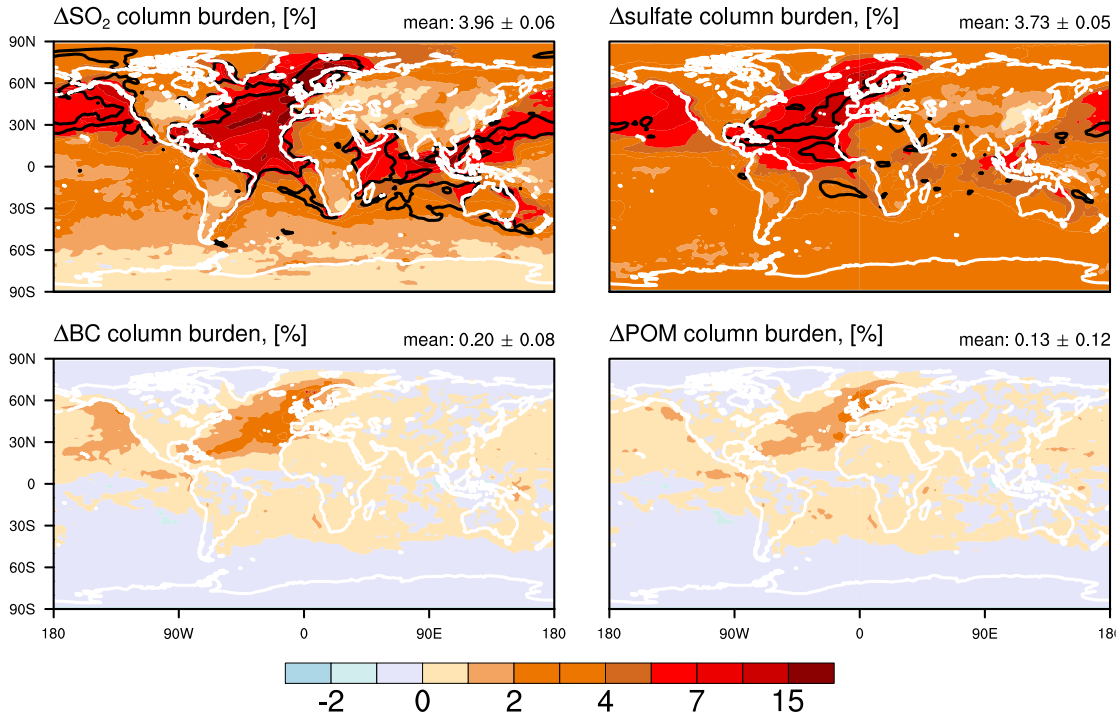


Figure 3.3: Relative changes in [%] of column burden of sulphur dioxide (SO_2 , top left), sulfate (top right), black carbon (BC, bottom left) and particulate organic matter (POM, bottom right) in experiment **B** compared to experiment **NS** (derived from $(\frac{\text{B}-\text{NS}}{\text{NS}} \cdot 100)$). The black contour lines enclose areas showing statistical significance at the 10% level.

3.2.2 Changes in aerosol number burdens

It is feasible to track the models' response induced by a certain change in emission parameters through each aerosol mode, thereby clarifying the underlying processes leading to the observed total response. The analysis starts with the smallest (Nucleation-) mode and subsequently discuss the changes in each larger mode. Global distributions of relative changes in atmospheric column number burdens as well as the vertically- and meridionally resolved changes in particle number concentrations are shown in Figs. 3.4 and 3.5. The population of soluble Nucleation mode (NS) particles by design consists only of secondary aerosol resulting from new particle formation, mainly nucleated from sulfuric acid (H_2SO_4). H_2SO_4 exhibits very low vapour pressure under normal atmospheric conditions, and therefore easily nucleates with water at low ambient temperatures (Kazil et al., 2010, and references therein), such as in the upper troposphere. The largest relative changes in NS-particle number burdens are found in the western part of the northern Atlantic and the northern Indian Oceans. Vertically resolved, the pronounced relative increases in NS-particle concentrations are constrained to the NH mid- and upper troposphere as well as the tropical boundary layer. This feature should be interpreted with care though, as ECHAM5-HAM has been shown to overestimate ultrafine

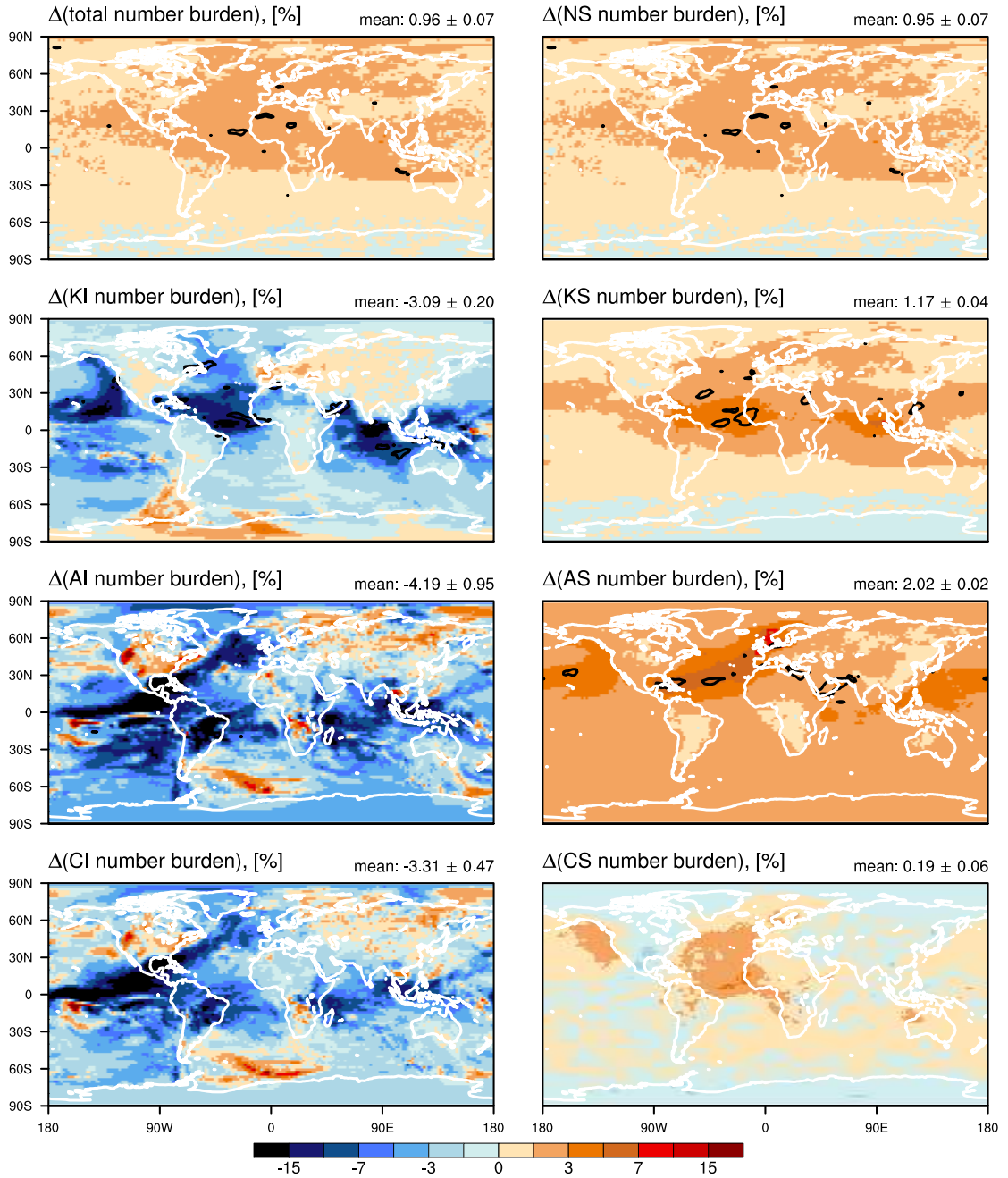


Figure 3.4: Relative changes in [%] of particle number column burdens in experiment **B** compared to experiment **NS** (derived from $(\frac{B-NS}{NS} \cdot 100)$). The change in total particle numbers (top left) as well as the change of particle numbers in each aerosol mode, as resolved by ECHAM5-HAM, is shown. The acronyms in the plot captions follow the notation as introduced in Tab. 3.1. The black contour lines enclose areas showing statistical significance at the 10% level.

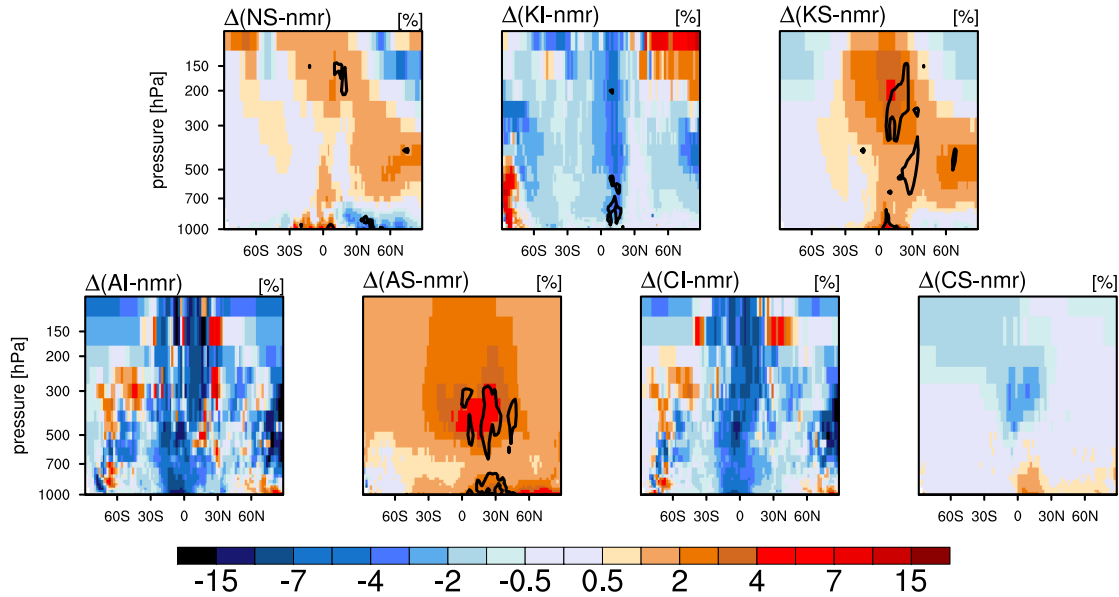


Figure 3.5: Relative changes in [%] of particle number mixing ratios (nmr) in experiment **B** compared to experiment **NS** (derived from $(\frac{B}{NS} - 1) \cdot 100$). The change of particle numbers in each aerosol mode, as resolved by ECHAM5-HAM, is shown. The acronyms in the plot captions follow the notation as introduced in Tab. 3.1. The black contour lines enclose areas showing statistical significance at the 10% level.

particle numbers (Kazil et al., 2010). This increase in NS-particle number concentrations is accompanied by a decrease in particle numbers in the NH mid-latitude boundary layer and low troposphere (up to ≈ 800 hPa), although hardly statistically significant. This is because the number of emitted primary soluble particles in the boundary layer is substantially higher in experiment **B** compared to **NS**. So in **B**, condensation of H_2SO_4 onto pre-existing particles dominates over new particle formation. Furthermore, the large number of primary particles also serves as an efficient coagulation sink for nucleated particles. Although it would be expected that this change is mostly limited to oceanic areas (*i.e.* the place where shipping emissions occur) the same pattern is found for both land and oceanic regions in the temporal average.

For the Aitken mode, particle numbers of the insoluble part (KI) are reduced over almost all oceanic areas except over coastal waters of southwestern Europe and near the southern tip of South America. This reduction is due to an increased number of insoluble particles becoming soluble through either (1) condensation of soluble material on them or (2) coagulation scavenging. The changes in the soluble Aitken mode (KS) roughly correspond to those of **NS**. The decrease of KS particle number concentrations in the NH boundary layer would intuitively not be expected. This unexpected result is similar for **NS**, with a similar pattern for both land- and ocean regions. As outlined for the changes in the NS-particle number concentrations, the increase of emitted primary KS-particles leads to increased

condensation of H_2SO_4 onto them, thus yielding faster (than without shipping emissions) growth rates. The particles then quickly gain size and eventually become large enough to be assigned to the soluble Accumulation mode (AS). For the mid- and upper troposphere, the changes in KS-particle number concentrations result from different processes. The increase in KS-particle number concentrations results from coagulation and condensational growth of increasingly present NS-particles (see above).

The global pattern of relative changes in the column number burden of insoluble Accumulation mode (AI) particles, which are only comprised of dust particles, appear very noisy. Distinct decreases, most probably due to condensation of H_2SO_4 onto the AI-particles, are obtained for the eastern Pacific Ocean, continental South America, the tropical and northern Atlantic Ocean, the western Indian Ocean, and Southeast Asia. With the exception of continental South America and the tropical Atlantic Ocean, these regions are already associated with low AI-particle numbers, so a small decrease in absolute numbers results in large relative changes. Additionally, the tropical Atlantic Ocean as well as continental South America are affected by dust transport from Northern Africa. The increased availability of condensable material, especially over the Atlantic Ocean, therefore leads to substantially more of AI-particles being coated in that region. The marked increase in AI-particle numbers over North America and the southern Ocean east of South America is not clear.

For the soluble fraction of the Accumulation mode (AS), particle number burdens increase everywhere on the globe. In relative numbers, the patterns resemble the areas of highest shipping emissions of the North Atlantic, North Pacific, mid-Indian Ocean, and Southeast Asia. The vertically and meridionally resolved changes in AS-particle number concentrations show an increase practically everywhere throughout the troposphere. Specifically, increases on the order of 10% are obtained for the NH boundary layer and the tropical mid-troposphere. Therefore, the previously described reduction of both NS- and KS-particle number concentrations in the NH boundary layer leads to a significant increase (“accumulation”) of particles in AS. This is of particular interest as the Accumulation mode size range is the one most suitable for CCN-activation at supersaturations typical for stratocumulus clouds (80 - 100 nm at 0.2% supersaturation, *e.g.* Pierce and Adams, 2009).

The relative changes in particle numbers of the insoluble Coarse mode (CI) are very similar to those obtained for AI. This directly results from the fact that particles in both of these modes are comprised of just dust. Therefore, the mechanisms described for the changes in AI-particle numbers also apply to the changes in CI. Correspondingly, soluble Coarse mode (CS) particle numbers distinctly increase off the western coast of northern Africa due to the coating of pre-existing

insoluble dust aerosol with H_2SO_4 . Also, an increase in CS-particle numbers is also obtained for the entire North Atlantic and the eastern North Pacific Oceans. This seems due to fast growing particles which do not get activated to form cloud droplets. Vertically, the increase in CS-particle concentrations is confined to the lower troposphere, but is not as large as for the Accumulation mode. However, the relative changes of particle numbers in the Coarse mode are not significant at the 10% level at any point in the troposphere.

To summarise, the introduction of shipping emissions according to the emission parameterisation applied here leads to substantially increased condensational growth rates of primary Aitken-mode sized particles in the NH boundary layer. This results in decreases in particle number concentrations in both NS and KS and a subsequent increase in particle number concentrations in AS-particle number concentrations in the NH boundary layer. There, the increase in particle number concentrations has the most potential to alter cloud micro- and macro-physical properties by the processes incorporated in the model. Furthermore, the increased availability of sulfuric compounds leads to increased particle nucleation rates throughout the tropical troposphere, which results in increased particle number concentrations in all soluble modes but the Coarse mode. Overall, aerosol particle number concentrations are distinctly increased throughout the troposphere.

The aforementioned faster growth rates of aerosol particles could in fact lead to a reduction of atmospheric lifetimes of those particles. Computed values of the aerosol lifetimes, defined here as the ratio of burdens over sources, are displayed in Tab. 3.4. Indeed, lifetimes are slightly reduced for all aerosol types in experiment **B**, with the exception of sea salt.

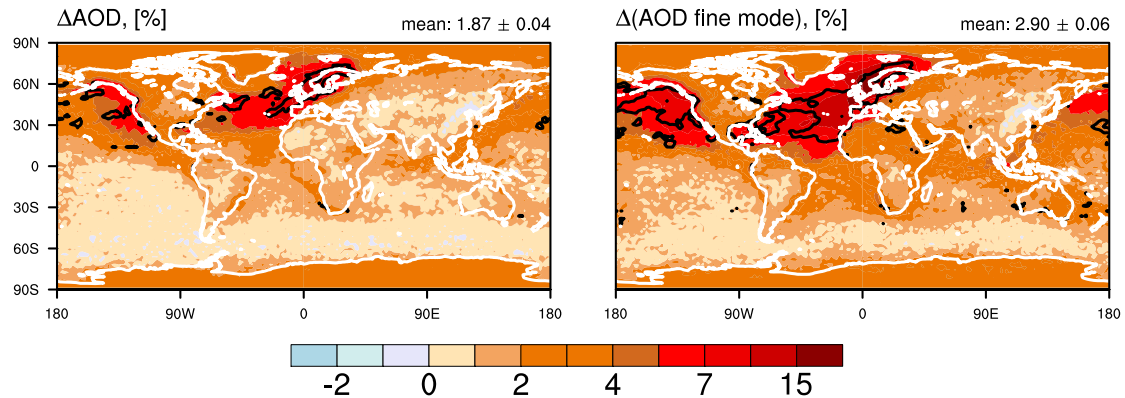


Figure 3.6: Relative changes in [%] of aerosol optical depth (AOD, left) and its fine mode (right) in experiment **B** compared to experiment **NS** (derived from $(\frac{\text{B}-\text{NS}}{\text{NS}} \cdot 100)$). The black contour lines enclose areas showing statistical significance at the 10% level.

The impact of the shipping emissions on the aerosol population and its direct effect on atmospheric radiation is illustrated by the relative changes in AOD and its fine mode (*i.e.* the contribution from particles smaller than $1 \mu\text{m}$ in diameter),

as shown in Fig. 3.6. Statistically significant increases in both the AOD and its fine mode are obtained for most of the western European coastal waters as well as some areas off the western coast of North America. The globally averaged relative increase in the fine-mode AOD is larger than that obtained for the total AOD. This should be expected, as the main increase in particle numbers is found for Accumulation mode sized particles, which are by definition smaller than $1 \mu\text{m}$ in diameter. The impact of this change in AOD on clear-sky atmospheric radiation will be discussed in Ch. 3.2.5.

3.2.3 Changes in predicted CCN concentrations

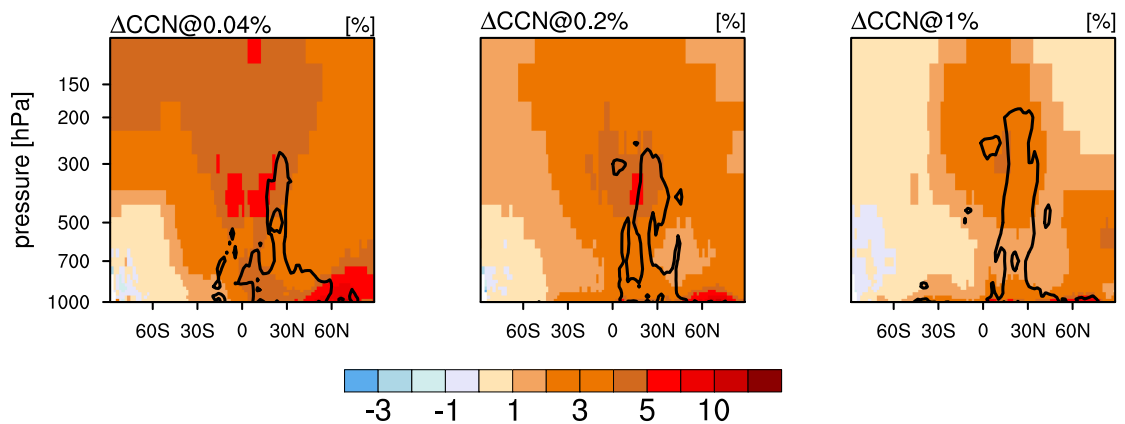


Figure 3.7: Relative changes in [%] of the vertically- and meridionally resolved cloud condensation nuclei (CCN) concentrations at supersaturations $S = 0.04\%$ (left), $S = 0.02\%$ (middle) and $S = 1\%$ (right) in experiment **B** compared to experiment **NS** (derived from $(\frac{\mathbf{B}-\mathbf{NS}}{\mathbf{NS}} \cdot 100)$). The black contour lines enclose areas showing statistical significance at the 10% level.

A recently implemented diagnostic in ECHAM5-HAM allows for the investigation of cloud condensation nuclei (CCN) concentrations at various supersaturations (following Pruppacher and Klett, 1997; Abdul-Razzak et al., 1998; Abdul-Razzak and Ghan, 2000). Vertically- and meridionally resolved changes in CCN concentrations at various supersaturations are displayed in Fig. 3.7. At low supersaturations (0.04%), large areas in the NH lower- to mid troposphere exhibit a significant increase in CCN concentrations, with the values $>10\%$ occurring in the boundary layer north of 60°N . The same holds for the CCN concentration changes at 0.2% and 1% supersaturation. Vertically resolved, the extent of such large relative changes decreases with increasing supersaturation. This again hints at aerosol processing in the boundary layer – smaller particles (higher supersaturations) are found near the emission sources whereas larger particles (smaller supersaturations) are found higher up in the troposphere as a result of microphysical- and chemical ageing during transport. In addition to the increases in CCN concentrations in the NH boundary layer, distinct and often statistically significant increases in CCNs

in the mid to high tropical troposphere are also obtained. This feature is explained by the increases in particle number concentrations for this part of the troposphere where cloud formation is primarily related to detrainment of cloud water resulting from deep convection. Therefore, the increase in CCNs in this part of the atmosphere may lead to highly complex effects, such as the aerosol-influence on mixed phase- and ice-clouds; a topic which has attained a large amount of attention in recent years (*e.g.* Lohmann and Feichter, 2005; Storelvmo et al., 2008a,b; Hoose et al., 2008).

From the evaluation of the changes in CCN concentrations, it is evident that shipping emissions indeed lead to an increased number of CCNs at supersaturations typical for marine liquid water clouds. This follows from distinct increases in soluble Accumulation mode particle numbers, especially in the NH boundary layer, as a result from increased particle growth rates.

3.2.4 Changes in cloud micro- and macrophysical properties

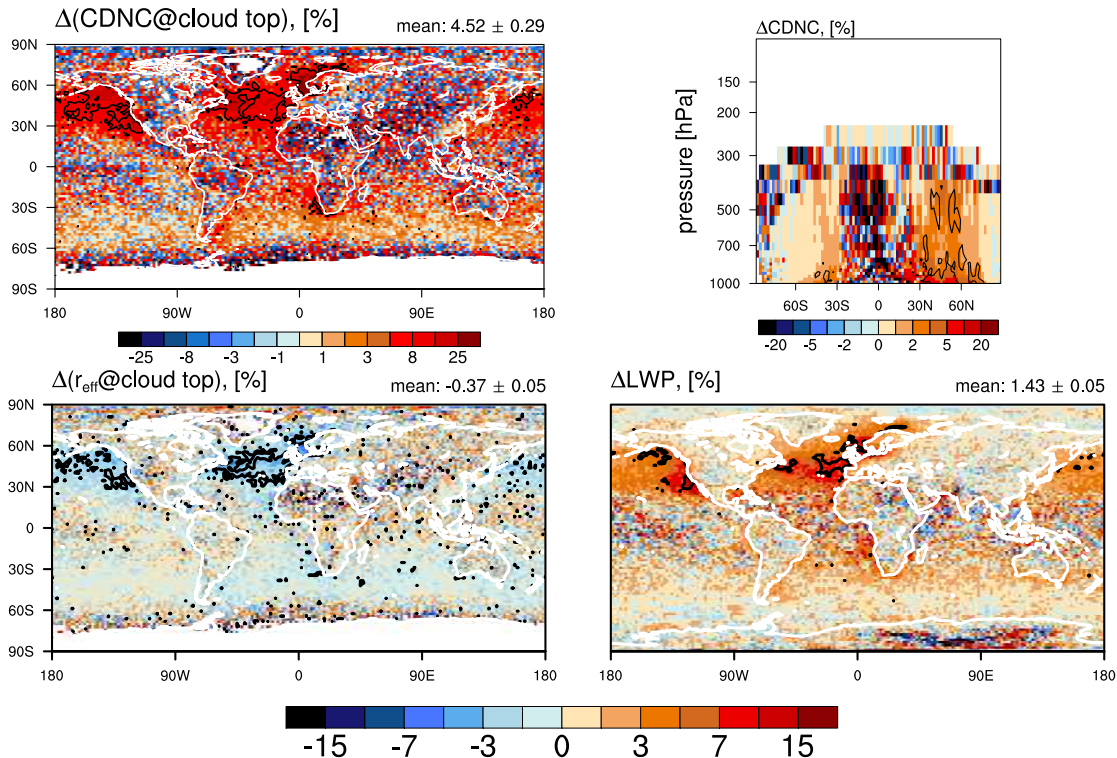


Figure 3.8: Relative changes in [%] of micro- and macrophysical cloud properties in experiment **B** compared to experiment **NS** (derived from $(\frac{\mathbf{B}-\mathbf{NS}}{\mathbf{NS}} \cdot 100)$): cloud droplet number concentration (CDNC) at cloud top (top left), CDNC concentrations (top right), cloud droplet effective radius (r_{eff}) at cloud top (bottom left) and cloud liquid water path (LWP) (bottom right). The black contour lines enclose areas showing statistical significance at the 10% level.

As described in Ch. 3.1.3, the obtained changes in the aerosol population in

experiment **B** with respect to **NS** have the potential to alter liquid-cloud properties. The evaluation of Eqs. 3.1, 3.2 and 3.4 reveals that it is the increase of particle numbers in the soluble Accumulation (AS) mode in the NH which leads to distinct changes in liquid-cloud micro- and macrophysical properties – more droplets are nucleated, which leads to an increase in cloud droplet number concentration (N_l or CDNC) and a decrease of the autoconversion rate. Changes in CDNC are shown in Fig. 3.8. Distinct and sometimes significant increases of CDNC are obtained throughout the North Atlantic- and North Pacific Oceans as well as off the southwestern coast of Africa. Close to the coasts of northwestern Europe and California, CDNCs are increased by more than 15%. The changes over tropical oceans are rather noisy because here, the relatively large variations in macrophysical cloud properties, such as cloud liquid water path/-geometrical thickness, dominate the signal even for the five year averages considered here. This also becomes clear when considering the updraft velocity w given in Eq. 3.3: the contribution of $\sqrt{\text{CAPE}}$ may be small or large depending on the situation whereas the contribution from $\sqrt{\text{TKE}}$ is most probably more homogeneous (spatially as well as temporally). No change in CDNC at cloud top is obtained for the southern oceans stormtracks. Vertically resolved, distinct changes in CDNC are found throughout the mid-latitude NH troposphere up to ≈ 400 hPa. These are significant for most of the boundary layer and for some parts of the mid-troposphere. The corresponding patterns for the change in cloud droplet effective radius (r_{eff}) at cloud top match those of the changes in CDNC – r_{eff} decreases, often statistically significant, throughout the mid-latitude Pacific and Atlantic Oceans as well as off the western coast of southern Africa.

Via the parametrisation of the autoconversion (*i.e.* the conversion of cloud- to precipitation water after Khairoutdinov and Kogan (2000)), a response of cloud macrophysical properties to changes in CDNC is incorporated in the model: the obtained increase in (smaller) cloud droplets leads to a reduced precipitation efficiency which may subsequently lead to an increase in cloud liquid water path (LWP) and possibly cloud fraction (“lifetime effect” Albrecht, 1989). Indeed, the LWP increases over large regions covering both the mid-latitude Atlantic- and Pacific Oceans as well as the stratocumulus region off the southern African west coast. Changes in the cloud cover are also obtained. Zonally averaged, the cloud cover is slightly enhanced in the NH mid-latitude boundary layer (not shown).

3.2.5 Impact on atmospheric radiation

In the scope of this study, the AIE at TOA is defined in terms of the the “radiative flux perturbation” as per the definition given in Lohmann et al. (2010). For this, the instantaneous radiation perturbation by the total aerosol loading, with cloud fields held constant (direct aerosol radiative perturbation, DARP), obtained

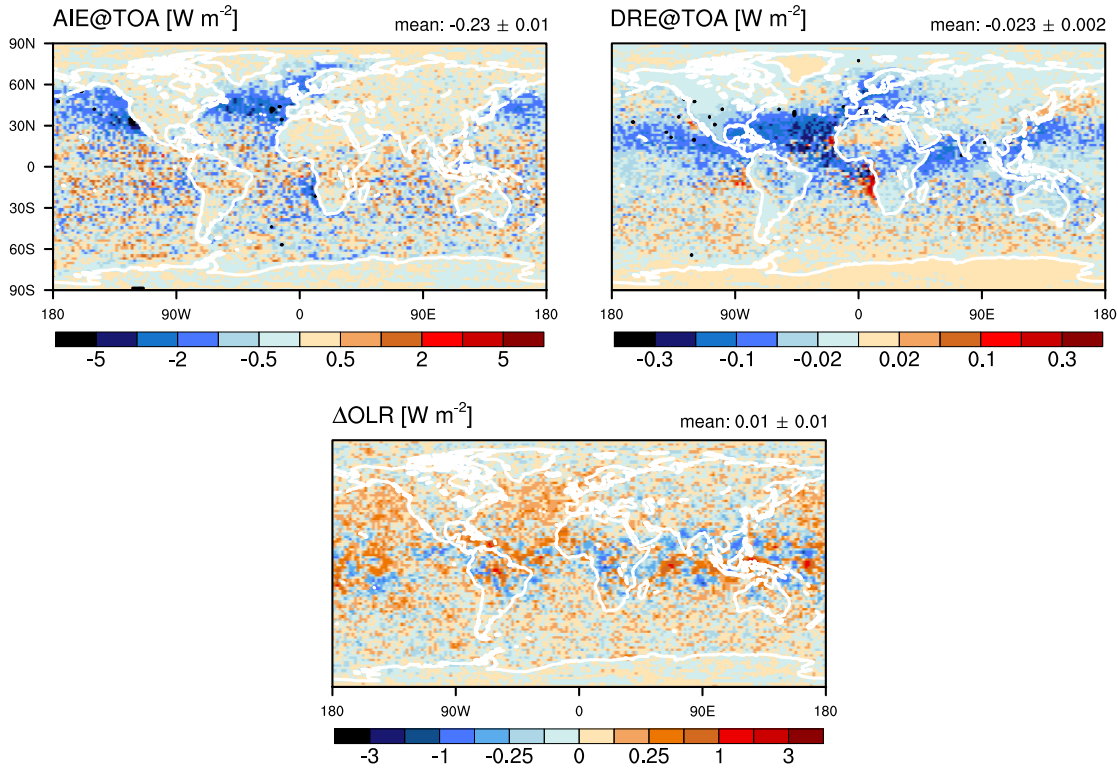


Figure 3.9: Changes in top-of-atmosphere (TOA) radiation in experiment **B** with respect to experiment **NS**. The aerosol indirect effect (AIE, top left) is computed as the change in “net all-sky radiation - direct aerosol radiative perturbation”, the direct radiative effect (DRE, top right) is the change in net clear-sky radiation and the change in outgoing longwave radiation (OLR, bottom) represents changes in net all-sky thermal radiation. The black contour lines enclose areas showing statistical significance at the 10% level.

from a double-call of the ECHAM5 radiation scheme, is subtracted from the net all-sky radiation at the top of the atmosphere (TOA). From the results shown in the previous section, it is evident that the changes in cloud micro- and macrophysical properties induced by the shipping emissions have an effect on atmospheric radiation. As shown in Eq. 1.1, the results should yield a negative AIE at TOA due to the increase in cloud albedo. This is especially true for the North Atlantic and North Pacific as well as off the coast of southern Africa.

Thus using the above-mentioned definition of the AIE, the results from experiment **B** yield an AIE at TOA of $-0.22 \pm 0.008 \text{ Wm}^{-2}$ (see Fig. 3.9). As expected, the largest contributions come from those areas in which the change in shipping emissions leads to the largest changes in cloud micro- and macrophysical quantities: the NH mid-latitude Atlantic Ocean, the Pacific Ocean in close proximity to the Californian coast and the southeastern Atlantic Ocean off the African coast.

The direct radiative effect (DRE) of shipping emissions at TOA, obtained from the difference in the results of the above-mentioned double-call of the ECHAM5 radiation scheme between experiments **B** and **NS**, is found to be -0.02 ± 0.002

Wm^{-2} . Interestingly, the DRE is distinctly positive in some parts of the semi-permanent stratocumulus fields off continental west coasts, such as off the coast of Namibia and Angola. This effect is often observed in that region and is due to absorbing aerosols residing above clouds (*e.g.* Peters et al., 2011, and references therein). The reasons for obtaining this change in **B** could be twofold. Either (1), carbonaceous aerosol from shipping emissions is lofted above the clouds or (2) the absorption of carbonaceous biomass burning aerosol from Africa above the clouds is increased due to increased internal mixing in the presence of shipping emissions. To investigate this, the results from **B** are compared to those of **BnoC** and **BnoBC** and found that the positive DRE off the coast of Namibia and Angola can be attributed to increased internal mixing of biomass burning aerosol (see also Stier et al., 2006b).

Compared to previous estimates of the DRE from shipping emissions (-47.5 to -9.1 mWm^{-2} , Eyring et al., 2010, and references therein), the value obtained from **B** is of comparable magnitude. In previous studies (*e.g.* Lauer et al., 2007), it is argued that the DRE of shipping emissions is negligible compared to the corresponding AIE. However, here it is evident that the emission of non-absorbing aerosols and aerosol precursors from shipping emissions have important implications for the absorption characteristics of pre-existing aerosol. This may then have implications for the macrophysical characteristics of stratocumulus fields, (*e.g.* cloud thickening from Wilcox (2010)).

Both the AIE and DRE are representative of radiative effects in the solar shortwave spectrum. It has been suggested that the aerosol influence on clouds, specifically those stemming from shipping emissions, have the potential to also alter the radiative balance at TOA in the longwave spectral range. Recently, Christensen and Stephens (2011) have shown that under certain meteorological conditions, shipping emissions lead to an increase in cloud top height of liquid water clouds, thereby decreasing cloud top temperature and the emitted thermal radiation. For aerosols other than those stemming from shipping emissions, an increase in cloud top height, as a result of aerosol pollution, has also been found for mixed-phase clouds (*e.g.* Koren et al., 2005; Devasthale et al., 2005). In the results of experiment **B**, no significant changes in the outgoing longwave radiation (OLR) compared to experiment **NS** are found. However, there does seem to be a tendency towards an increase in OLR over NH mid-latitude oceans.

3.3 Sensitivity to emission parameters

In the preceding section, the aerosol- and cloud processes associated with the incorporation of shipping emissions in the aerosol climate model ECHAM5-HAM were investigated. The simulation we used for that detailed analysis however

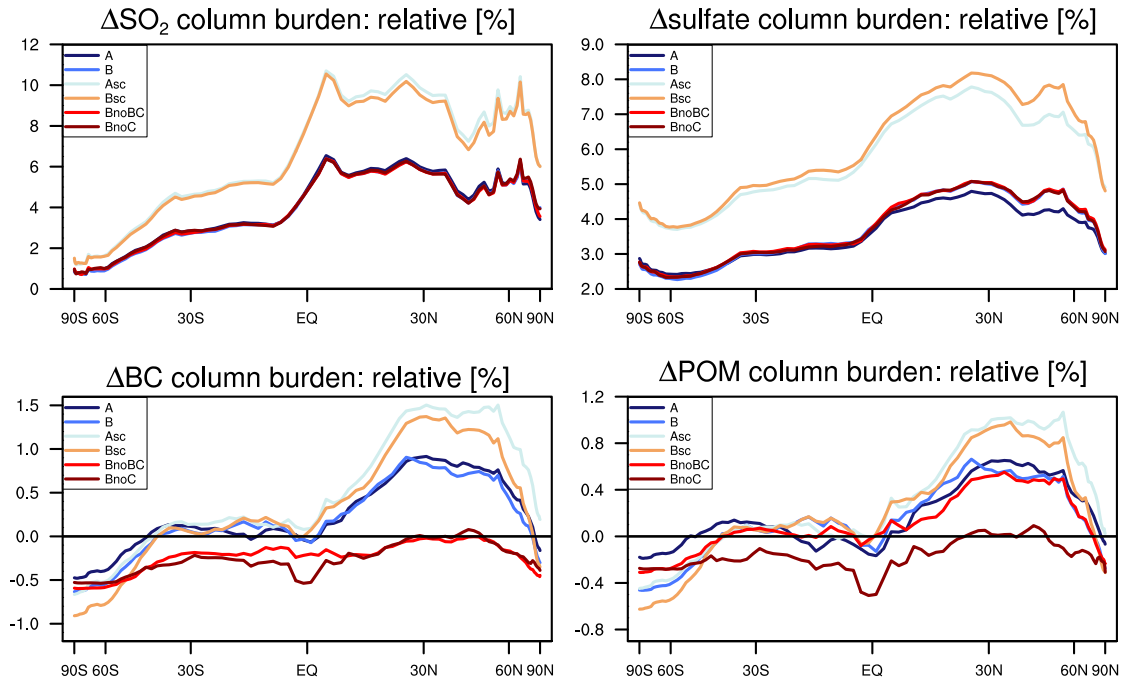


Figure 3.10: Zonally averaged relative changes of atmospheric column burdens with respect to **NS** (derived from $\left(\frac{\text{“experiment”} - \text{NS}}{\text{NS}} \cdot 100\right)$): sulphur dioxide (SO_2 , top left), sulfate (top right), black carbon (BC, bottom left) and particulate organic matter (POM, bottom right).

represents just one possible solution out of those spanning the uncertainty range of the emissions only. To test the models’ sensitivity towards assumed emission parameters, such as the physical- and chemical properties of the emitted particles as well as the total emission amount, in total seven simulations were performed as described in Ch. 3.1.5. This chapter contains a description of the models’ response to changes in (1) the emission parametrisation, (2) the total amount of emissions and (3) the emitted amount of carbonaceous compounds from shipping emissions is described. The results are shown in Figs. 3.10, 3.12, 3.13 and 3.14 as zonal averages over both land and ocean areas. No pre-filtering is applied to the data, such that all available data is used regardless of statistical significance. A summary of globally averaged differences of selected parameters with respect to experiment **NS** are displayed in Tab. 3.5.

3.3.1 Changes in the emission parametrisation

For this comparison, the results obtained from experiments **A** and **B** are used. **A** represents the emission parametrisation as used in the standard AEROCOM setup of HAM. This means that $f_{\text{SO}_4} = 2.5\%$ (*i.e.* 2.5% of the SO_2 -emissions from ships are emitted as sulfate into the soluble coarse mode (CS) and all carbonaceous particles (BC and POM) from shipping emissions are assigned to the insoluble Aitken mode (KI) at the point of emission). For experiment **B**, the orig-

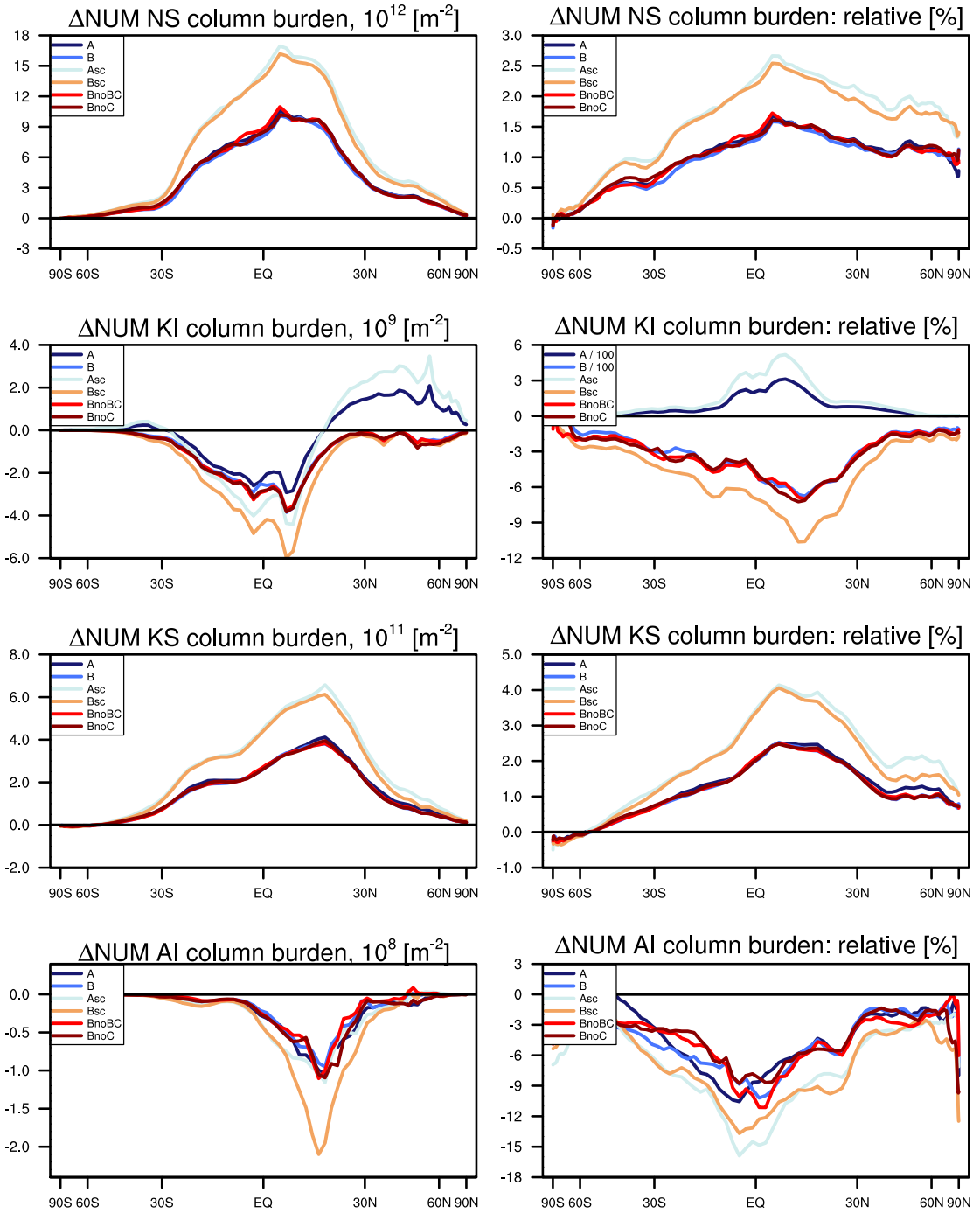


Figure 3.11: Zonally averaged absolute- and relative changes of atmospheric column number burdens with respect to NS and aerosol mode in ECHAM5-HAM: Nucleation mode soluble (NS, top), Aitken mode insoluble (KI, second from top), Aitken mode soluble (KS, second from bottom) and Accumulation mode insoluble (AI, bottom). Relative changes are derived from $\left(\frac{\text{"experiment"} - \text{NS}}{\text{NS}} \cdot 100\right)$.

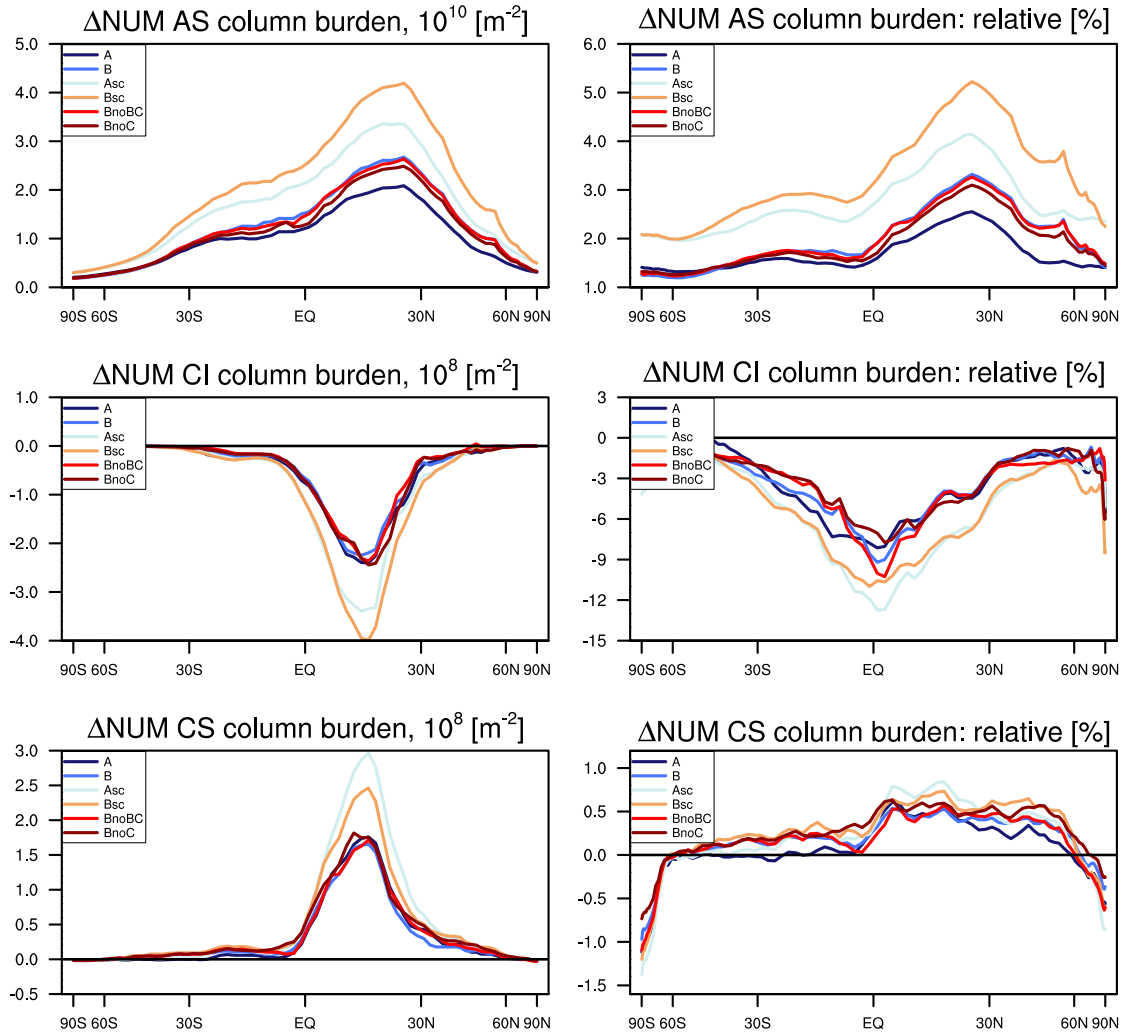


Figure 3.12: Zonally averaged absolute- and relative changes of atmospheric column number burdens with respect to **NS** and aerosol mode in ECHAM5-HAM: Accumulation mode soluble (AS, top), Coarse mode insoluble (CI, middle) and Coarse mode soluble (CS, bottom). Relative changes are derived from $\left(\frac{\text{“experiment”} - \text{NS}}{\text{NS}} \cdot 100\right)$.

inal AEOROCOM-style emission parametrisation is modified in such a way that (1) $f_{\text{SO}_4} = 4.5\%$ and the emitted sulfate particles are assigned to the soluble Aitken mode (KS) and (2) all emitted carbonaceous particles are also assigned to KS. The details of these choices are elaborated on in Ch. 3.1.5. Thus, in experiment **B**, a much larger number of primary, internally mixed particles than in experiment **A** is introduced into the model. As shown in the following, this leads to substantially different results between the two experiments with respect to aerosol processing and the subsequent effect on cloud micro- and macrophysical properties.

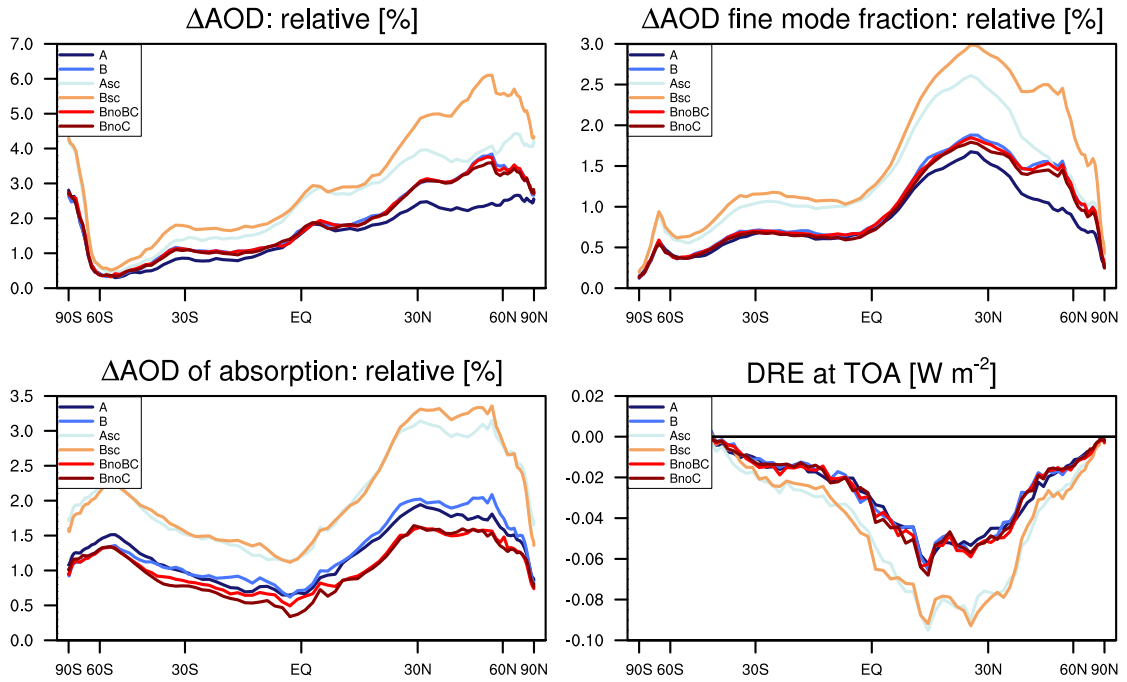


Figure 3.13: Zonally averaged relative changes of quantities related to direct aerosol-radiation interaction with respect to NS (derived from $\left(\frac{\text{“experiment”} - \text{NS}}{\text{NS}} \cdot 100\right)$): aerosol optical depth (AOD, top left), AOD fine mode (top right), AOD of absorption (bottom left). The resulting aerosol direct radiative effect (DRE) at TOA is also shown (bottom right).

3.3.1.1 Changes in species column- and number-burdens as well as clear-sky radiation

As expected, the zonally averaged relative differences of carbonaceous- and sulfuric species column burdens of the two experiments show almost exactly the same meridional patterns. For experiment **A**, carbonaceous species are slightly more abundant in the mid-latitudes of the southern- and northern hemisphere (SH and NH). This is due to a longer lifetime of carbonaceous particles in **A** compared to experiment **B** (see Tab. 3.4) because they are emitted as hydrophobic particles. These undergo less efficient internal mixing than their hygroscopic counterparts in **B** and are therefore exhibit shorter atmospheric lifetimes. For the sulfuric compounds, the expected results are obtained, *i.e.* SO_2 and sulfate being more and less abundant in **A**, respectively. This is due to the change in f_{SO_4} .

Coming to the change in particle number column burdens as obtained from the two simulations, the most pronounced differences between **A** and **B** are found for the modes KI and AS (soluble Accumulation mode). For KI, a large relative increase is obtained throughout the globe in **A**. At most, the zonally averaged relative change amounts to more than 300% close to the equator. This increase in KI column burden is however confined to the oceanic regions because no other

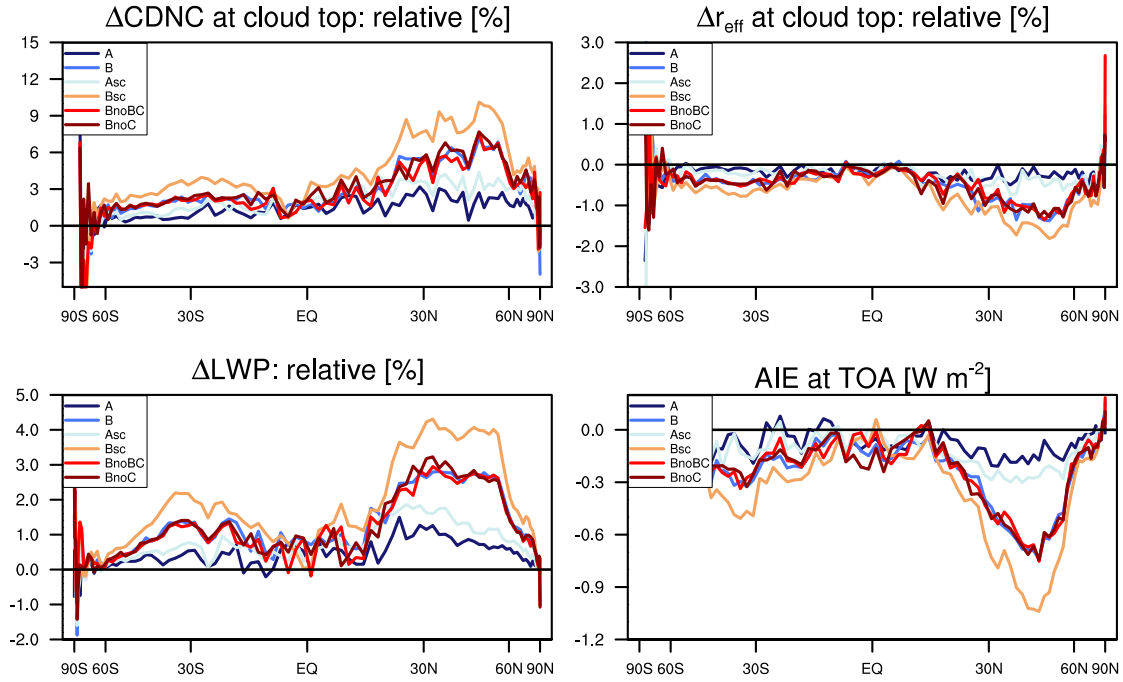


Figure 3.14: Zonally averaged relative changes of quantities related to aerosol-cloud interaction with respect to **NS** (derived from $\left(\frac{\text{“experiment”} - \text{NS}}{\text{NS}} \cdot 100\right)$): cloud droplet number concentration (CDNC) and cloud droplet effective radius (r_{eff}) at cloud top (top left and right) and cloud liquid water path (LWP, bottom left). The resulting AIE at TOA is also shown (bottom right).

source exists for such small-sized insoluble particles in those regions. In absolute numbers however, a distinct zonally averaged reduction of KI column number burden from about 30S - 15N is found. Here, the most pronounced absolute decrease in KI column number burden is simulated over South America, sub-Saharan Africa, and northern Australia. In these regions, carbonaceous emissions from biomass-burning are partly assigned to KI (Stier et al., 2005). Through the increased availability of condensable material in the mid- and upper troposphere (*i.e.* H_2SO_4 from atmospheric processing of SO_2 from shipping) these KI particles undergo internal mixing and are thus removed from that mode. Because KI column number burdens are substantially larger over land than over the ocean by several orders of magnitude, the obtained zonally averaged absolute changes are dominated by the decreases over land. Conversely, the zonally averaged relative changes are dominated by the increases over oceans, albeit these changes are small in absolute numbers. Northwards of 15N, the KI column number burden is substantially increased.

In experiment **A**, it therefore seems that the sheer amount of emitted KI particles over oceans is too large to allow for efficient internal mixing and thus particle growth, because the competition for condensable material is so high. This effect can easily be inferred from the obtained changes in AS column number burdens.

Table 3.4: Atmospheric lifetimes of the aerosol species considered in ECHAM5-HAM in experiment **NS** [days] and changes in the remaining experiments with respect to **NS** [minutes]. The lifetime is defined as the ratio of total burden over total sources. All aerosol species treated in ECHAM5-HAM are considered here, *i.e.* sulfate, black carbon (BC), particulate organic matter (POM), sea salt (SS) and dust (DU).

Compound	NS	A	B	Asc	Bsc	BnoBC	BnoC
sulfate	4.8±0.16	-7.9±2.7	-30.5±3.5	-32.8±6.3	-18.9±4.3	-29.2±5.5	0.3±1.9
BC	6.3±0.17	-3.9±7.2	-17.8±12.1	-16±10.2	-16.7±8.5	-4±3.3	10.2±13.2
POM	6.1±0.19	-7.6±9.6	-2.7±17	-11.5±14.7	-8.4±13.2	-10.4±2.6	-4.9±19.2
SS	0.7±0.006	-1.6±0.1	2.3±0.1	-1.3±0.1	0.9±0.1	2.2±0.3	-0.06±0.1
DU	4.9±0.2	1.6±7.2	-19±6.2	-11.5±11.8	-14.3±11.5	-19±9	2.3±8.9

There, the relative increase obtained from **B** is distinctly higher than that of **A**, with this difference between the two experiments being most pronounced in the NH mid-latitudes. As the column number burdens in AS are particularly important for the generation of CCN, it can already be deduced that the effect of shipping emissions on clouds is less in **A** than in **B**. The effect of the less efficient mixing processes in **A** with respect to **B** can also be deduced from the relative changes in total aerosol column number burden. There, the zonally averaged relative increase in aerosol number shows a very similar pattern for both experiments with **A** showing slightly larger values. Therefore, although the number of emitted particles is distinctly larger in **B** than in **A**, the less efficient internal mixing of the emitted KI particles in **A** leads to longer particle lifetimes and a subsequent larger increase in column number burden compared to **B**.

The resulting changes in zonally averaged aerosol optical depth (AOD) and its fine mode fraction match the changes in number burdens and are thus larger for **B** than for **A**. So despite the results from **A** yielding a slightly larger total aerosol number burden, **B** yields more particles in modes associated with larger sizes in HAM, which subsequently leads to larger aerosol column extinction or AOD. This also holds for the changes in the AOD fine mode fraction because the experimental setup of **B** leads to substantially more particles in AS (*i.e.* that mode which contains those particles about to grow to sizes $>1 \mu\text{m}$ in diameter). The changes in the AOD of absorption are also higher for **B**. This is due to internally mixed BC particles, as absorption by carbonaceous particles increases when they are internally mixed (*e.g.* Jacobson, and references therein); an effect also accounted for in the radiation module of HAM (Stier et al., 2006b). The resulting aerosol direct radiative effect (DRE) is however not much different between the two experiments: $-23.5 \pm 0.9 \text{ mWm}^{-2}$ and $-22.9 \pm 1.7 \text{ mWm}^{-2}$ for **A** and **B**.

3.3.1.2 Effects on clouds and cloudy-sky radiation

The relative change in zonally averaged CDNC at cloud top is substantially larger in **B** than **A**, on the order of 5% at NH mid-latitudes in **B** versus about 2% in **A**. Correspondingly, the r_{eff} decreases by about 1% in **B** versus $\approx 0.25\%$ in **A**. Because the implemented parametrisation of the autoconversion process allows for changes with respect to cloud droplet sizes, the changes in cloud liquid water path (LWP) also show the same distinct difference pattern. While the LWP increases by more than 2.5% over NH mid-latitudes in **B**, this increase amounts to $<1\%$ in **A**.

The cloud optical depth τ , and thus the cloud albedo, is determined by both r_{eff} and LWP. Therefore, the effect on atmospheric radiation is substantially larger in **B** compared to **A**. In fact, the globally averaged AIE from **B** amounts to $-0.22 \pm 0.008 \text{ Wm}^{-2}$ whereas that of **A** equals to $-0.07 \pm 0.017 \text{ Wm}^{-2}$. For both simulations, the zonally averaged AIE is largest over the NH mid-latitudes, amounting to about -0.7 and -0.2 Wm^{-2} for **B** and **A** respectively. In experiment **B**, it is therefore the effect of assigning more and smaller soluble particles for a given amount of emissions, which leads to more than a tripling of the AIE in ECHAM5-HAM for the model configuration used in this study.

3.3.2 Changes in the amount of emissions

Although it is illustrated that the AIE of shipping emissions as calculated by an aerosol-climate model such as ECHAM5-HAM strongly depends on the chosen emission parametrisation, a possibly more obvious AIE-determinant is investigated in this section: the uncertainty associated with total shipping emissions. For this, the results from the experiments **Asc** and **Bsc**, in which the shipping emissions are scaled by a factor of 1.63 with respect to experiments **A** and **B**, are investigated. The emission parametrisations are the same as in **A** and **B** (see Ch. 3.1.5).

With respect to the results of experiments **A** and **B**, the results obtained from **Asc** and **Bsc** show the same zonally averaged patterns, but with an offset. This offset roughly corresponds to the scaling factor which is applied to the shipping emissions and therefore implies no distinct nonlinearities in aerosol processes associated with shipping emissions. The results of selected parameters are shown in Tab. 3.5.

From experiment **Bsc**, an upper estimate of globally averaged AIEs from shipping emissions (*i.e.* $-0.32 \pm 0.01 \text{ Wm}^{-2}$) is obtained. Compared to the current best estimate of globally averaged AIE from anthropogenic activities of -0.7 Wm^{-2} (Forster et al., 2007, which considers just the first AIE), our result represents a somewhat high estimate. Although the results of **Bsc** are considered as an upper estimate, one must bear in mind that the utilised emissions represent the upper estimate for the year 2000. Because global ship traffic correlates well with world

Table 3.5: Globally averaged changes of aerosol- and cloud properties for the experiments described in Sec. 3.1.5 with respect to experiment NS, i.e. “experiment - NS”. The results for cloud droplet number concentration (CDNC) and cloud droplet effective radius (r_{eff}) represent values at cloud top as diagnosed by the model. The values in parentheses represent globally averaged relative changes in % as derived from $\left(\frac{B-NS}{NS} \cdot 100\right)$.

	A	B	A _{sc}	B _{sc}	B _{noBC}	B _{noC}
AOD	1.9E-3±0.07E-3	2.3E-3±0.1E-3	3E-3±0.07E-3	3.7E-3±0.13E-3	2.3E-3±0.07E-3	2.3E-3±0.1E-3
AOD F _{MF}	4.6E-3±0.1E-3	5.4E-3±0.08E-3	7.3E-3±0.02E-3	8.7E-3±0.15E-3	5.3E-3±0.1E-3	5.1E-3±0.1E-3
ADE [mWm^{-2}]	-23.5±0.9	-23±1.7	-38±1.5	-37.4±1.6	-24.1±0.7	-23.9±1.4
CDNC [cm^{-3}]	0.84±0.05	1.64±0.18	1.24±0.17	2.6±0.2	1.57±0.08	1.8±0.14
r_{eff} [μm]	-0.03±0.003	-0.07±0.006	-0.04±0.009	-0.09±0.005	-0.06±0.004	-0.06±0.007
LWP [kg m^{-2}]	6.6E-4±0.6E-4	2E-3±0.06E-3	1E-3±0.05E-3	3E-3±0.1E-3	2E-3±0.1E-3	2.1E-3±0.09E-3
AIE [Wm^{-2}]	-0.07±0.017	-0.23±0.008	-0.11±0.02	-0.32±0.01	-0.21±0.02	-0.22±0.02
	(0.61±0.05)	(1.43±0.05)	(0.94±0.05)	(2±0.07)	(1.37±0.12)	(1.41±0.08)
	(1.51±0.02)	(1.87±0.04)	(2.47±0.04)	(3±0.06)	(1.86±0.02)	(1.83±0.05)
	(0.86±0.03)	(1±0.02)	(1.36±0.04)	(1.62±0.05)	(1±0.02)	(0.95±0.03)
	(3.12±0.2)	(4.5±0.3)	(3.65±0.29)	(6.13±0.34)	(4.34±0.21)	(4.88±0.3)
	(-0.07±0.04)	(-0.37±0.05)	(-0.15±0.08)	(-0.58±0.04)	(-0.33±0.03)	(-0.35±0.06)

economic growth (*e.g.* Eyring et al., 2005a; Kaluza et al., 2010), AIEs from shipping emissions are bound to be even larger for current levels of shipping emissions. Furthermore, the AIE estimated from experiment **Bsc** is about half of the current upper estimate of AIEs from shipping emissions (-0.6 Wm^{-2} as given in Lauer et al., 2007).

3.3.3 Reduction of carbonaceous emissions

Experiments **BnoBC** and **BnoC** were performed to explore the effect of reducing the emission of carbonaceous particles from ships. Because of the net positive radiative forcing at TOA, the idea of reducing carbonaceous emissions as a fast global warming mitigation option has attained increasing attention in the last years. However, most of these ideas focus solely on the DRE of BC particles and do not take their capability to act as CCN into account (*e.g.* Pierce et al., 2007; Spracklen et al., 2011). In the experiments **BnoBC** and **BnoC**, the emission parametrisation as in **B** is applied, implying that carbonaceous particles stemming from shipping emissions are assigned to the soluble Aitken mode (KS) at the point of emission. Therefore, these particles can efficiently grow to CCN sizes through internal mixing and water uptake, which explains part of the substantial AIE-characteristics of **B**. Alternatively, BC-particles become more absorbing when they are internally mixed (*e.g.* by coating with H_2SO_4), which increases their contribution to aerosol absorption.

The results of the simulations **BnoBC** and **BnoC** show no substantial differences compared to experiment **B** and the main results are nearly identical. However, a closer look at specific model diagnostics reveals the effect of reducing the carbonaceous emissions quite clearly. First, the zonally averaged relative changes of BC column burdens indicate lower values in both experiments than those of the reference experiment **NS**. This is due to increased internal mixing of already present BC-particles (*e.g.* from wildfires or industrial activities) resulting from the increased availability of condensable sulfuric material. This leads to enhanced wet scavenging and thus a decreased atmospheric lifetime of BC-particles, which in total reduces their column burden. The same holds for the zonally averaged relative changes of POM column burden when considering experiment **BnoC**. As expected, the zonally averaged relative change of the AOD of absorption shows reduced values with respect to **B** for both experiments, especially in the NH mid-latitudes. Keeping these changes in BC- and POM column burdens in mind, the reduction of the absorption AOD combines the effects of both the reduction of carbonaceous emissions from ships and the general decrease of carbonaceous-compound lifetimes in the atmosphere. However, it remains an open question whether BC emissions from ships even have a positive DRE at TOA. The albedo of the ocean is typically so low that any aerosol residing in the air above it will have a negative DRE at

TOA. So by reducing BC emissions from ships, the resulting effect may be just the opposite of the envisaged, namely a less negative DRE over oceans.

Concerning the changes in particle number column burdens in **BnoBC** and **BnoC** with respect to **B**, the only aerosol mode in HAM which shows a hint of a change is AS. Here, the model calculates fewer particles throughout the NH for **BnoC**, but there is no systematic change depictable for **BnoBC**. So depending on the particle type the emission of which is reduced, it appears that the reduction of carbonaceous particles from shipping emissions may have different impacts on atmospheric radiation. The reduction of just BC-particle emissions leads to a reduction of absorption AOD throughout the globe which may partly offset the strongly positive anthropogenic radiative forcing of climate. On the other hand, the reduction of POM leads to a decrease of particle numbers in AS (*i.e.* the aerosol mode in HAM which holds responsible for contributing CCN), which could lead to a reduced net radiative cooling at TOA. The changes in aerosol-species lifetimes shown in Tab. 3.4 also suggest the potential importance of at least POM emissions for the CCN budget. Compared to the other experiments, the lifetime of sulfate is not reduced, which indicates that POM from shipping emissions represents an important condensational sink for H_2SO_4 .

However, the obtained zonally averaged relative changes concerning cloud- and atmospheric radiative properties do not give such a clear picture and the differences with respect to experiment **NS** are similar to those of **B**. Although the number of emitted particles is surely lower in **BnoBC** and **BnoC** compared to **B**, the effect of shipping emissions on clouds and radiation is nearly unchanged. This illustrates the effect of the large amount of sulfuric emissions from ships, both as gaseous SO_2 and primary sulfate, which dominates over the relatively small amount of carbonaceous emissions (see Tab. 3.2).

These results however do not deny the possible effectiveness of reducing BC emissions from anthropogenic activities as a fast option to mitigate the anthropogenically induced increase of global surface temperature. BC stemming from anthropogenic activities is emitted mostly over land, where the respective particles undergo less efficient internal mixing and thus exhibit longer atmospheric lifetimes compared to those emitted over oceans. Furthermore, the albedo of the land surface is higher than that of ocean-surfaces so that the DRE of BC particles at TOA is positive.

3.4 Summary

The aerosol climate model ECHAM5-HAM was used to quantify the aerosol indirect effect (AIE) from shipping emissions. For this, the shipping emissions inventory from Behrens (2006) was used and the experiments were designed to investi-

gate the uncertainty of the derived radiative forcing (RF) associated with the uncertainty in the shipping emissions themselves. For these experiments, ECHAM5-HAM was nudged with ERA-Interim re-analysis data, sea surface temperatures (SSTs) were prescribed by AMIP data, and the model integrations span the time frame of October 1999 – December 2004. The first three months were used as model spin-up and discarded from the analysis.

The sensitivity experiments consisted of three sets of simulations in which the following key uncertainties/questions, with respect to AIEs, were assessed:

1. Uncertainty in the emitted particle-size distribution and -composition
2. Uncertainty in amount of emissions
3. What is the effect of reducing carbonaceous emissions from shipping ?

The first uncertainty was addressed by modifying the originally implemented emission parameterisation (AEROCOM, Dentener et al., 2006). Compared to that parameterisation, the particles from shipping emissions are all assigned to a soluble and/or smaller aerosol mode with a higher fraction of emitted SO₂ directly emitted as particulate sulfate in the modified emission parameterisation. Thus, the modified emission parameterisation leads to the emission of substantially more soluble particles. These modifications to the emission parameterisation are within the observed ranges (see Ch. 3.1.5).

The second uncertainty arises from the fact that the global annual amount of fuel consumed by ship traffic is still not fully constrained. There do exist relatively low and high estimates of annual fuel consumption, with the emissions inventory employed in this study (Behrens, 2006) providing an estimate which is on the lower end. Therefore, the emissions were scaled to meet the highest published value (see Ch. 3.1.5). This frames this emission sensitivity analysis within the range of published uncertainties.

For quantifying the third question, two simulations were performed. One in which all black carbon (BC) emissions from shipping are omitted and one in which all BC- and particulate organic matter (POM) emissions are omitted.

To assess the impact of shipping emissions on the radiation budget, their RF from shipping emissions is defined in terms of a “radiative-flux perturbation” (Lohmann et al., 2010), defined as the average net shortwave radiation at the top of the atmosphere (TOA) subtracted by the instantaneous aerosol direct radiative effect obtained from a double-call of the ECHAM5 radiation code.

The different model experiments yield substantially different RFs at TOA and the upper estimate of the AIE at TOA from shipping emissions is found to be $-0.32 \pm 0.01 \text{ Wm}^{-2}$. This is a factor of two less than the upper estimate from Lauer et al. (2007), who also used the ECHAM5 model, but coupled it to a different

aerosol sub-model. The above-mentioned experiment was run with the modified emission parametrisation and scaled emissions.

Concerning the effect of shipping emissions on clouds, it is found that the emission size distribution matters far more than the amount of total emissions. Even in the case of scaled emissions, the experiment with the original emission parametrisation yields an AIE at TOA of $-0.11 \pm 0.02 \text{ Wm}^{-2}$, showing how the forcing increases by a factor of three when employing the modified emission parametrisation. This also holds for the cases with unscaled emissions, where the experiments employing the original- and modified parametrisation yield an AIE at TOA of $-0.07 \pm 0.017 \text{ Wm}^{-2}$ and $-0.23 \pm 0.008 \text{ Wm}^{-2}$ respectively.

The removal of carbonaceous aerosol from the shipping emissions proved not to have a substantial impact on the obtained AIE. Therefore, the results obtained from studies advocating for the importance of carbonaceous CCN (*e.g.* Pierce et al., 2007; Spracklen et al., 2011) are not confirmed for shipping emissions in our model. However, it is recognised that carbonaceous emissions from ships provide an important condensational sink for sulfuric compounds. These results also indicate potentially important regional reductions of the aerosol optical depth of absorption.

COMBINING MODELLING AND SATELLITE APPROACHES

In this chapter, a detailed comparison of the simulations of the impact of shipping emissions on clouds in ECHAM5-HAM (see Ch. 3) with the satellite data analysis (see Ch. 2) is performed. For this, the Eulerian sampling approach as described in Ch. 2.4.1 is applied to the modelling results of the control case (**NS**) and two sensitivity experiments (**A** and **Bsc**). Additional to the cloud- and aerosol parameters that were studied in the satellite data analysis, possible changes in atmospheric composition in the shipping corridors were also investigated.

It is found that there do exist marked changes in atmospheric composition in the shipping corridors and that there even exists a distinct change in across-corridor gradient at the location of a shipping lane. However, cloud properties are modified across the whole breadth of the shipping corridor rather than just at the location of the shipping lane, thereby confirming the findings of the satellite data analysis.

4.1 On the benefits and issues of comparing satellite- to model data

The combined use of satellite- and re-analysis data for investigation of the influence of shipping emissions on large scale cloud fields is discussed in Ch. 2. The results from that study however lead to the conclusion that it is not possible to disentangle the effects of both the large-scale meteorology and micro-physics on clouds in the considered regions. The approach described in Ch. 2 may be hampered by several factors: (1) there is no “control case”, (2) dynamical factors controlling marine boundary layer convection cannot be accounted for and (3) the satellite data retrieval algorithms for cloud properties do not give all too robust results for broken cloud fields such as those present in the regions of interest.

With the performed ECHAM5-HAM simulations described in Ch. 3.1.5 the results from the model can be compared to those obtained from the satellite study. The use of the model results eliminates two of the three limitations of the satellite data mentioned above. First, there exists a control case for which the model was run without any shipping emissions. Second, the results obtained for the micro-physical cloud- and aerosol properties do not depend on uncertainties in satellite data retrieval algorithms but are taken directly from the model. One must keep in mind that comparing model results directly to satellite data is not straight forward, though. When using data from passive remote sensing instruments performing measurements in the visible- and near-infrared spectral range (such as MODIS), cloud obstruction is most probably the most important factor to consider. By using such an instrument, only the properties of the uppermost cloud-layer of the sampled atmospheric column can be determined accurately (more or less) because the upwelling radiances from possibly present lower cloud layers do not reach the satellite sensor. Thus, especially the analysis of multi-level cloud systems is not feasible by using an instrument such as MODIS. Furthermore, instruments mounted on polar-orbiting satellites such as EOS-Aqua and -Terra perform measurements of a particular region at most once a day (at the same time). Additionally, geophysical quantities derived from satellite remote sensing are subject to inherent uncertainties associated with the underlying retrieval algorithms and often, a large amount of measurements has to be analysed in order to obtain a reasonable signal-to-noise ratio.

When comparing different datasets of whatever nature, it is of great use to prepare them in such a way that most of the differences between the datasets are accounted for. For the case of comparing satellite instrument derived quantities to those obtained from a GCM, it is obvious that the satellite dataset is the one with the more peculiarities to look out for. To account for this, the sampling of the model data should be as close to that of the satellite data. In the following, two approaches, often dubbed “satellite-simulators”, to do so are shortly discussed.

In the first approach, the limitations of the satellite data concerning cloud obstruction and temporal resolution are roughly accounted for. The three-dimensional cloud-field from the model is sampled at the corresponding local time of the assumed satellite overpass and only the micro- and macrophysical properties of the uppermost cloud layer are used. The cloud fraction at TOA is computed by using a cloud-overlap assumption, such as maximum-random overlap, for the respective atmospheric column. So for this approach, the sampling issues of the satellite sensor are very much completely accounted for but the uncertainties associated with the retrievals themselves is not addressed.

The second, more advanced approach on the other hand also accounts for those uncertainties. For this, the model-calculated outgoing radiation at TOA is sim-

ulated at certain wavelengths and these are then fed into a retrieval algorithm which closely represents that of a certain satellite instrument, *i.e.* the results are such as if the satellite were actually flying over the modelled atmosphere. Thus, compared to the first approach, the geophysical quantities derived by use of this approach are most probably better comparable to those retrieved from actual satellite measurements. A comprehensive description of COSP (CFMIP (Cloud Feedback Model Intercomparison Project) Observation Simulator Package), a software product available for exactly that purpose, can be found in Bodas-Salcedo et al. (2011).

Although the use of either one of these approaches has been shown to give substantial added-value to global-modelling results (*e.g.* Quaas et al., 2006; Gehlot, 2010; Nam, 2011), a somewhat reduced version of the first approach is used in this study. Cloud properties, *i.e.* r_{eff} and CDNC are diagnosed at cloud top but there is no constraint concerning the local time of day; the sampling approach is detailed in the next section.

4.2 Sampling approach

To achieve a high degree of comparability between the results of the satellite data analysis presented in Ch. 2 and those obtained from the simulations with ECHAM5-HAM presented in Ch. 3, the model output is sampled according to the Eulerian approach illustrated in Ch. 2.4.1. The positions of the shipping lanes are chosen identically to those in the satellite study but the spatial resolution of the sampling was modified to better match the model resolution. In the satellite data analysis, the averaging boxes for cloud- and aerosol parameters were of the size of $0.3^\circ \times 0.3^\circ$. For the model data, which come at a resolution of $1.8^\circ \times 1.8^\circ$ (T63 spectral resolution), such small averaging boxes would be of use; the averaging domain is therefore increased to $2^\circ \times 2^\circ$. This basically means that the values in each “averaging box” are represented by those of just one single model grid box. The distance between the averaging lines parallel to the shipping lane was also increased: 1° compared to 0.5° in the satellite data analysis. This already hints at the disadvantage of using model data: there is basically no spatial variability in the obtained cloud- and aerosol fields near the position of the shipping lane. On the other hand, model data offers the advantage of supplying data at every model output time step which substantially enhances the sampling frequency compared to the satellite data.

The quantities describing the large scale meteorological environment, *i.e.* wind speed and -direction at 10 m height, sea surface temperature (SST), lower tropospheric stability (LTS) and boundary layer height (BLH), are taken from the model output. All available data from the model runs is used, that is this analy-

sis covers the time period from 2000 – 2004 and the output data are provided at six-hour intervals.

The analysis of cloud properties is performed with respect to liquid-water clouds only. For this, a gridbox suited for the analysis of liquid cloud properties has to yield

$$c_{ph} = 1 + \frac{q_w}{q_w + q_i} = 2, \quad f \geq 0.05, \quad (4.1)$$

with q_w and q_i being the cloud liquid water and -ice contents and f the cloud fraction in a grid-box. Eq. 4.1 is applied for $q_w > 0$, *i.e.* it can only be equal 2 if $q_i = 0$, which then defines a liquid water cloud. If a respective model column contains such a liquid water cloud valid for retrieval, a check for mixed-phase- and ice clouds overlying the liquid water cloud is performed. So if there exist grid boxes with $1 < c_{ph} < 2$ in a model layer above the detected liquid water cloud, that particular model column is discarded from further analysis. In the end, the analysis of cloud properties from the model data is thus performed in scenes in which the model calculates the presence of liquid water clouds in the model column only. This sampling of the model data therefore provides a very good basis for comparing them to the satellite data which similar filtering methods were applied to.

Diagnosis of cloud properties is then performed by conditionally sampling of the model output according to the filtering described above. Cloud droplet effective radius (r_{eff}) and cloud droplet number concentration (CDNC) are the values at cloud top as diagnosed from the model. Cloud optical depth (τ) and cloud liquid water path (LWP) are obtained by integrating over all model levels which contain liquid water clouds according to Eq. 4.1. The cloud properties are weighted, *i.e.* the values represent “in-cloud”- and not grid-box mean ones, and only used if $\tau > 4$ (as in satellite data analysis). The cloud top temperature (CTT) is defined as the temperature of the model layer which contains the uppermost valid liquid water cloud.

Additional to the cloud properties, the output of ECHAM5-HAM gives a wealth of information which help to diagnose the aerosol processes leading to possible changes in cloud properties (see *e.g.* Ch. 3.2). Therefore, the Eulerian analysis framework is also applied to model diagnostics like (1) column burdens of SO_4 , BC and POM, (2) column particle number- and mass burdens with respect to aerosol mode and (3) cloud condensation nuclei (CCN) column number burdens. Of course, aerosol radiative properties like aerosol optical depth (AOD) and its fine mode fraction (FMF) are also sampled.

4.3 Results

The results from this analysis are presented in a similar fashion as those of the satellite data analysis (see Ch. 2.4.2). Because experiments **A** and **Bsc** represent the lower and upper bound of the models' response to shipping emissions, respectively, only the results from these two experiments are discussed here. For the properties which represent the imposed change on the system, relative changes with respect to experiment **NS** are shown. Only the results obtained for sulphuric species and BC are discussed because (1), it was shown in Ch. 3.3.3 that it is the change in sulphuric emissions which has the most influence on cloud properties and (2), the across-corridor gradients are almost identical for BC and POM. For sulfate-, BC- and CCN column burdens, changes associated with the 20 lowest model levels of ECHAM5-HAM are also provided. In the model setup used for this study (31 vertical levels), the 20 lowest levels approximately correspond to the range from the surface to 680 hPa, *i.e.* the vertical subset which represents those clouds classified as being “low” in ISCCP (*e.g.* Rossow and Schiffer, 1991; Gehlot, 2010). This sub-sampling is applied because the results presented in Ch. 3.2 showed that substantial changes in both sulfate- and CCN concentrations occur throughout the troposphere. Limiting the analysis to the air masses below 680 hPa thus enables a better evaluation of the potential effect of shipping emissions on liquid-water clouds in ECHAM5-HAM.

For those quantities related to both aerosol indirect- and direct radiative effects, both absolute values and relative changes with respect to experiment **NS** are shown. By showing absolute values, the comparison with the satellite analysis as made as straight forward as possible. Investigating the relative changes yields more quantitative insights into the model results.

For reference purposes, across-corridor gradients associated with emission fluxes of sulphuric (S) species from ships, as incorporated into experiment **Bsc**, are displayed in Fig. 4.3. Compared to Fig. 2.2, the emissions appear much more spread out across the shipping corridor, which is due to the interpolation to the model's T63 resolution ($1.8^\circ \times 1.8^\circ$ versus $1^\circ \times 1^\circ$ of the original data as provided by Behrens (2006)). Regarding the share of the shipping emissions in the total S-emissions it is important to note that emission of dimethyl sulphide represents a large source of S over oceans. Therefore, the share of shipping emissions is just on the order of 10–20% for the SE Pacific and mid Indian Ocean shipping corridor. In the mid Atlantic Ocean shipping corridor, shipping emissions have a much larger share in the total emissions, which amounts to $\approx 70\%$ in the polluted part of the corridor. Concerning emissions of black carbon (BC) and particulate organic matter (POM), the share of shipping emissions is close to 100% over all oceans (see also Fig. 3.2).

Across-corridor gradients of SST, LTS or BLH are not provided here because

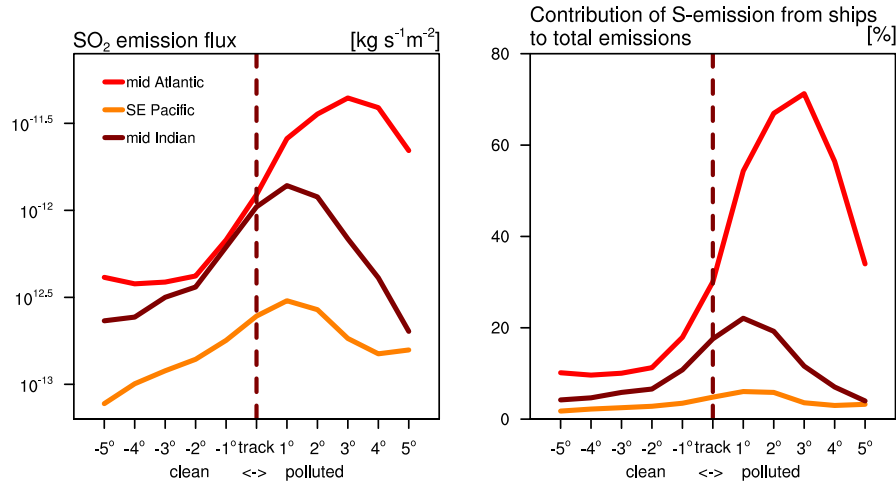


Figure 4.1: Across-corridor (*i.e.* the shipping corridors used in Ch. 2) gradients associated with the shipping emission from Behrens (2006) as implemented in experiment **Bsc**. **Left panel:** Annual mean ship-emission fluxes (\log_{10} scale); **right panel:** Share of the sulphur (S) emissions from ships in the total emission fluxes in [%] derived from $\left(\frac{S_{\text{ship}}(\mathbf{Bsc})}{S_{\text{total}}(\mathbf{Bsc})} \cdot 100\right)$. Compare to Fig. 2.2.

these are largely similar to the gradients found in the satellite data analysis. This is because ERA-Interim re-analysis data were used for both the nudging of the model simulations and the characterisation of the meteorological environment for the satellite data analysis. The SSTs in the model correspond to those provided for the AMIP II, which rely on observations and should thus be very similar to the observations used in Ch. 2.

SE-Pacific Ocean

For the SE-Pacific region, quantities associated with the change in atmospheric composition are displayed in Fig. 4.2 and those quantities associated with the resulting aerosol indirect- and direct radiative effects in Figs. 4.3 and 4.4. The relative changes in atmospheric column burdens of sulphuric compounds indicate an overall increase throughout the entire shipping corridor for the considered model simulations. As expected, this overall increase is larger for experiment **Bsc** compared to **A**. However, the rate of increase in the column burden of the sulphuric compounds shows no distinct change at the position of the shipping lane in this region, which is expected from the emission-related gradients shown in Fig. 4.3. The relative changes in BC column burden are an order of magnitude less than those obtained for the sulphuric ones. It is however interesting to note that despite scaling of the emissions, the change in BC column burden of the lower troposphere is less in experiment **Bsc** compared to **A**. So in the end, the change in atmospheric column burden associated with the reduction of BC-particle lifetimes in **Bsc** (see Tab. 3.4) even overcompensates the increase in the emission of those particles.

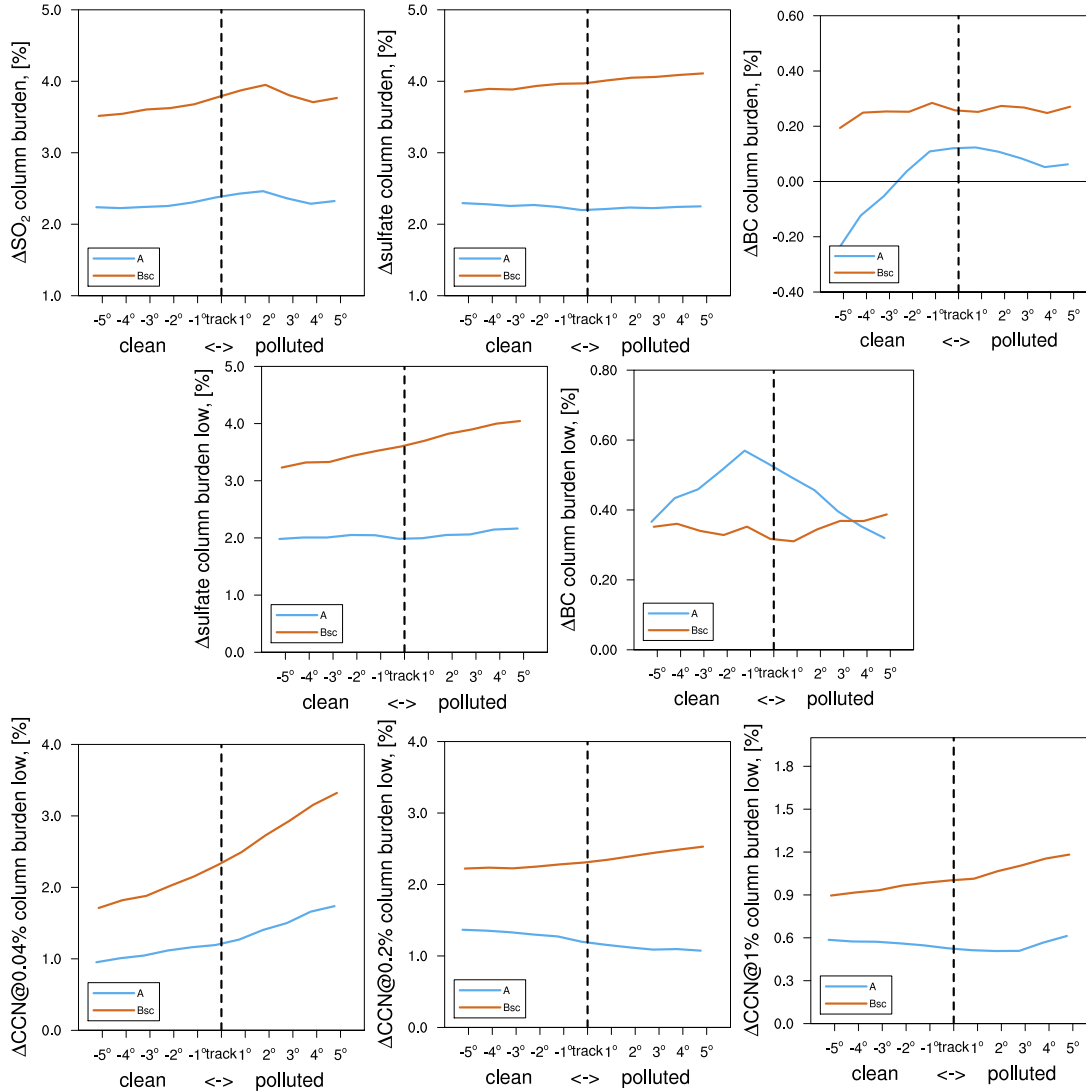


Figure 4.2: Five-year mean values of properties representing the imposed change of atmospheric composition due to shipping emissions for the **SE-Pacific Ocean** region obtained from applying the Eulerian analysis approach to the model simulations **NS**, **A** and **Bsc** (see Ch. 3.1.5). Panels (from left to right) show relative changes with respect to **NS**: **1st row**: SO₂-, sulfate- and BC total column burdens, **2nd row**: sulfate- and BC column burdens of the lower troposphere (\approx surface - 680 hPa), **3rd row**: CCN burdens at supersaturations $S=0.04\%$, 0.2% and 1% (CCN(0.04%), CCN(0.2%) and CCN(1%)) of the lower troposphere. Compare to the across-corridor gradients of shipping-emissions in Fig. 2.2

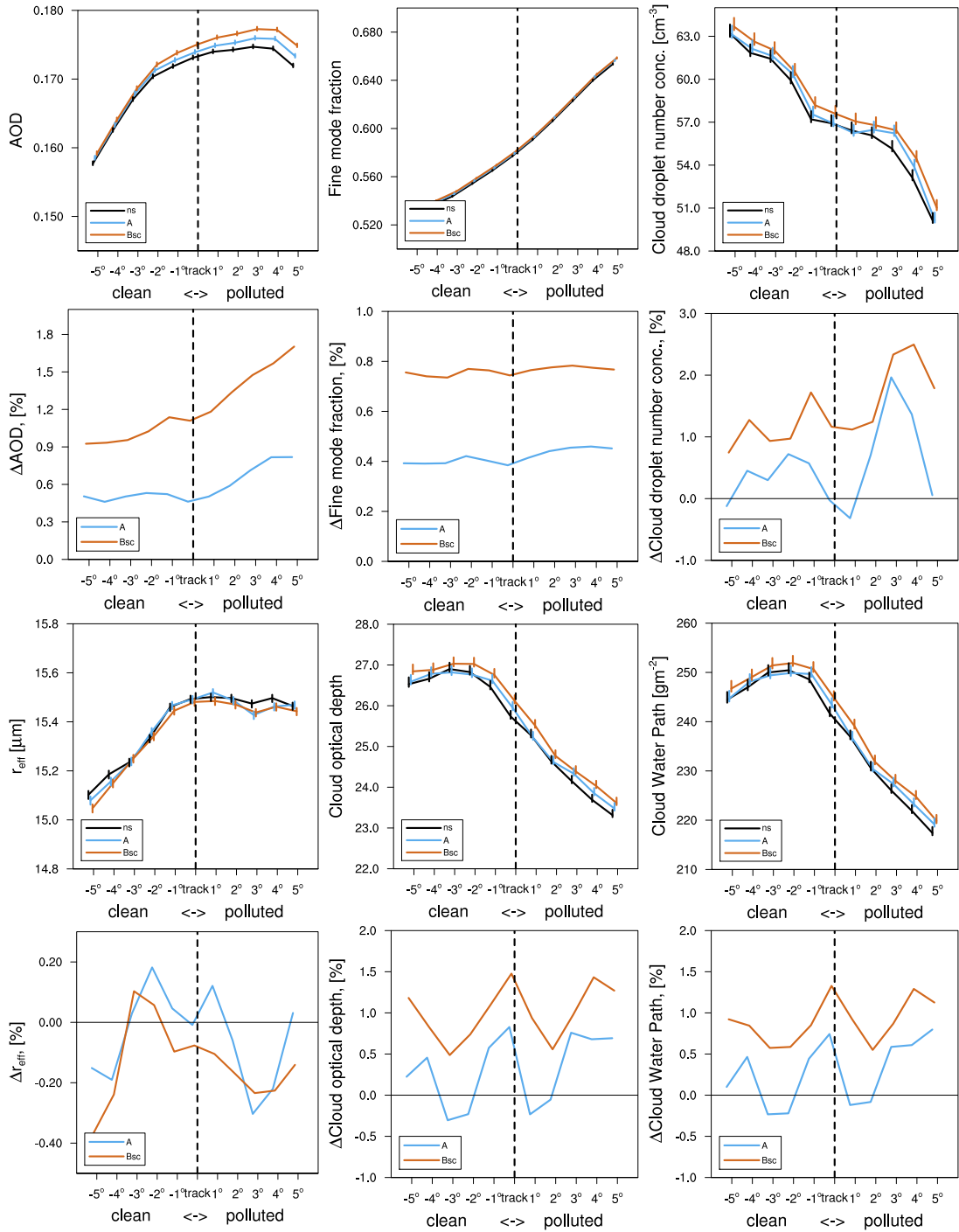


Figure 4.3: Five-year mean values of quantities related to both aerosol direct- and indirect effects from shipping emissions for the **SE-Pacific Ocean** region obtained from applying the Eulerian analysis approach to the model simulations **NS**, **A** and **Bsc** (see Ch. 3.1.5). Panels from left to right show: **1st and 2nd row:** AOD, AOD fine mode fraction and CDNC; **3rd and 4th row:** r_{eff} , τ and LWP. Rows **1** and **3** show absolute values, rows **2** and **4** show relative changes with respect to **NS**.

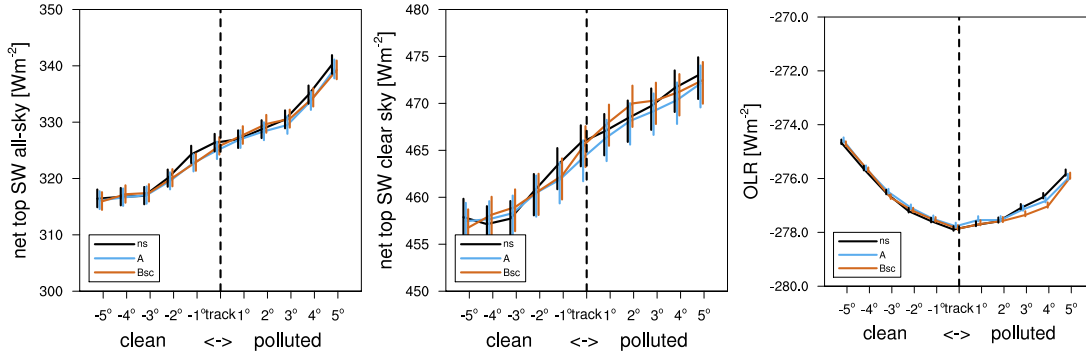


Figure 4.4: Five-year mean values of TOA radiative properties for the **SE-Pacific Ocean** region obtained from applying the Eulerian analysis approach to the model simulations **NS**, **A** and **Bsc** (see Ch. 3.1.5). Panels from left to right show: net shortwave all-sky, net shortwave clear-sky and outgoing longwave radiation (OLR).

The relative changes in the CCN-burdens integrated from the surface to ≈ 680 hPa (see Fig. 4.2, bottom row) also show a general increase across the breadth of the shipping corridor and as expected, changes are more positive for experiment **Bsc** compared to **A**. For experiment **Bsc**, the increase in CCN column burdens gets more positive towards the polluted part of the shipping corridor for all S which confirms the alteration of the ambient aerosol population by shipping emissions. For experiment **A** on the other hand, the relative increase in CCN column burdens decreases for CCN(0.2%) and CCN(1%) in the polluted part. For both experiments, the largest across-corridor increases are obtained for CCN(0.04%) which indicates a shift of the overall aerosol particle size distribution towards larger sizes. This is most probably accommodated by the increased particle growth rates discussed in Ch. 3.2.

As indicated above, the relative changes in CCN burdens of the lower troposphere are on the order of a few percent but show distinct changes at the location of the shipping lane. Of the properties having implications for atmospheric radiation, it is only the total AOD which also shows a distinct change in across-corridor gradient at the position of the shipping lane. However, this change in AOD is small ($\approx 1.5\%$). The obtained changes in micro- and macrophysical liquid-cloud properties do not give such a clear impression. Similar to the results obtained from the satellite analysis, cloud properties exhibit substantial across-corridor gradients which are associated with the gradients of the large-scale meteorological environment. However, it can be easily seen that clouds are slightly modified throughout the shipping corridor in a manner consistent with AIE hypotheses: r_{eff} is mostly decreased, τ , CDNC and LWP are increased. Therefore, shipping emissions do have an impact on clouds in this shipping corridor but this impact is neither just limited to those clouds in the polluted part of the corridor, nor do the cloud properties exhibit a distinct change at the point of the shipping lane. This is also evident in

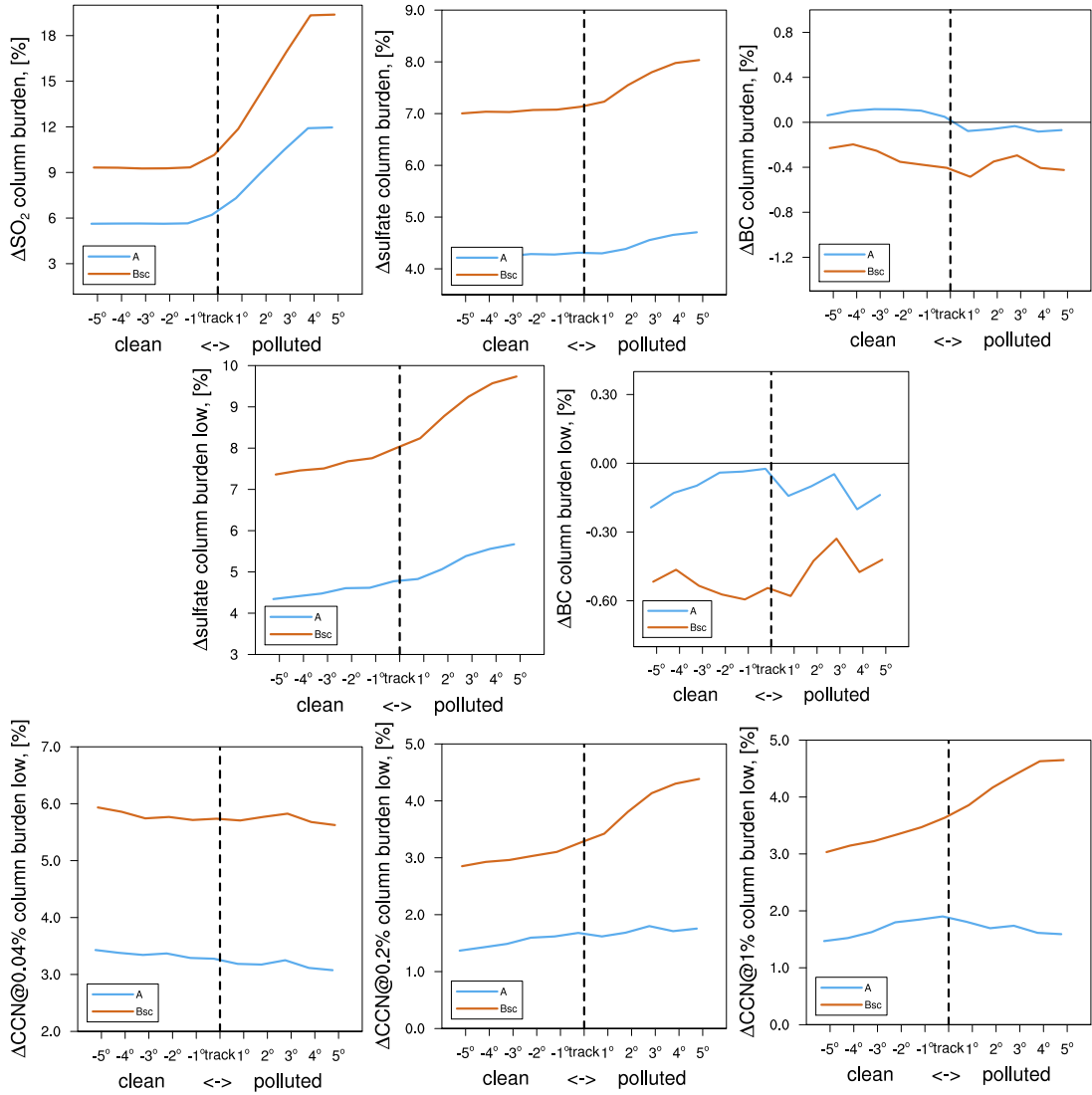


Figure 4.5: As Fig. 4.2, but for the **mid-Atlantic Ocean** region

the across-corridor gradients of TOA radiative properties shown in Fig. 4.4 where neither the results from **A** nor the ones from **Bsc** show marked differences to the ones of **NS**.

So for the SE Pacific region, the simulations with ECHAM5-HAM indicate a pronounced change in CCN column burdens, integrated from the surface to ≈ 680 hPa, at the point of the shipping lane which is not evident from the changes in aerosol-species burdens. Nevertheless, the total AOD is subject to distinct modifications at the location of the shipping lane. Micro- and macrophysical cloud properties show an offset-like change consistent with AIE-hypotheses across the whole breadth of the shipping corridor and show the same substantial across-corridor gradients as found for the satellite data analysis.

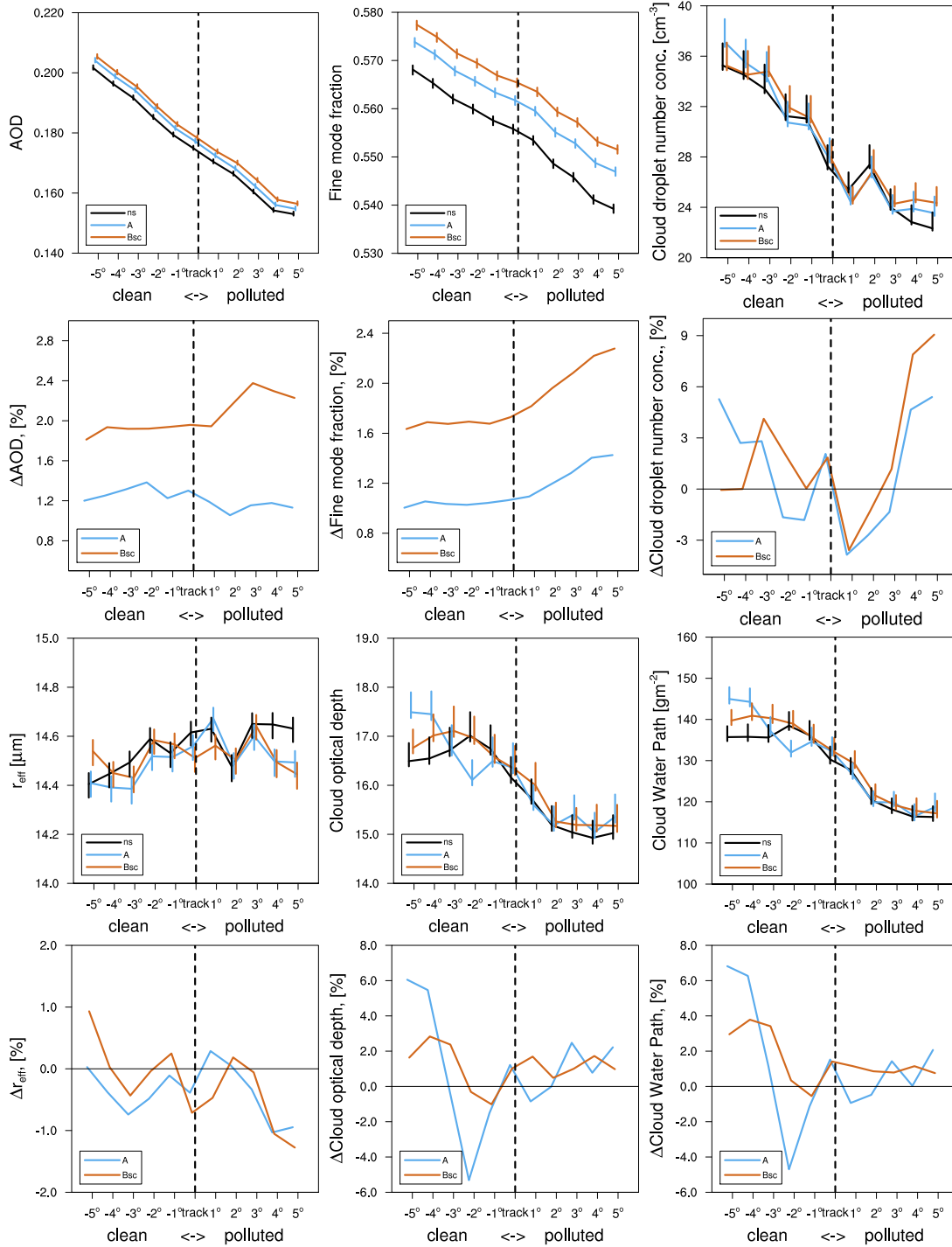
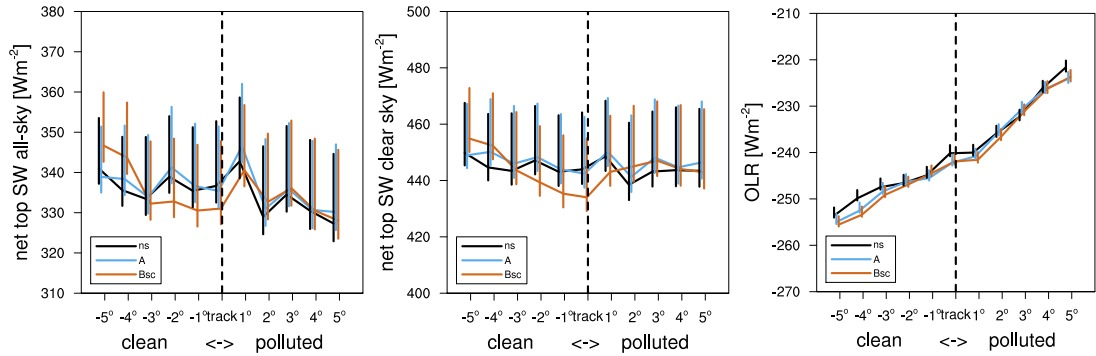


Figure 4.6: As Fig. 4.3 but for the **mid-Atlantic Ocean**

Figure 4.7: As Fig. 4.4 but for the **mid-Atlantic Ocean**

Mid-Atlantic Ocean

The results from applying the Eulerian sampling approach to the mid-Atlantic region are shown in Figs. 4.5, 4.3 and 4.7. Compared to the SE-Pacific region discussed in the preceding part, the mid-Atlantic shipping corridor is subject to a substantially larger amount of shipping emissions (see Fig. 4.3). In fact, the shipping emissions in this corridor lead to a pronounced increase in SO_2 total column burden of about 12% and 20% in experiments **A** and **Bsc**, respectively. The SO_2 column burden increases sharply at the point of the shipping lane but it is also increased in the clean part with respect to experiment **NS** due to the overall global atmospheric increase in SO_2 . The relative increases in particulate sulfate total-column- and lower-tropospheric burdens are less than that of gaseous SO_2 . Nevertheless, the stronger increase from the location of the shipping lane into the polluted part of the corridor is evident. Similar to the results obtained for the SE Pacific region, the relative changes in BC column burdens are small. For the mid-Atlantic region however, the results show continuous changes in across-corridor direction consistent with expectations: the change is more negative in the polluted part of the corridor which indicates the reduced atmospheric lifetime of BC particles which even overcompensates for the increased emissions. For the same reason, BC column burdens (in the polluted part) are lower for experiment **Bsc** compared to **A**.

From these results, a pronounced change in CCN column burdens for the lower troposphere can also be expected. Indeed, CCN column burdens in the lower troposphere increase in all experiments (as much as $\approx 6\%$), but the across-corridor gradients of these increases show differences depending on S . On the one hand, the relative changes in CCN(0.04%) column burdens show either decreasing- or about constant increase-rates in across-corridor direction. So overall, the particle size distribution is shifted towards larger sizes. But getting closer to the shipping lane, the additional amount of small particles provides for the lower increase towards the polluted part. For the changes in CCN(0.2%) column burdens, experiment **A** shows an overall increase in burden but there is not distinct change at the

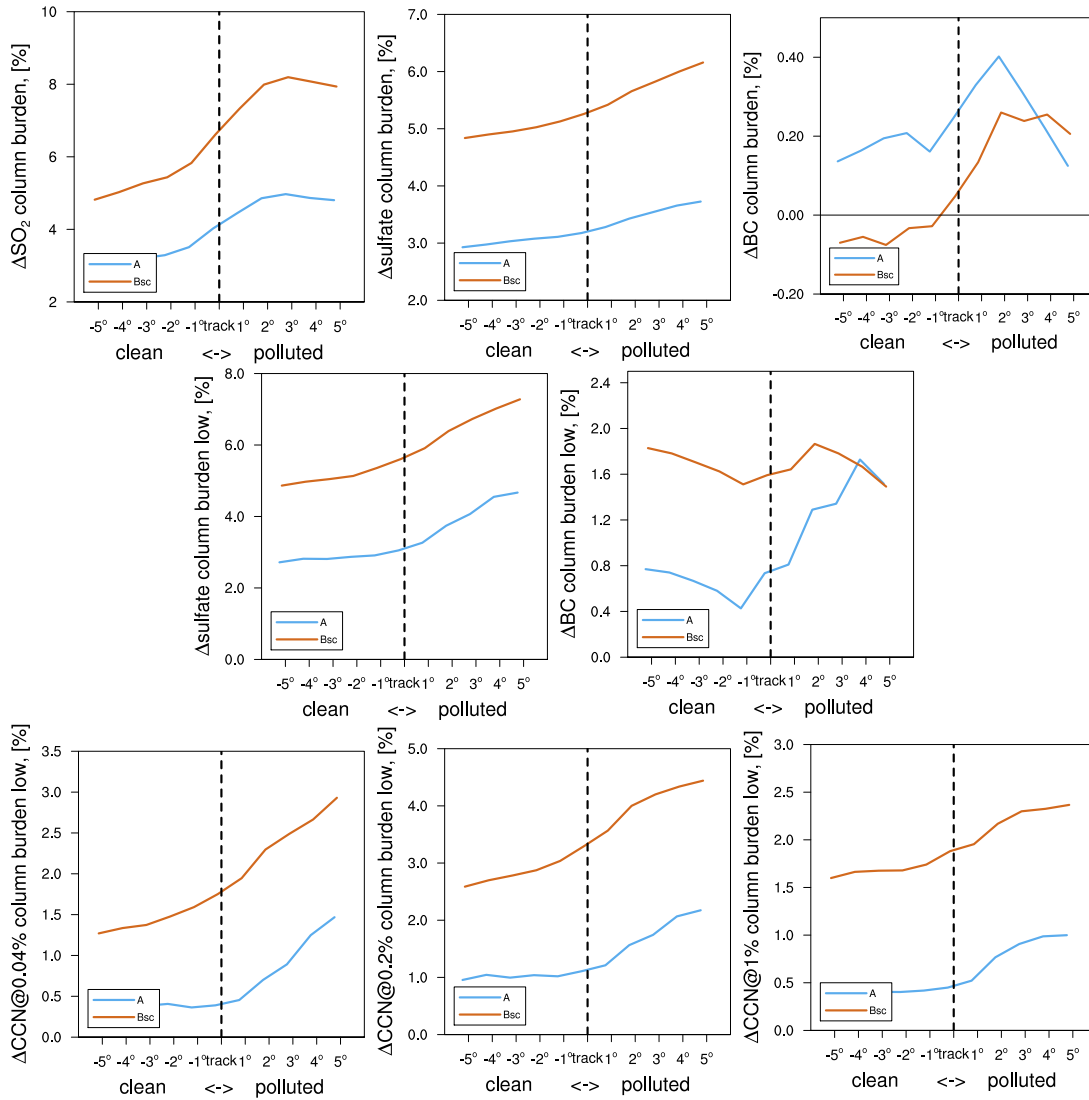


Figure 4.8: As Fig. 4.2, but for the **mid-Indian Ocean** region

shipping lane. In experiment **Bsc**, the $\text{CCN}(0.2\%)$ column burden also increases in the clean part but the increase is distinctly more positive in the polluted part. Identical results are found for the changes in $\text{CCN}(1\%)$ column burdens. So in the mid-Atlantic region, shipping emissions lead to a general increase in CCN concentrations with the actual emissions at the point of the shipping lane being most visible for high values of S , *i.e.* when considering small particles.

Regarding the impact of the imposed shipping emissions on atmospheric radiation, the changes in the aerosol population lead to a general increase in total AOD in both experiments ($\approx 1\text{-}2\%$). The increased emissions at the shipping lane are not apparent in the total AOD, most probably because the background AOD is quite high in this region (*i.e.* due to biomass-burning- and dust aerosol). However, the increase in AOD FMF shows a distinctly more positive change in across-corridor gradient from the location of the shipping lane onwards.

The sometimes relatively large changes in CCN column burdens of the lower

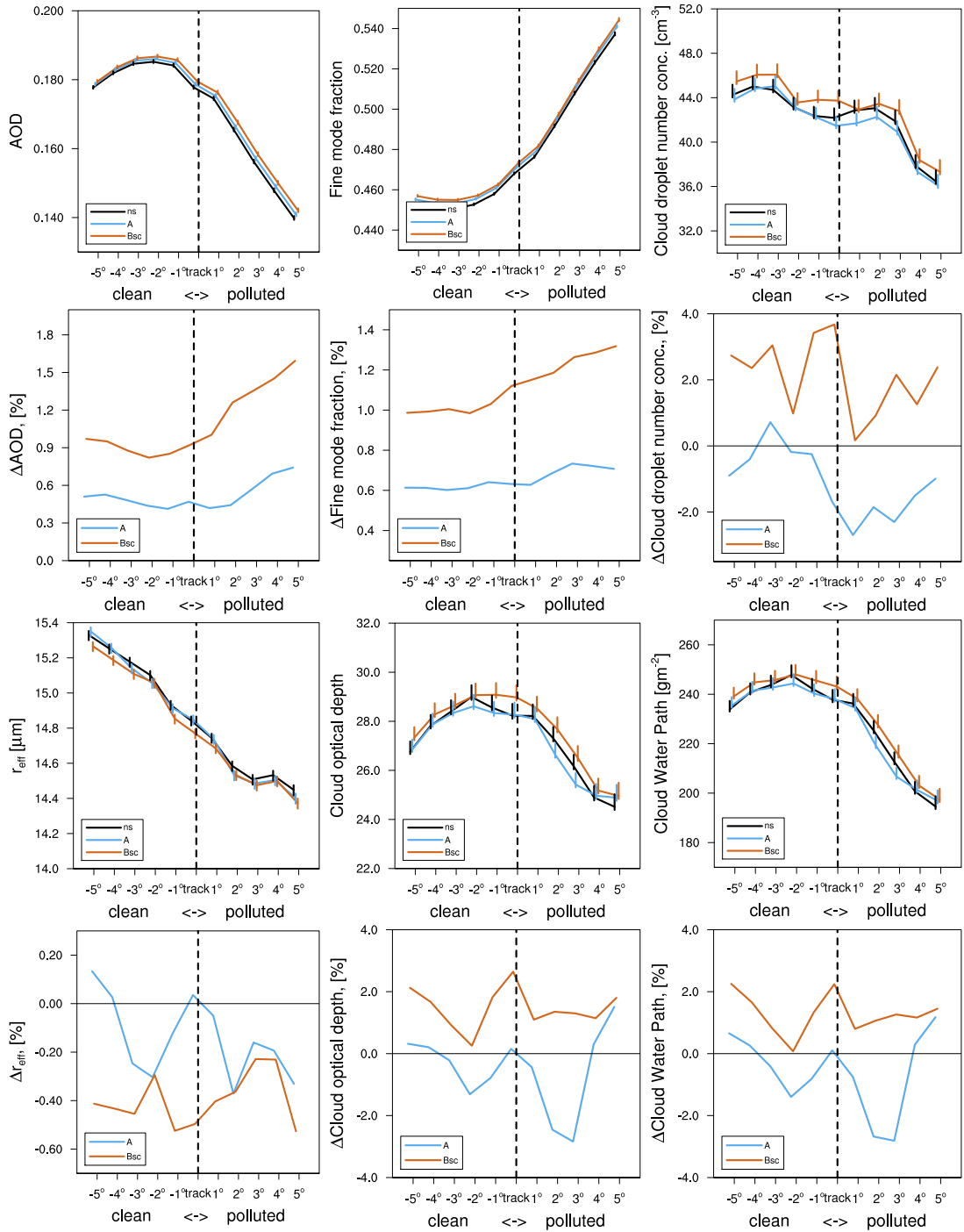


Figure 4.9: As Fig. 4.3 but for the **mid-Indian Ocean** region.

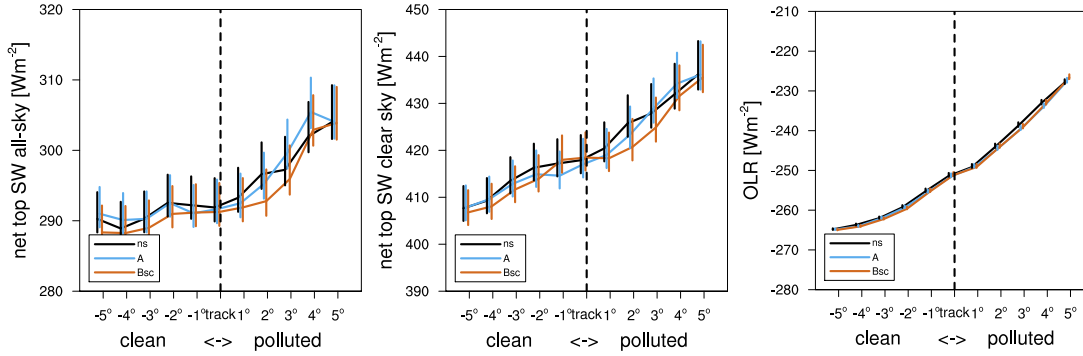


Figure 4.10: As Fig. 4.4 but for the **mid-Indian Ocean**

troposphere could indicate a substantial effect on liquid-water clouds and cloudy-sky radiation in the shipping corridor of the mid-Atlantic region considered here. Indeed, the CDNC increases distinctly in the polluted part of the corridor for both experiments. However, there is no such evident systematic change in cloud properties relevant for atmospheric radiation, *i.e.* τ or LWP. Interestingly, those properties show a larger spread among the three experiments in the clean- than in the polluted part of the shipping corridor. This is also apparent from the TOA radiative properties shown in Fig. 4.7.

Concluding, shipping emissions in the shipping corridor covering the routes from Africa to South America lead to a substantial increase in atmospheric column burdens of sulphuric compounds. Because sulphuric compounds are known to provide a substantial amount of CCNs, this could indicate a large effect of shipping emissions on clouds in this shipping corridor. Indeed, CCN column burdens in the lower troposphere increase by as much as 6%. ECHAM5-HAM is found to respond to this perturbation by calculating substantially higher CDNC (almost 10% for experiment **Bsc**), but the resulting changes in cloud macrophysical properties are not as pronounced.

Mid-Indian Ocean

Results of sampling the region of the mid-Indian Ocean shipping corridor in an Eulerian-type fashion are shown in Figs. 4.8, 4.9 and 4.10. Similar to the results from analysing the mid-Atlantic shipping corridor (Ch. 4.3), the SO_2 total column burden is generally enhanced across the whole shipping corridor and the relative change distinctly increases approximately at the location of the shipping lane. Due to fewer emissions in the mid-Indian Ocean compared to the mid-Atlantic Ocean (see Fig. 4.3), the relative change in SO_2 total column burden over the mid-Indian Ocean is less than half of that over the mid-Atlantic Ocean ($\approx 8\%$ vs. $\approx 20\%$), though. However, the corresponding increase in sulfate column burdens does not indicate such large differences ($\approx 6\%$ vs. $\approx 8\%$ for the total column; $\approx 7\%$ vs. $\approx 10\%$ for the lower troposphere). As expected, experiment **A** shows consistently

smaller changes in sulphuric compound column burdens compared to experiment **Bsc**. Compared to the other two shipping corridors (Chs. 4.3 and 4.3), the relative changes in BC column burden of the lower troposphere are larger in the mid-Indian Ocean. Additionally, particle number burdens of the insoluble Aitken mode (KI) increase by 350% - 600% in experiment **A**, a value at least one magnitude larger than those obtained for the other two regions (not shown). Because this region is the one farthest away from landmasses, these results confirm this regions' pristine state with respect to anthropogenic emissions.

Similar as for the change in CCN column burdens of the lower troposphere in the other two regions, the results show an overall increase in both experiments at all supersaturations which is also more pronounced in experiment **Bsc**. Also, the across-corridor gradients indicate distinctly more positive relative increases in the polluted parts of the corridor with the highest ones calculated for CCN(0.02%). It is therefore in this region only (of the three analysed regions), where lower tropospheric CCN column burdens are consistently increased in all experiments and across the whole considered spectrum of S .

Very similar to the results for the SE-Pacific- and mid-Atlantic Ocean regions, marked changes in both the total AOD and its FMF are visible at the location of the shipping lane. However, distinct changes in cloud micro- and macrophysical properties are not apparent. For experiment **A**, CDNC even decreases in the polluted part of the shipping corridor and the changes in other cloud properties also do not indicate a modification according to AIE-hypotheses. For experiment **Bsc** however, the changes in cloud properties are more similar to the ones obtained for the other regions: cloud properties change according to AIE-principles across the whole breadth of the shipping corridor. The results obtained for the TOA radiative properties also confirm this, *i.e.* in the shortwave part of the spectrum, the values are more negative almost throughout the breadth of the corridor for experiment **Bsc** compared to **A**.

Summarising the results obtained for the mid-Indian Ocean shipping corridor, an overall increase in aerosol species column burdens which exhibit distinct increases at the location of the shipping lane is found. This results in distinct increases of CCN column burdens in across-corridor direction, but similar to the results obtained for the other two shipping corridors, clouds change in accordance with AIE-hypotheses across the whole breadth of the corridor, *i.e.* they do not exhibit pronounced changes at the location of the shipping lane. This is especially true for experiment **Bsc**, the models' response as obtained from experiment **A** shows much more across-corridor variability.

4.4 Summary and Conclusions

To further quantify the effect of shipping emissions on clouds as computed by the aerosol climate model ECHAM5-HAM (see Ch. 3) and to bridge the gap to the satellite data analysis, the Eulerian sampling strategy as illustrated in Ch. 2.4.1 was applied to the modelling results. Additionally to the cloud- and aerosol parameters that were studied in the satellite data analysis, possible changes in atmospheric composition in the shipping corridors were also investigated. This analysis strategy has two main advantages compared to the satellite data analysis: (1) the results can be compared to a “base-case” and (2), data concerning changes in atmospheric composition which may lead to AIEs can also be investigated.

Generally, an across-corridor increase in atmospheric column burdens of sulphuric compounds (SO_2 and sulfate) is found in all three shipping corridors. For the ones in the mid-Atlantic- and mid-Indian Oceans, there even is a very pronounced increase in SO_2 column burden at the location of the shipping lane. The relative change in the mid-Atlantic- is about twice as high as in the mid-Indian Ocean shipping corridor. Resulting from the general increase in sulphuric-compound mass in the atmosphere due to shipping emissions, an increase in CCN burdens (integrated from the surface to 680 hPa) across the entire breadth of the shipping corridors was found for every experiment. Especially the results from the experiments in which the modified emission parametrisation was used often indicate a distinct increase in CCN column burdens at the point of the shipping lane.

Despite the apparent increase in CCN column burdens in the lower troposphere, the sampled cloud micro-physical properties only partly show the expected response: in one region (mid-Atlantic), CDNC is subject to a marked increase at the location of the shipping lane. For the other regions, micro-physical cloud properties are modified for the entire environment of the shipping corridor rather than just at the location of the shipping lane. The same holds for the computed cloud macrophysical properties. Thus, it is the enhancement of CCN-numbers in the entire lower troposphere in vicinity of the shipping corridor which appears relevant rather than the often distinct change at the shipping lane.

But one must bear in mind that the cloud properties as sampled from the model fields exhibit similarly strong gradients in across corridor direction as those obtained from the satellite data analysis. However, the sign of the gradient is rarely identical among satellite- and model data; a result which is not too surprising when one considers the substantial difficulties of GCMs to correctly capture the distribution of low clouds (e.g. Bony and Dufresne, 2005; Gehlot, 2010; Nam, 2011). As the maximum changes in CCN column burdens are on the order of $\approx 5\%$ and the cloud response to this is most probably non-linear, it may also be highly unlikely to detect the corresponding change in cloud micro- and macrophysical properties as

calculated from a double-moment cloud scheme as employed in ECHAM5-HAM.

So in a sense, the sampling of the model results confirms the results from the satellite data: the environment in which the sampling approach is utilised does not allow for a sound separation of dynamical- from micro-physical effects. The model results also suggest that the clouds sampled in the satellite data analysis may very well have been influenced by shipping emissions; this effect is however spread out across the whole shipping corridor which again hampers the quantification by satellite data alone.

SUMMARY, IMPLICATIONS AND OUTLOOK

The alteration of micro- and macrophysical properties of clouds due to the emissions of aerosols and aerosol precursor gases from anthropogenic activities (“aerosol indirect effects”, AIEs) has been a topic of intense research in the past decades and will continue to be so for the next decades to come. In general, this alteration of cloud properties increases the reflectivity of the clouds, thereby reducing the amount of energy absorbed by the Earth System and a net cooling effect is exerted on the Earth System. It is exactly this effect on atmospheric radiation that attracts the attention of both the scientific community and a broader public because it partly masks the global warming induced by the anthropogenic emission of long-lived greenhouse gases, such as carbon dioxide and methane. But despite intense fundamental research activities in the past decades, AIEs are subject to the largest uncertainties of all climate forcing components when it comes to quantifying human induced climate change (Forster et al., 2007).

The scope of this thesis was to reduce the uncertainties associated with AIEs by systematically investigating AIEs from shipping emissions on climatically relevant scales. To do so, both observational data and results from general circulation model (GCM) simulations were used.

5.1 Summary

Satellite data analysis

To investigate the impact of shipping emissions on clouds on climatically relevant scales beyond that of an individual “ship-track”, a combination of satellite- and re-analysis data was used to sample parameters characterising the cloud-, aerosol- and radiative properties as well as the large-scale meteorological environment of several remote oceanic regions. These regions were chosen in such a way that a clear separation of “clean” from “polluted” areas, with respect to shipping emissions,

could be achieved. Three regions were found suitable for analysis: 1) the SE-Pacific Ocean with the shipping lane from the Panama Canal southwestward, 2) the mid-Atlantic Ocean with the shipping lane from Europe to South America and 3) the mid-Indian Ocean with the shipping lane from Madagascar to Indonesia.

The statistical analysis covered the years 2005 – 2007 and the main findings are as follows:

- The statistical analysis of cloud-, aerosol- and radiative properties in the selected oceanic regions did not reveal sound evidence of climatically relevant AIEs from shipping emissions.
- Relating the observed aerosol- to the observed microphysical cloud property changes provides observational evidence for a “Twomey-effect” in some regions. However, the observed changes in macrophysical cloud properties, which have a larger impact on atmospheric radiation, are better explained by changes in the ambient meteorological conditions than by any other concept of secondary AIEs.
- The highly convective nature of the sampled environments may have such a large influence on the cloud fields that the signal-to-noise ratio stemming from any micro-physical perturbation due to shipping emissions is very small.

Global modelling of ship-induced AIEs

The quantification of the total global impact of shipping emissions on clouds still remains an open issue and only very few estimates from global climate modelling exist. Basically, two key uncertainties, associated with correctly representing shipping emissions of aerosols- and aerosol precursor gases in global models, have to be accounted for. Firstly, the actual global total amount of fuel burnt by sea-going ships is poorly constrained and secondly, assumptions about the size distribution of the emitted particles are not always consistent with observations.

In this thesis, an up-to-date shipping emission inventory, representing emission-estimates for the year 2000, is implemented in the ECHAM5-HAM GCM which includes an interactive treatment of the global aerosol system and its interactions with cloud micro- and macro-physics. A series of experiments was designed to address the aforementioned uncertainties within the range of published values. Furthermore, simulations to test the importance of carbonaceous emissions from ships with respect to AIEs were also performed. All simulations covered the time period of 2000 – 2005 (plus a three-month spin-up period) and were nudged to ERA-Interim re-analysis data. Key findings of the performed experiments are as follows:

- The upper estimate of the globally averaged AIE from shipping emissions of the year 2000 is $-0.32 \pm 0.01 \text{ Wm}^{-2}$, which is about half of the previous upper estimate (-0.6 Wm^{-2} , Lauer et al., 2007).
- Uncertainties associated with the size distribution of emitted particles have much larger implications for the AIE than the total amount of the emissions themselves.
- Omitting the emission of carbonaceous compounds from ships proved not to have a substantial impact on the resulting globally averaged AIE from shipping emissions.
- Application of a Student’s t-test showed areas of significant changes in aerosol as well as micro- and macrophysical cloud properties. However, the obtained AIE patterns show no coherent areas of significance which may indicate compensating effects among the cloud-property changes related to atmospheric radiation.

Sampling the model like the satellite data

For a more complete quantification of a system’s response to an external forcing, the combination of results obtained from both observations and modelling is necessary. In the framework of this thesis, the sampling approach used for the statistical analysis of satellite data is thus applied to the results obtained from the sensitivity studies with ECHAM5-HAM. Apart from investigating the resulting impact on aerosol- and cloud properties, sampling of model data also allows insights into the underlying processes. The sampling was applied to all three regions mentioned above.

The key findings of this analysis approach are as follows:

- The results from sampling the model data confirm those obtained from the satellite data analysis, *i.e.* cloud properties do not show distinct changes near the locations where shipping emissions are applied in the model. However, cloud fields exhibit large-scale modifications which are in-line with AIE-hypotheses.
- Aerosols and aerosol precursor gases relevant for the production of cloud condensation nuclei (CCNs) often do change substantially at the location of applied shipping emissions.
- In the regions chosen for analysis, it is the overall increase in CCN which has an effect on cloud properties rather than the distinct additional increases at the point of emission.

5.2 Implications

The results presented in this thesis show that the AIE from shipping emissions may be less negative than previously anticipated. Considering the fact that estimates of the globally averaged AIEs have tended to get more, rather than less, negative in the past decades, these results shed new light on the discussion about climate sensitivity. As Andreae et al. (2005) have nicely illustrated, a strong cooling of the Earth System due to the whole suite of aerosol effects implies a large climate sensitivity (*i.e.* the equilibrium response change in surface temperature resulting from a doubling of atmospheric CO₂ concentrations). Thus, a reduction of aerosol emissions as it is assumed for the future decades will lead to even faster surface temperature changes than in the past.

But as the results of this thesis show, the globally averaged AIE may actually not be as large as anticipated, and although the AIE is still estimated to be relatively large, its signature cannot be extracted from observations. This in turn implies a lower climate sensitivity and thus an Earth System which is less sensitive to external forcings.

Furthermore, applying statistics to the results obtained from the global aerosol climate model show that although the spatial patterns of the AIE are well in line with expectations, they are still not statistically significant at the 10% level. However, a critical assessment of whether spatial significance should be accounted for when deriving globally averaged AIE-values is beyond the scope of this thesis.

Additionally to the implications for estimating climate sensitivity, the results presented in this thesis also give insight into AIE-mechanisms at the process-level, *e.g.* that perturbations of the tropical marine boundary layer composition are easily compensated for by the highly variable cloud properties in that environment.

5.3 Outlook

The findings presented in this thesis clearly show the need for ever more sophisticated approaches to increase the level of scientific understanding of AIEs. From the perspective of observational efforts, one of the key challenges is to control for as much of the large-scale environment as possible so that sound cause-and-effect relationships between changes in aerosol and cloud properties can be established. Dedicated field campaigns to investigate the response of cloud ensembles to controlled perturbations, *e.g.* in the highly dynamic regimes investigated in this thesis, could provide very useful insights into a possible climatic effect. Concerning the understanding at the process-level, ship-tracks continue to provide new insights into possible responses of cloud fields to external perturbations (*e.g.* Christensen and Stephens, 2011) and fostering the interest of the scientific community in these

features will surely provide compelling results.

Concerning the quantification of AIEs from observations in general, recent studies highlighted the importance choosing the correct scale which the data are analysed at. For example Grandey and Stier (2010) found that spurious statistical relationships between aerosol and cloud properties obtained from satellite data arise when they increased the averaging domain. Along those same lines, McComiskey and Feingold (2011) highlight the importance of choosing the analysis scale to be on the same order of the process scale, *e.g.* relating instantaneous aerosol and cloud properties of the same atmospheric column to each other rather than aggregating the data over large spatial and temporal scales. At first, following these recommendations will surely be more tedious than applying the previous ones but the results will be more physically representative.

Regarding the modelling effort presented in this thesis, it would also be of high interest to perform simulations in which the shipping emissions are scaled to a much higher level than that shown in Ch. 3. From those simulations, the emission amount needed to obtain substantial changes in the shipping corridors investigated in Ch. 4 could be assessed. This would also give valuable insights into the magnitude of perturbation needed to substantially disturb clouds in highly dynamic regimes.

One could of course think of a number of sensitivity studies to further investigate the response of ECHAM5-HAM to shipping emissions, *e.g.* using different spatial distributions of shipping emissions (*e.g.* Wang et al., 2007), implementing a subgrid-plume model of shipping emissions (*e.g.* Franke et al., 2008) or quantifying the transient response by implementing the future sulphur-content reductions of marine bunker fuels (IMO, 1998). Past modelling efforts of AIEs from ships utilised either GCMs or cloud resolving models – bridging the gap between the two by performing simulations on regional scales is an endeavour worth pursuing. In fact, a recently started PhD project at the ETH Zürich will address exactly this approach (A. Possner, pers. comm. 2011). In the more general AIE-context, there already exist first attempts to disentangle the effects of aerosols on clouds and precipitation (*e.g.* Seifert et al., 2011).

The results presented in this thesis also call for a more critical assessment of globally averaged AIEs obtained from GCM simulations. With the ever increasing power of supercomputers, it has now become affordable to perform multi-year GCM-integrations with sophisticated online-treatment of the global aerosol system. Using these multi-year integrations can then serve as input for thorough statistical analysis to sort out the various interactions between aerosols and clouds as represented in the model.

Calls for a more critical assessment of modelled AIEs are provided by simple statistical tests applied to the results of the GCM simulations: changes in various

aerosol- and cloud properties show statistical significance whereas changes in the net top-of-atmosphere radiation do not. From this, two pathways worth pursuing emerge:

- 1) From a process-oriented perspective, the question to tackle is: What processes are compensating for the substantial changes in cloud properties so that they don't show up in the net radiation?
- 2) From a climate-oriented perspective, the question is the following: How much trust does one have in a global mean value obtained by averaging over values which are almost all statistically insignificant?¹

¹A preliminary analysis is supplied in Appendix B.

IMPLEMENTING THE NUDGING

Here, a detailed description of the nudging scheme as performed in the ECHAM5 model is given (S. Rast, pers. comm.). The nudging to observations is performed by applying Newtonian relaxation as described in Krishnamurti et al. (1991).

Let $X^{(m)}(t)$ be the value of a model parameter X as predicted for time t based on a state $X^{(m)}(0)$ and $X(t)$ be an observed value of that parameter at time t . Then the difference between the modelled and the observed state is

$$\Delta X_t := X^{(m)}(t) - X(t). \quad (\text{A.1})$$

In the nudging procedure, a differential equation that yields an exponential decay of this difference with time t is used. The relaxation time τ describes how fast the exponential decay is:

$$\frac{d}{dt} \Delta X_t = -\frac{1}{\tau} \Delta X_t. \quad (\text{A.2})$$

Integration and evaluation of the limiting behaviour yields

$$\begin{aligned} \Delta X_t &= e^{-\frac{1}{\tau}t} \Delta X_0 \\ \lim_{t \rightarrow \infty} \Delta X_t &= 0, \end{aligned} \quad (\text{A.3})$$

an important result which has to be considered for correct numerical implementation.

Implicit Euler method

Numerically, (A.2) is solved by using an implicit Euler method:

$$\frac{d}{dt} \Delta X_t = \frac{\Delta X_t(t + \Delta t) - \Delta X_t(t)}{\Delta t} = -\frac{1}{\tau} \Delta X_t(t + \Delta t). \quad (\text{A.4})$$

Reordering yields

$$\begin{aligned} \Delta X_t(t + \Delta t) + \frac{\Delta t}{\tau} \Delta X_t(t + \Delta t) &= \Delta X_t(t) \\ \Delta X_t(t + \Delta t) \left(1 + \frac{\Delta t}{\tau} \right) &= \Delta X_t(t). \end{aligned} \quad (\text{A.5})$$

Substitution of (A.1) then results in

$$(X^{(m)}(t + \Delta t) - X(t + \Delta t)) \left(1 + \frac{\Delta t}{\tau} \right) = X^{(m)}(t) - X(t) \quad (\text{A.6})$$

$$\begin{aligned} X^{(m)}(t + \Delta t) &= \frac{X^{(m)}(t) - X(t)}{1 + \frac{\Delta t}{\tau}} + X(t + \Delta t) \\ X^{(m)}(t + \Delta t) &= \frac{1}{1 + \frac{\Delta t}{\tau}} \left(X^{(m)}(t) - X(t) + X(t + \Delta t) + \frac{\Delta t}{\tau} X(t + \Delta t) \right) \end{aligned} \quad (\text{A.7})$$

On the right hand side of (A.7), the approximation

$$X(t + \Delta t) - X(t) \approx \Delta \widetilde{X}^{(m)}(t) \quad (\text{A.8})$$

can be used. $\Delta \widetilde{X}^{(m)}(t)$ is the increment $\left(\widetilde{X}^{(m)}(t + \Delta t) - X^{(m)}(t) \right)$ as predicted by the model without nudging. This is valid because the change in observational data from time t to $t + \Delta t$ is assumed to be close to that of the model. Applying (A.8) to (A.7) thus gives

$$X^{(m)}(t + \Delta t) = \frac{1}{1 + \frac{\Delta t}{\tau}} \left(X^{(m)}(t) + \Delta \widetilde{X}^{(m)}(t) + \frac{\Delta t}{\tau} X(t + \Delta t) \right). \quad (\text{A.9})$$

The state of the parameter $X^{(m)}$ at time $t + \Delta t$ is thus given by the state of the model at time t , the tendency predicted by the model without nudging and the observational state at time $t + \Delta t$ which the model is relaxed to.

Observational data are typically stored every six hours and then spline-interpolated between their six-hourly output intervals. In the nudging procedure applied in the model, the nudging coefficients, *i.e.* the relaxation time τ , are dynamic. This means that the nudging continuously changes from being strongest at the time of an observation, *i.e.* every six hours, and weakest (*i.e.* infinite relaxation time τ) at the times farthest away from the actual observations, *i.e.* three hours before/after the observation time.

Evaluation of the limiting behaviour

It is important that the limiting behaviour of (A.2) described by (A.3) also holds for the numerical solution of (A.2). In fact, (A.3) holds for the implicit Euler method:

$$\begin{aligned} \lim_{\Delta t \rightarrow \infty} (X^{(m)}(t + \Delta t) - X(t + \Delta t)) &= \lim_{\Delta t \rightarrow \infty} \left(\frac{1}{1 + \frac{\Delta t}{\tau}} (X^{(m)}(t) - X(t)) \right) \\ &= 0. \end{aligned}$$

Using an explicit Euler method would give the following discretisation:

$$\frac{d}{dt} \Delta X_t = \frac{\Delta X_t(t + \Delta t) - \Delta X_t(t)}{\Delta t} = -\frac{1}{\tau} \Delta X_t(t). \quad (\text{A.10})$$

Reordering and substituting (A.1) yields

$$\begin{aligned} \Delta X_t(t + \Delta t) &= \Delta X_t(t) - \frac{\Delta t}{\tau} \Delta X_t(t) \\ X^{(m)}(t + \Delta t) - X(t + \Delta t) &= \left(1 - \frac{\Delta t}{\tau} \right) (X^{(m)}(t) - X(t)). \end{aligned} \quad (\text{A.11})$$

Evaluation of the limiting behaviour of (A.11) yields

$$\begin{aligned} \lim_{\Delta t \rightarrow \infty} (X^{(m)}(t + \Delta t) - X(t + \Delta t)) &= \lim_{\Delta t \rightarrow \infty} \left[\left(1 - \frac{\Delta t}{\tau} \right) (X^{(m)}(t) - X(t)) \right] \\ &= \pm \infty. \end{aligned}$$

Thus applying an explicit Euler method to the nudging routine leads to wrong limiting behaviour.

CONDITIONAL VS. UNCONDITIONAL SAMPLING OF THE AIE

Intrigued by question 2), a short preliminary assessment of the globally averaged AIE is performed by conditionally sampling the model output fields. The general approach for conditionally sampling the AIE as obtained from experiment **B** (see Ch. 3.2.5) is to mask the global AIE field with the significance patterns calculated for the changes in sulfate column burden (SO_4), aerosol optical depth (AOD), AOD fine mode (FM), cloud droplet number concentration at cloud top (CDNC) and the aerosol indirect effect (AIE) itself. For computing the global average from these masked fields, all regions showing no significance are assumed zero. Furthermore, data modifications which could increase the areas of statistical significance are also employed. In a first step, the original model output data (T63-resolution) is remapped to lower model resolution (*i.e.* T42, T31 and T21) and in a second step, the original and remapped model data are “smoothed” by computing a weighted area average for the centre-pixel of a 3×3 -pixel model domain. These two approaches are designed to retain the overall global average but the spatial inhomogeneity is reduced, thereby enhancing the signal-to-noise ratio. The results of applying this conditional sampling are shown in Fig. B.

As expected from the results shown in Ch. 3.2.5, the area used for computing the globally averaged AIE from just those areas with significant changes is totally negligible. At the original T63 resolution, masking the AIE-data according to the significance of AOD fine-mode changes gives the largest area-fraction ($\approx 7\%$), closely followed by that obtained when masking with the significance pattern of CDNC changes ($\approx 6\%$). This result is also as expected, because the shipping emissions lead to substantially increased aerosol particle numbers in the soluble Accumulation mode (AS). The response of the cloud micro-physics parametrisation includes increased cloud droplet nucleation rates (see Eq. 3.2). Masking by significant changes in the sulfate column burden leads to a slightly smaller averag-

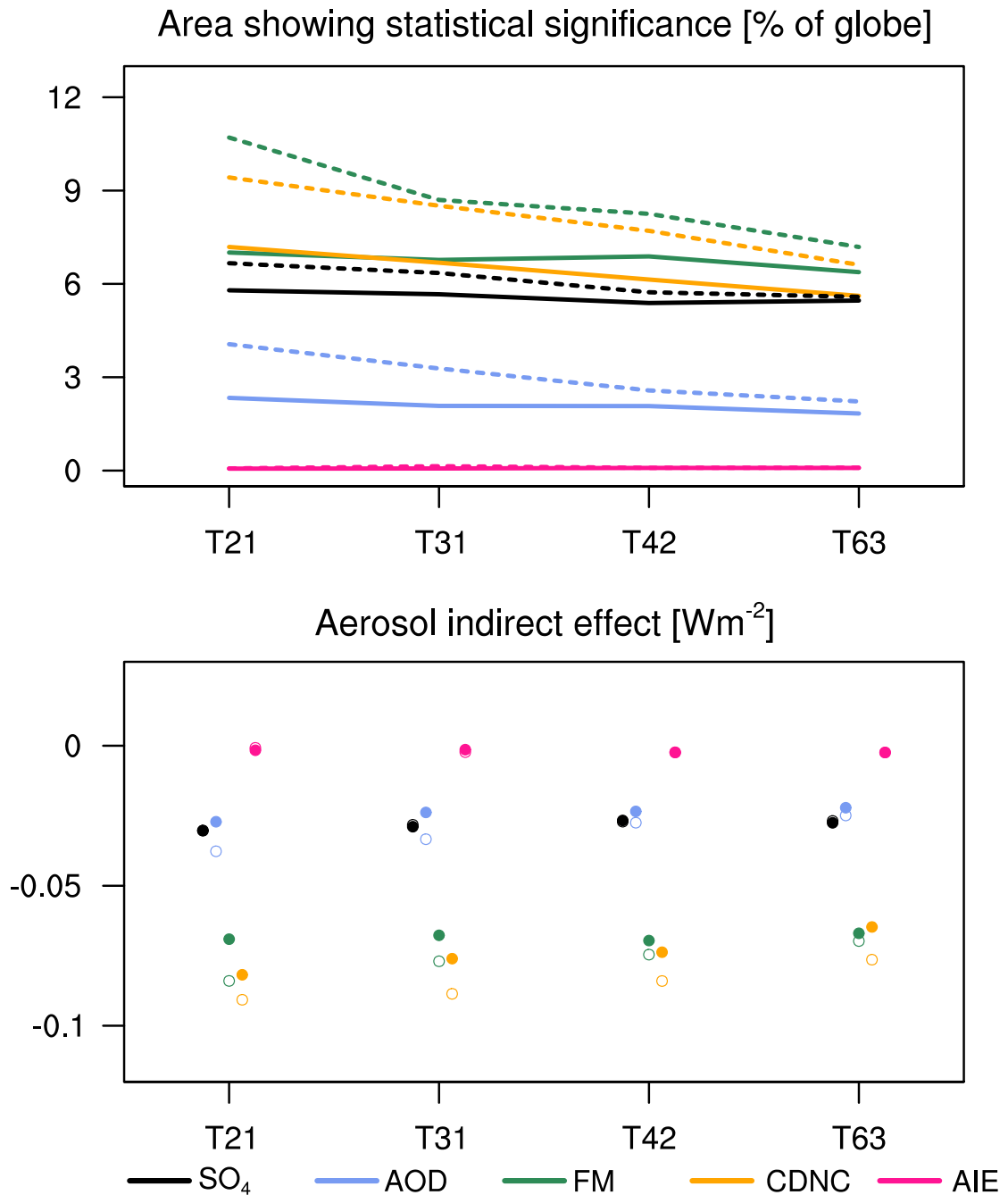


Figure B.1: Globally averaged AIE from shipping emissions (**bottom panel**) and percentage of global area used for obtaining the AIE (**top panel**) in experiment **B**. Results are shown for (i) averaging over regions where changes of certain parameters show statistical significance (*i.e.* sulfate column burden (SO₄), aerosol optical depth (AOD), AOD fine mode (FM), cloud droplet number concentration at cloud top (CDNC) and aerosol indirect effect (AIE); indicated by colour coding), (ii) remapping the original T63 model output to lower resolutions (T21, T31, T42; x-axis) and (iii) applying a 9-point smoothing to the original and remapped model fields (original: filled circles, solid lines; smoothed: open circles, dashed lines).

ing domain compared to CDNC, and masking by total AOD yields less than half of the area compared to the other approaches.

The impact of reducing the spatial inhomogeneity of the model output fields by both remapping and smoothing is indeed substantial. For all masking approaches, except the one which utilises the AIE-significance, the area of significant changes increases with decreasing resolution. In principal, the effects shown here were also found by McComiskey and Feingold (2011) when they mapped the output of a cloud resolving model to coarser resolutions. Here, the area is further increased, also for the original T63 resolution, when the output fields undergo a spatial smoothing. Here, the maximum global fraction of significant areas results from using the mask obtained from the smoothed T21-fields of significant changes in the AOD fine mode ($\approx 11\%$). So in the end, using the results from this analysis would reduce the area used for obtaining the globally averaged AIE by at least $\approx 90\%$ and it is questionable whether the resulting AIE is still on the order of the one obtained from unconditional averaging (*i.e.* $-0.23 \pm 0.008 \text{ Wm}^{-2}$).

From the results shown in the bottom panel of Fig. B, it immediately becomes apparent that the AIE resulting from conditional sampling does not amount to even half the value obtained from unconditional sampling. At the original T63 resolution, the lowest globally averaged AIE amounts to -0.076 Wm^{-2} for sampling according to the significant changes in CDNC obtained from the smoothed output fields; sampling according to AOD fine-mode significance yields a slightly more positive AIE. Interestingly, the AIE is not maximised when sampling the regions of significant changes in the AOD fine mode, although these represent a larger fraction of the global area. It is instead those areas with the most pronounced changes in cloud top properties which result in a more negative AIE although covering less area. Averaging over regions of significant changes in total AOD or sulfate column burden gives an AIE on the order of -0.025 Wm^{-2} . When sampling according to significant changes in AIE, the global average is nearly zero.

Remapping of the model output data results in a slightly more negative AIE for all sampling approaches when using the original, unsmoothed model data. When the remapping is applied to the smoothed model output data fields, the obtained AIE values are consistently lower than the ones obtained from the unsmoothed fields and the difference between the two gets larger with decreasing resolution. This is especially apparent for sampling according to significant changes in total AOD and AOD fine mode. These features are not derived for the AIE values derived from sampling the data according to significant changes in sulfate column burden and AIE. The most negative AIE-value is thus obtained if the averaging would be performed over areas of significant changes in CDNC of the smoothed T21-data. Then the globally averaged AIE would amount to -0.09 Wm^{-2} .

Of course, this analysis represents just very preliminary and pre-mature results.

A more detailed assessment of the issues related to globally averaging the regionally confined AIE should thus be a topic of future fundamental research.

BIBLIOGRAPHY

- Abdul-Razzak, H. and Ghan, S. (2000). A parameterization of aerosol activation 2. multiple aerosol types. *J. Geophys. Res.*, 105(D5):6837–6844.
- Abdul-Razzak, H., Ghan, S., and Rivera-Carpio, C. (1998). A parameterization of aerosol activation 1. single aerosol type. *J. Geophys. Res.*, 103(D6):6123–6131.
- Agrawal, H., Malloy, Q., Welch, W., Wayne Miller, J., and Cocker III, D. (2008). In-use gaseous and particulate matter emissions from a modern ocean going container vessel. *Atmos. Env.*, 42(21):5504–5510.
- Albrecht, B. A. (1989). Aerosols, Cloud Microphysics, and Fractional Cloudiness. *Science*, 245:1227 – 1230.
- Andreae, M., Jones, C., and Cox, P. (2005). Strong present-day aerosol cooling implies a hot future. *Nature*, 435(7046):1187–1190.
- Andreae, M. O. (2009). Correlation between cloud condensation nuclei concentration and aerosol optical thickness in remote and polluted regions. *Atmos. Chem. Phys.*, 9(2):543–556.
- Ångström, A. (1962). Atmospheric turbidity, global illumination and planetary albedo of the earth. *Tellus*, 14(4):435–450.
- Behrens, H. L. (2006). Present traffic and emissions from maritime shipping. In *Deliverable D1.1.2.2 of the EU-IP QUANTIFY (confidential)*. Det Norske Veritas.
- Bellouin, N., Jones, A., Haywood, J., and Christopher, S. A. (2008). Updated estimate of aerosol direct radiative forcing from satellite observations and comparison against the Hadley Centre climate model. *J. Geophys. Res.-Atmos.*, 113:D10205.
- Betts, A. and Ridgway, W. (1989). Climatic equilibrium of the atmospheric convective boundary layer over a tropical ocean. *J. Atmos. Sci.*, 46(17):2621–2641.

- Bodas-Salcedo, A., Webb, M., Bony, S., Chepfer, H., Dufresne, J., Klein, S., Zhang, Y., Marchand, R., Haynes, J., Pincus, R., et al. (2011). COSP: Satellite simulation software for model assessment. *Bull. Am. Meteorol. Soc.*, 92:1023 – 1043.
- Bond, T. (2007). Can warming particles enter global climate discussions? *Environ. Res. Lett.*, 2:045030.
- Bond, T., Streets, D., Yarber, K., Nelson, S., Woo, J., and Klimont, Z. (2004). A technology-based global inventory of black and organic carbon emissions from combustion. *J. Geophys. Res.*, 109(D14):D14203.
- Bond, T. and Sun, H. (2005). Can reducing black carbon emissions counteract global warming? *Environ. Sci. Technol.*, 39(16):5921–5926.
- Bony, S. and Dufresne, J. (2005). Marine boundary layer clouds at the heart of tropical cloud feedback uncertainties in climate models. *Geophys. Res. Lett.*, 32(20):L20806.
- Brinkop, S. and Roeckner, E. (1995). Sensitivity of a general circulation model to parameterizations of cloud–turbulence interactions in the atmospheric boundary layer. *Tellus A*, 47(2):197–220.
- Cancún (2010). The United Nations Climate Change Conference in Cancún, COP 16 / CMP 6.
- Capaldo, K., Corbett, J., Kasibhatla, P., Fischbeck, P., and Pandis, S. (1999). Effects of ship emissions on sulphur cycling and radiative climate forcing over the ocean. *Nature*, 400(6746):743–746.
- Chen, W., Lee, Y., Adams, P., Nenes, A., and Seinfeld, J. (2010). Will black carbon mitigation dampen aerosol indirect forcing ? *Geophys. Res. Lett.*, 37(5).
- Christensen, M. and Stephens, G. (2011). Microphysical and macrophysical responses of marine stratocumulus polluted by underlying ships: Evidence of cloud deepening. *J. Geophys. Res.-Atmos.*, 116(D3):D03201.
- Coakley, J., Bernstein, R., and Durkee, P. (1987). Effect of Ship-Stack Effluents on Cloud Reflectivity. *Science*, 237(4818):1020–1022.
- Conover, J. (1966). Anomalous Cloud Lines. *J. Atmos. Sci.*, 23:778–785.
- Corbett, J., Fischbeck, P., and Pandis, S. (1999). Global nitrogen and sulfur inventories for oceangoing ships. *J. Geophys. Res.*, 104(D3):3457–3470.
- Corbett, J. and Koehler, H. (2003). Updated emissions from ocean shipping. *J. Geophys. Res.*, 108(D20):4650–64.

- Corbett, J. and Koehler, H. (2004). Considering alternative input parameters in an activity-based ship fuel consumption and emissions model: Reply to comment by Øyvind Endresen et al. on Updated emissions from ocean shipping. *J. Geophys. Res.*, 109(D23):D23303.
- Dalsøren, S., Eide, M., Endresen, Ø., Mjelde, A., Gravir, G., and Isaksen, I. (2009). Update on emissions and environmental impacts from the international fleet of ships: the contribution from major ship types and ports. *Atmos. Chem. Phys.*, 9:2171–2194.
- Dentener, F., Kinne, S., Bond, T., Boucher, O., Cofala, J., Generoso, S., Ginoux, P., Gong, S., Hoelzemann, J. J., Ito, A., Marelli, L., Penner, J. E., Putaud, J.-P., Textor, C., Schulz, M., van der Werf, G. R., and Wilson, J. (2006). Emissions of primary aerosol and precursor gases in the years 2000 and 1750 prescribed data-sets for aerocom. *Atmos. Chem. Phys.*, 6(12):4321–4344.
- Devasthale, A., Krüger, O., and Grassl, H. (2005). Change in Cloud-Top Temperatures Over Europe. *IEEE Geosci. Remote S.*, 2(3):333–336.
- Devasthale, A., Krüger, O., and Grassl, H. (2006). Impact of ship emissions on cloud properties over coastal areas. *Geophys. Res. Lett.*, 33(2).
- Dusek, U., Frank, G., Hildebrandt, L., Curtius, J., Schneider, J., Walter, S., Chand, D., Drewnick, F., Hings, S., Jung, D., et al. (2006). Size matters more than chemistry for cloud-nucleating ability of aerosol particles. *Science*, 312(5778):1375–1378.
- Endresen, Ø., Sørsgård, E., Bakke, J., and Isaksen, I. (2004). Substantiation of a lower estimate for the bunker inventory: Comment on Updated emissions from ocean shipping by James J. Corbett and Horst W. Koehler. *J. Geophys. Res.*, 109(D23):D23302.
- Endresen, Ø., Sørsgård, E., Behrens, H., Brett, P., and Isaksen, I. (2007). A historical reconstruction of ships' fuel consumption and emissions. *J. Geophys. Res.*, 112(D12).
- Endresen, Ø., Sørsgård, E., Sundet, J., Dalsøren, S., Isaksen, I., Berglen, T., and Gravir, G. (2003). Emission from international sea transportation and environmental impact. *J. Geophys. Res.*, 108(D17):4560.
- Eyring, V., Isaksen, I. S. A., Berntsen, T., Collins, W. J., Corbett, J. J., Endresen, O., Grainger, R. G., Moldanova, J., Schlager, H., and Stevenson, D. S. (2010). Transport impacts on atmosphere and climate: Shipping. *Atmos. Environ.*, 44(37, Sp. Iss. SI):4735–4771.

- Eyring, V., Köhler, H., Lauer, A., and Lemper, B. (2005a). Emissions from international shipping: 2. impact of future technologies on scenarios until 2050. *J. Geophys. Res.*, 110(D17):D17306.
- Eyring, V., Köhler, H., Van Aardenne, J., and Lauer, A. (2005b). Emissions from international shipping: 1. The last 50 years. *J. Geophys. Res.*, 110(D17):D17305.
- Eyring, V., Stevenson, D. S., Lauer, A., Dentener, F. J., Butler, T., Collins, W. J., Ellingsen, K., Gauss, M., Hauglustaine, D. A., Isaksen, I. S. A., Lawrence, M. G., Richter, A., Rodriguez, J. M., Sanderson, M., Strahan, S. E., Sudo, K., Szopa, S., van Noije, T. P. C., and Wild, O. (2007). Multi-model simulations of the impact of international shipping on atmospheric chemistry and climate in 2000 and 2030. *Atmos. Chem. Phys.*, 7(3):757–780.
- Feichter, J., Kjellström, E., Rodhe, H., Dentener, F., Lelieveld, J., and Roelofs, G. (1996). Simulation of the tropospheric sulfur cycle in a global climate model. *Atmos. Env.*, 30(10-11):1693–1707.
- Forster, P., Ramaswamy, V., Artaxo, P., Berntsen, T., Betts, R., Fahey, D. W., Haywood, J., Lean, J., Lowe, D. C., Myhre, G., Nganga, J., Prinn, R., Raga, G., Schulz, M., and Van Dorland, R. (2007). Changes in Atmospheric Constituents and in Radiative Forcing. In Solomon, S., Qin, D., Manning, M., Chen, Z., Marquis, M., Averyt, K. B., Tignor, M., and Miller, H. L., editors, *Climate Change 2007: The Physical Science Basis. Contribution of Working Group I to the Fourth Assessment Report of the Intergovernmental Panel on Climate Change*. Cambridge University Press, Cambridge, United Kingdom and New York, NY, USA.
- Fouquart, Y. and Bonnel, B. (1980). Computations of solar heating of the earth’s atmosphere- a new parameterization. *Beitr. Phys. Atmos.*, 53:35–62.
- Franke, K., Eyring, V., Sander, R., Hendricks, J., Lauer, A., and Sausen, R. (2008). Toward effective emissions of ships in global models. *Meteorol. Z.*, 17(2):117–129.
- Fuglestvedt, J., Berntsen, T., Eyring, V., Isaksen, I., Lee, D. S., and Sausen, R. (2009). Shipping emissions: From cooling to warming of climate – and reducing impacts on health. *Environ. Sci. Technol.*, 43(24):9057–9062.
- Gehlot, S. (2010). Feedbacks between convection and climate: analysis with global modelling and satellite observations. In *Berichte zur Erdsystemforschung*, number 81, 120pp., ISSN: 1614-1199. Max-Planck-Institut für Meteorologie.
- Grandey, B. S. and Stier, P. (2010). A critical look at spatial scale choices in satellite-based aerosol indirect effect studies. *Atmos. Chem. Phys.*, 10(23):11459–11470.

- Guelle, W., Schulz, M., Balkanski, Y., and Dentener, F. (2001). Influence of the source formulation on modeling the atmospheric global distribution of sea salt aerosol. *J. Geophys. Res.*, 106(D21):27509–27.
- Hayes, C., Coakley Jr, J., and Tahnk, W. (2010). Relationships among properties of marine stratocumulus derived from collocated calipso and modis observations. *J. Geophys. Res.*, 115:D00H17.
- Haywood, J. and Boucher, O. (2000). Estimates of the direct and indirect radiative forcing due to tropospheric aerosols: A review. *Rev. Geophys.*, 38(4):513 – 543.
- Hegg, D. A., Covert, D. S., Jonsson, H. H., and Woods, R. (2009). Differentiating natural and anthropogenic cloud condensation nuclei in the california coastal zone. *Tellus B*, 61(4):669–676.
- Hewson, E. (1943). The reflection, absorption, and transmission of solar radiation by fog and cloud. *Q. J. Roy. Meteor. Soc.*, 69(298):47–62.
- Hoose, C., Lohmann, U., Stier, P., Verheggen, B., and Weingartner, E. (2008). Aerosol processing in mixed-phase clouds in ECHAM5-HAM: Model description and comparison to observations. *J. Gephys. Res.*, 113(D7):D07210.
- Horowitz, L., Walters, S., Mauzerall, D., Emmons, L., Rasch, P., Granier, C., Tie, X., Lamarque, J., Schultz, M., Tyndall, G., et al. (2003). A global simulation of tropospheric ozone and related tracers: Description and evaluation of mozart, version 2. *J. Geophys. Res*, 108(D24):4784.
- Hudson, J., Noble, S., and Jha, V. (2010). Stratus cloud supersaturations. *Geophys. Res. Lett.*, 37(21):L21813.
- IMO (1998). Regulations for the prevention of air pollution from ships and NO_x technical code, ANNEX IV of MARPOL 73/78. Technical report, London.
- IPCC (1990). *IPCC First Assessment Report 1990 (FAR)*. Cambridge University Press, Cambridge, United Kingdom, and New York, NY, USA.
- IPCC (1995). *IPCC Second Assessment Report: Climate Change 1995 (SAR)*. Cambridge University Press, Cambridge, United Kingdom, and New York, NY, USA.
- IPCC (2001). *IPCC Third Assessment Report: Climate Change 2001 (TAR)*. Cambridge University Press, Cambridge, United Kingdom, and New York, NY, USA.
- IPCC (2007). *IPCC Fourth Assessmet Report: Climate Change 2007 (FAR)*. Cambridge University Press, Cambridge, United Kingdom and New York, NY, USA.

- Jacobson, M. Strong radiative heating due to the mixing state of black carbon in atmospheric aerosols. *Nature*, 409:695 – 697.
- Jacobson, M. (2002). Control of fossil-fuel particulate black carbon and organic matter, possibly the most effective method of slowing global warming. *J. Geophys. Res.*, 107(D19):4410.
- Kaluza, P., Kölzsch, A., Gastner, M., and Blasius, B. (2010). The complex network of global cargo ship movements. *J. R. Soc. Interface*, 7(48):1093.
- Kazil, J. and Lovejoy, E. R. (2007). A semi-analytical method for calculating rates of new sulfate aerosol formation from the gas phase. *Atmos. Chem. Phys.*, 7(13):3447–3459.
- Kazil, J., Stier, P., Zhang, K., Quaas, J., Kinne, S., O’Donnell, D., Rast, S., Esch, M., Ferrachat, S., Lohmann, U., and Feichter, J. (2010). Aerosol nucleation and its role for clouds and Earth’s radiative forcing in the aerosol-climate model ECHAM5-HAM. *Atmos. Chem. Phys.*, 10(22):10733–10752.
- Kettle, A. and Andreae, M. (2000). Flux of dimethylsulfide from the oceans- a comparison of updated data sets and flux models. *J. Geophys. Res.*, 105(26):793–808.
- Khairoutdinov, M. and Kogan, Y. (2000). A new cloud physics parameterization in a large-eddy simulation model of marine stratocumulus. *Mon. Wea. Rev.*, 128(1):229–243.
- Kireeva, E., Popovicheva, O., Persiantseva, N., Timofeyev, M., and Shonija, N. (2010). Fractionation analysis of transport engine-generated soot particles with respect to hygroscopicity. *J. Atmos. Chem.*, pages 1–19.
- Klein, S. and Hartmann, D. (1993). The seasonal cycle of low stratiform clouds. *J. Climate*, 6(8):1587–1606.
- Koren, I., Kaufman, Y., Rosenfeld, D., Remer, L., and Rudich, Y. (2005). Aerosol invigoration and restructuring of Atlantic convective clouds. *Geophys. Res. Lett.*, 32.
- Kotarba, A. (2010). Estimation of fractional cloud cover for Moderate Resolution Imaging Spectroradiometer/Terra cloud mask classes with high-resolution over ocean ASTER observations. *J. Geophys. Res.-Atmos.*, 115(D22).
- Krishnamurti, T. N., Xue, J., Bedi, H. S., Ingles, K., and Oosterhof, D. (1991). Physical initialization for numerical weather prediction over the tropics. *Tellus B*, 43(4):53–81.

- Kulmala, M., Lehtinen, K. E. J., and Laaksonen, A. (2006). Cluster activation theory as an explanation of the linear dependence between formation rate of 3nm particles and sulphuric acid concentration. *Atmos. Chem. Phys.*, 6(3):787–793.
- Kyoto Protocol (1997). *Kyoto Protocol to the United Nations Framework Convention on Climate Change*. United Nations Publications: Geneva, Switzerland.
- Lack, D. A., Corbett, J. J., Onasch, T., Lerner, B., Massoli, P., Quinn, P. K., Bates, T. S., Covert, D. S., Coffman, D., Sierau, B., Herndon, S., Allan, J., Baynard, T., Lovejoy, E., Ravishankara, A. R., and Williams, E. (2009). Particulate emissions from commercial shipping: Chemical, physical, and optical properties. *J. Geophys. Res.-Atmos.*, 114.
- Lauer, A., Eyring, V., Corbett, J., Wang, C., and Winebrake, J. (2009). Assessment of Near-Future Policy Instruments for Oceangoing Shipping: Impact on Atmospheric Aerosol Burdens and the Earth’s Radiation Budget. *Environmental science & technology*, 43(15):5592–5598.
- Lauer, A., Eyring, V., Hendricks, J., Jöckel, P., and Lohmann, U. (2007). Global model simulations of the impact of ocean-going ships on aerosols, clouds, and the radiation budget. *Atmos. Chem. Phys.*, 7(19):5061–5079.
- Lin, H. and Leitch, W. (1997). Development of an in-cloud aerosol activation parameterization for climate modelling. In *Proceedings of the WMO Workshop on Measurement of Cloud Properties for Forecasts of Weather, Air Quality and Climate, Mexico City*, pages 328–335.
- Lin, S. and Rood, R. (1996). Multidimensional flux-form semi-lagrangian transport schemes. *Mon. Wea. Rev.*, 124(9):2046–2070.
- Loeb, N. G. and Manalo-Smith, N. (2005). Top-of-atmosphere direct radiative effect of aerosols over global oceans from merged CERES and MODIS observations. *J. Climate*, 18(17):3506 – 3526.
- Lohmann, U. and Feichter, J. (2005). Global indirect aerosol effects: a review. *Atmos. Chem. Phys.*, 5:715–737.
- Lohmann, U., Feichter, J., Chuang, C., and Penner, J. (1999). Prediction of the number of cloud droplets in the ECHAM GCM. 104(D8):9169–9198.
- Lohmann, U., Rotstayn, L., Storelvmo, T., Jones, A., Menon, S., Quaas, J., Ekman, A. M. L., Koch, D., and Ruedy, R. (2010). Total aerosol effect: radiative forcing or radiative flux perturbation? *Atmos. Chem. Phys.*, 10(7):3235–3246.

- Lohmann, U., Stier, P., Hoose, C., Ferrachat, S., Kloster, S., Roeckner, E., and Zhang, J. (2007). Cloud microphysics and aerosol indirect effects in the global climate model ECHAM5-HAM. *Atmos. Chem. Phys.*, 7(13):3425–3446.
- Ludewig, E. (2011). Modis cloud top height evaluation. Diploma Thesis, Meteorologisches Institut, Universität Hamburg, Hamburg, Germany.
- McComiskey, A. and Feingold, G. (2011). The scale problem in quantifying aerosol indirect effects. *Atmos. Chem. Phys. Disc.*, 11(9):26741–26789.
- McCormick, R. A. and Ludwig, J. H. (1967). Climate Modification by Atmospheric Aerosols. *Science*, 156(3780):1358 – 1359.
- Mlawer, E., Taubman, S., Brown, P., Iacono, M., and Clough, S. (1997). Radiative transfer for inhomogeneous atmospheres: RRTM, a validated correlated-k model for the longwave. *J. Geophys. Res.*, 102(D14):16663–16.
- Nakajima, T. and King, M. (1990). Determination of the Optical-Thickness and Effective Particle Radius of Clouds from Reflected Solar-Radiation Measurements .1. Theory. *J. Atmos. Sci.*, 47(15):1878–1893.
- Nam, C. C.-W. (2011). Using CALIPSO and CloudSat satellite retrievals to evaluate low-level cloud parameterizations in ECHAM5 for cloud-climate feedbacks implications. In *Berichte zur Erdsystemforschung*, number 88, 132pp., ISSN: 1614-1199. Max-Planck-Institut für Meteorologie.
- Olivier, J. G. J., Van Aardenne, J. A., Dentener, F. J., Pagliari, V., Ganzeveld, L. N., and Peters, J. A. H. W. (2005). Recent trends in global greenhouse gas emissions: regional trends 1970–2000 and spatial distribution of key sources in 2000. *Env. Sc.*, 2(2-3):81–99.
- Peters, K., Quaas, J., and Bellouin, N. (2011). Effects of absorbing aerosols in cloudy skies: a satellite study over the Atlantic Ocean. *Atmos. Chem. Phys.*, 11(4):1393–1404.
- Petty, G. W. (2006). *A First Course In Atmospheric Radiation, Second Edition*. Sundog Publishing.
- Petzold, A., Hasselbach, J., Lauer, P., Baumann, R., Franke, K., Gurk, C., Schlager, H., and Weingartner, E. (2008). Experimental studies on particle emissions from cruising ship, their characteristic properties, transformation and atmospheric lifetime in the marine boundary layer. *Atmos. Chem. Phys.*, 8(9):2387–2403.

- Pierce, J. R. and Adams, P. J. (2009). Uncertainty in global CCN concentrations from uncertain aerosol nucleation and primary emission rates. *Atmos. Chem. Phys.*, 9(4):1339–1356.
- Pierce, J. R., Chen, K., and Adams, P. J. (2007). Contribution of primary carbonaceous aerosol to cloud condensation nuclei: processes and uncertainties evaluated with a global aerosol microphysics model. *Atmos. Chem. Phys.*, 7(20):5447–5466.
- Platnick, S., King, M., Ackerman, S., Menzel, W., Baum, B., Riédi, J., and Frey, R. (2003). The MODIS cloud products: Algorithms and examples from Terra. *IEEE Trans. Geosci. Remote Sens.*, 41(2):459–473.
- Pruppacher, H. and Klett, J. (1997). *Microphysics of clouds and precipitation*, volume 18. Kluwer Academic Pub.
- Quaas, J., Boucher, O., and Lohmann, U. (2006). Constraining the total aerosol indirect effect in the LMDZ and ECHAM4 GCMs using MODIS satellite data. *Atmos. Chem. Phys.*, 6(4):947–955.
- Quaas, J., Stevens, B., Stier, P., and Lohmann, U. (2010). Interpreting the cloud cover – aerosol optical depth relationship found in satellite data using a general circulation model. *Atmos. Chem. Phys.*, 10(13):6129–6135.
- Remer, L., Kaufman, Y., Tanre, D., Mattoo, S., Chu, D., Martins, J., Li, R., Ichoku, C., Levy, R., Kleidman, R., Eck, T., Vermote, E., and Holben, B. (2005). The MODIS aerosol algorithm, products, and validation. *J. Atmos. Sci.*, 62(4):947–973.
- Remer, L. A., Kleidman, R. G., Levy, R. C., Kaufman, Y. J., Tanré, D., Mattoo, S., Martins, J. V., Ichoku, C., Koren, I., Yu, H. B., and Holben, B. N. (2008). Global aerosol climatology from the MODIS satellite sensors. *J. Geophys. Res.-Atmos.*, 113(D14):148 – 227.
- Roeckner, E., Bäuml, G., Bonaventura, L., Brokopf, R., Esch, M., Giorgetta, M., Hagemann, S., Kirchner, I., Kornblueh, L., Manzini, E., et al. (2003). The atmospheric general circulation model ECHAM5. Part I: Model description. *Max Planck Institute for Meteorology Rep.*, 349:127 pp.
- Rogers, R. and Yau, M. (1989). *A Short Course in Cloud Physics*. Butterworth-Heinemann.
- Rossow, W. and Schiffer, R. (1991). Isccp cloud data products. *B. Am. Meteorol. Soc.*, 72:2–20.
- Rossow, W. B. and Schiffer, R. A. (1999). Advances in understanding clouds from isccp. *B. Am. Meteorol. Soc.*, 80:2261–2288.

- Sandu, I., Stevens, B., and Pincus, R. (2010). On the transitions in marine boundary layer cloudiness. *Atmos. Chem. Phys.*, 10(5):2377–2391.
- Schreier, M., Mannstein, H., Eyring, V., and Bovensmann, H. (2007). Global ship track distribution and radiative forcing from 1 year of AATSR data. *Geophys. Res. Lett.*, 34(17).
- Seifert, A., Köhler, C., and Beheng, K. D. (2011). Aerosol-cloud-precipitation effects over germany as simulated by a convective-scale numerical weather prediction model. *Atmos. Chem. Phys. Disc.*, 11(7):20203–20243.
- Simmons, A., Uppala, S., Dee, D., and Kobayashi, S. (2007). ERA-Interim: New ECMWF reanalysis products from 1989 onwards. *ECMWF Newsletter*, 110:25–35.
- Small, J., Chuang, P., Feingold, G., and Jiang, H. (2009). Can aerosol decrease cloud lifetime? *Geophys. Res. Lett.*, 36(16):L16806.
- Spracklen, D. V., Carslaw, K. S., Pöschl, U., Rap, A., and Forster, P. M. (2011). Global cloud condensation nuclei influenced by carbonaceous combustion aerosol. *Atmos. Chem. Phys.*, 11(17):9067–9087.
- Stevens, B. and Feingold, G. (2009). Untangling aerosol effects on clouds and precipitation in a buffered system. *Nature*, 461:607–613.
- Stier, P., Feichter, J., Kinne, S., Kloster, S., Vignati, E., Wilson, J., Ganzeveld, L., Tegen, I., Werner, M., Balkanski, Y., et al. (2005). The aerosol-climate model ECHAM5-HAM. *Atmos. Chem. Phys.*, 5(4):1125–1156.
- Stier, P., Feichter, J., Kloster, S., Vignati, E., and Wilson, J. (2006a). Emission-induced nonlinearities in the global aerosol system: Results from the ECHAM5-HAM aerosol-climate model. *J. Climate*, 19(16):3845–3862.
- Stier, P., Seinfeld, J. H., Kinne, S., Feichter, J., and Boucher, O. (2006b). Impact of nonabsorbing anthropogenic aerosols on clear-sky atmospheric absorption. *J. Geophys. Res.*, 111(D18):D18201.
- Storelvmo, T., Kristjánsson, J., and Lohmann, U. (2008a). Aerosol influence on mixed-phase clouds in cam-oslo. *J. Atmos. Sci.*, 65(10):3214–3230.
- Storelvmo, T., Kristjánsson, J. E., Lohmann, U., Iversen, T., Kirkevåg, A., and Seland, Ø. (2008b). Modeling of the wenger–bergeron–findeisen process – implications for aerosol indirect effects. *Environ. Res. Lett.*, 3(4):045001.

- Sundqvist, H., Berge, E., and Kristjansson, J. (1989). Condensation and cloud parameterization studies with a mesoscale numerical weather prediction model. *Mon. Wea. Rev.*, 117(8):1641–1657.
- Taylor, K., Williamson, D., and Zwiers, F. (2000). The sea surface temperature and sea-ice concentration boundary conditions for amip ii simulations. *PCMDI Rep*, 60:28.
- Tegen, I., Harrison, S., Kohfeld, K., Prentice, I., Coe, M., and Heimann, M. (2002). Impact of vegetation and preferential source areas on global dust aerosol: Results from a model study. *J. Geophys. Res*, 107(D21):4576.
- Tiedtke, M. (1989). A comprehensive mass flux scheme for cumulus parameterization in large-scale models. *Mon. Wea. Rev.*, 117(8):1779–1800.
- Trenberth, K. E., Jones, P. D., Ambenje, P., Bojariu, R., Easterling, D., Klein Tank, A., Parker, D., Rahimzadeh, F., Renwick, J. A., Rusticucci, M., B, S., and Zhai, P. (2007). Observations: Surface and Atmospheric Climate Change. In Solomon, S., Qin, D., Manning, M., Chen, Z., Marquis, M., Averyt, K. B., Tignor, M., and Miller, H. L., editors, *Climate Change 2007: The Physical Science Basis. Contribution of Working Group I to the Fourth Assessment Report of the Intergovernmental Panel on Climate Change*. Cambridge University Press, Cambridge, United Kingdom and New York, NY, USA.
- Twomey, S. (1974). Pollution and the planetary albedo. *Atmos. Environ.*, 8:1251 – 1256.
- UNFCCC (1992). *United Nations Framework Convention on Climate Change*. United Nations Publications: Geneva, Switzerland.
- Vignati, E., Wilson, J., and Stier, P. (2004). M7: An efficient size-resolved aerosol microphysics module for large-scale aerosol transport models. *J. Geophys. Res*, 109:D22202.
- Wang, C., Corbett, J., and Firestone, J. (2007). Improving spatial representation of global ship emissions inventories. *Environ. Sci. Technol*, 42(1):193–199.
- Wang, H. and Feingold, G. (2009). Modeling Mesoscale Cellular Structures and Drizzle in Marine Stratocumulus. Part II: The Microphysics and Dynamics of the Boundary Region between Open and Closed Cells. *J. Atmos. Sci.*, 66:3257–3275.
- Wentz, F. and Meissner, T. (2000). *AMSR Ocean Algorithm. Algorithm Theoretical Basis Document, Version 2*. Remote Sensing Systems, Santa Rosa, California USA.

- Wielicki, B. A., Barkstrom, B. R., Harrison, E. F., Lee, R. B., Smith, G. L., and Cooper, J. E. (1996). Clouds and the earth's radiant energy system (CERES): An earth observing system experiment. *B. Am. Meteorol. Soc.*, 77(5):853 – 868.
- Wilcox, E. M. (2010). Stratocumulus cloud thickening beneath layers of absorbing smoke aerosol. *Atmos. Chem. Phys.*, 10(23):11769–11777.
- Wood, R. and Bretherton, C. (2004). Boundary layer depth, entrainment, and decoupling in the cloud-capped subtropical and tropical marine boundary layer. *J. Climate*, 17(18):3576–3588.

ACKNOWLEDGEMENTS

This PhD thesis couldn't have come out the way it did if it weren't for quite a number of individuals, so here I'd like to use some space to thank those that come into my mind now as all is coming to an end. If someone reads this and thinks he/she should also be in here, please bear with me at this point and poke me the next time we see...

First of all, I would like to thank Johannes Quaas for being a super adviser during in the course of my thesis. Thank you for giving me all the freedom one can imagine a PhD student could have and for providing the vast opportunities to meet and greet so many other peers of the scientific community. It is also his wonderfully pragmatic attitude that makes working with him so enjoyable.

I sincerely thank Hartmut Graßl for having had the initial confidence for letting me tackle a subject that had been the focus of so many studies before and it often were his little hints that guided me into a direction where no one else had gone before. Also, I thank him for having the grand overview of the work and for knowing beforehand what was possible/feasible and what not.

Andreas Chlond chaired my advisory panel and I found it especially encouraging that he showed his interest in my work not only in the panel meetings, but also on informal occasions, be it in the queue for coffee, on the stairs or when getting lunch at the EGU conference in Vienna.

I thank the whole atmosphere department and especially the members of the ex-CCF group (you know who you are !) for providing the ever stimulating and collegial research environment. Throughout my time at the MPI, quite a large number of people experienced me as their office mate and I thank Gabriel Chiodo, Tim de Paus, Rabab Mashayekhi, Nadine Schneider, Benjamin Grandey, Malte Rieck, Ann-Kristin Naumann, Ritthik Bhattacharya and Daniel Büttner for keeping our office so interesting.

The IMPRS-ESM provided the ideal framework for my PhD research. In particular, it is the the experience of being part of such a large group of people from all kinds of subjects that makes being part of the IMPRS so valuable. But the IMPRS would not be the way it is without Antje Weitz and Cornelia Kampmann whom I am very thankful to for keeping the system running.

Furthermore, the IMPRS-ESM provided me with the opportunity to spend two months at the University of Oxford. Without this exchange, substantial parts of this thesis couldn't have been performed in the given time frame. I am very thankful to Philip Stier for hosting me as an active member of his working group and for asking just the right questions at the right time. I very much enjoyed the working environment at AOPP and in particular, I thank Till Wagner for being a great office mate and hosting great board game nights, Benjamin Grandey for his never-ending cheerfulness and the terrific lunches at St. John's college, the rest of the Climate Processes working group (Rosalind West, Zak Kipling, Natalie Weigum and Edward Gryspeerdt) for keeping me involved, Tim Samwell of COSC for pushing hard on me in the pool and all the folks at NOOC for making my stay in the UK so amazing.

Thank you Jessica Bickel, Benjamin Grandey, Lee Miller, Ulrike Niemeier, Andy Sayer and Nadine Schneider for doing a wonderful job proof-reading previous versions of this thesis.

Funding of this PhD project was provided by the EU FP6 (Integrated Project QUANTIFY) and the EU FP7 (MACC). Gunnar Myhre and Michael Gauss provided the inventory of shipping emissions and thank you to Yves Balkanski for keeping in touch. Irina Sandu gave advice for using HYSPLIT.

I am deeply thankful for the enduring support and motivation that Steffi has given me throughout the last years. Thank you for understanding, keeping me distracted and showing me the importance of looking beyond known horizons.

Thank you to all my friends for keeping me busy and involved in those activities that just give that little "extra".

Last but not least I thank my family for all their love, support and understanding throughout my life. Without you all, I wouldn't be where I am today. Thank you.

